PHOTOELECTROCHEMISTRY OF MICROSTRUCTURED SILICON MATERIALS FOR SOLAR ENERGY APPLICATIONS

Thesis by

James R. Maiolo III

In Partial Fulfillment of the Requirements

for the Degree of

Doctor of Philosophy

California Institute of Technology

Pasadena, California

2009

(Defended May 12, 2009)

Acknowledgements

I have a great number of people to thank for a great many contributions that they have made to my life and journey. Anyone who knows me fairly well probably understands that much of who I am is made up of the people I have met and worked with and admired, and that I would certainly not have had such an interesting and full life up to this point without them. I want to start by thanking my wife, Lea. We met right about when I started grad school, and she has stuck with me through everything and has put up with a lot so that I could earn this degree. She made all the tough times easier and all the good times better. Plus, she puts up with me muttering to myself and pacing while I am thinking really hard.

My progression as a scientist has been formed and molded by my scientific mentors along the way. It has been an honor working for Nate Lewis these last few years. I honestly do not think I have met anyone so passionate about science and so brilliant. He is an intellectual rock star. I also want to thank my committee for their support. I had the interesting pleasure of having two committees—first Pat Collier and Jonas Peters with Nate, and now Harry Gray, Harry Atwater, and Mitchio Okumura with Nate. Everyone on my committees has been helpful and supportive during this process, but I want to particularly single out Harry Gray, who is just an all around great guy.

Before I came to grad school, I had the pleasure of working with Marc Ferrer and Liz Ottinger both at Swarthmore and at Merck. Their direction of my undergraduate thesis work helped me to learn about research and provided me with some great opportunities. Before working with them, I was privileged to work at the Hershey

Medical Center over a couple of summers with both Ira Ropson and Kay LaNoue, who helped me to learn about research right in my home town.

One of the best parts of being a grad student is being able to indulge your academic curiosity, and it is that curiosity that has always brought me to new and interesting subject matter. For this, I largely blame a string of excellent teachers. Probably one of the first, although not in science, was a middle school English teacher, Mrs. Templeton, who encouraged me to read and to write and to think. Also in middle school, Mrs. Fackler was a great science teacher and Science Olympiad coach. Dr. Mondschein, and her support in both AP Chemistry and an independent study, is probably the reason that I decided to go into science and to choose chemistry in particular. Finally, in college, I had some great professors who really stoked my passion for learning, particularly Tom Stephenson, who made me want to be him when I was all grown up, and Jim Rego, who made chemistry fun and real.

Throughout my career, I have had great interactions with my peers, and Caltech has been a fabulous place to study because I have always been surrounded by brilliant and interesting people. When I first started, the Lewis Group was very accepting, and I had some great mentoring from Dave Michalak and Lauren Webb at the beginning. Also, from the very start David Knapp (DK) has been probably the most helpful group member. He knows how to run everything, and he has given extremely generously of his time in helping the rest of the group. DK also did most of the hard work in the scanning confocal microscopy experiments. Pat Hurley and his expertise were also invaluable during the beginning stages of my work.

I inherited the position of safety officer from Matt Traub, who was very helpful in showing me the ropes. Several years later, I was pleased to hand off the position to Liz Santori, who is probably keeping the group safer than I did. I am also very much indebted to a number of people who helped me to get samples for my electrochemical work. Josh Spurgeon was always my go-to guy for wire arrays, and he put up with my requests quite good naturedly. Brendan Kayes and Mike Filler in the Atwater group were bringing me wire samples from the beginning, and worked hard with me to get the first wire array paper out. M. David Henry worked with me for about a year, making me pillar samples, and I thank him for his patience as well. Finally, Emily Warren helped me with doping wire array samples.

I have had the privilege to work with two great SURFs over the years—Natalie Szweda and Leon Liu—and I hope that both of them go far in life. In recent days, I have enjoyed working with Liz Santori and showing her the ropes of electrochemistry. I have had so many great interactions with people in the group that the best I can do here is to list them—Steve Maldonado, Jordan Katz, Kate Plass, David “Cinco” Gleason-Rohrer, Heather McCaig, Edgardo Garcia, Craig Wiggenhorn, Marc Woodka, Anna Folinsky, Tony Fitch, Don Walker, Greg Kimball, Leslie O’Leary, Erik Johansson, Shannon Boetcher, Joe Beardsly, Mike Walter, Kimberly Marshall, Tom Hamann, and Mike Kelzenberg. Thank you to everyone for making this a really great and fun experience. Also, special thanks to Jillian for working so hard with me on the GRS. Finally, I have tons of appreciation for all the hard work that Sherry Feick, Amy Crown, and April Neidholdt do to keep all the groups running.

Abstract

In the face of mounting evidence that CO_2 emissions from the burning of fossil fuels is a key contributor to anthropogenic global climate change, the search for a carbon-neutral energy source that is scalable and economically viable has become a key research target. Orthogonalization of the directions of light absorption and charge carrier collection in solar cell absorber materials, as in arrays of wires with radial junctions, has the potential to enable the use of low-purity and low-cost materials in efficient solar cells. This work focuses on the use of structured silicon materials as the absorber in semiconductor/liquid junction photoelectrochemical cells in order to verify the potential of structured materials to enable efficient and inexpensive solar cells.

Macroporous Si was used as a physical model system for wire-array solar cells. Using high-purity starting materials, it was found that increasing the surface area by porous etching did not dramatically lower the observed energy conversion efficiency, and efficiencies in excess of 10% were observed even for the longest pores studied. The open-circuit voltage (V_{oc}) was lowered in samples with long pores, however, verifying the principle that a reduction in V_{oc} is expected with increased junction area due to a decreased flux of minority carriers through the junction. This will be an important design principle for building structured solar cells. In addition, diffusion of Au impurities into macroporous Si was used to explore the effect of employing a structured junction in poor quality materials.

Wire array solar cells produced by chemical vapor deposition were also measured in liquid junction cells. Initial studies showed significant photocurrent and photovoltage over the control substrate. Improved arrays having longer wires showed significantly higher photocurrents, giving energy conversion efficiencies as high as 1.5% in the liquid junction cell, and it has been shown that the photoelectrochemical properties of the wire array samples are due to the CVD-grown wires rather than the silicon substrate used. These results are an important first step toward understanding and building efficient, low-cost solar cells using structured materials.

Online Availability

Chapters 2 and 4 of this work have been previously published in American Chemical Society (ACS) Journals. Per ACS policy, those chapters cannot be made available online to the general public. However, free copies of the original papers are available by using the internet addresses shown below. Please note that a one-time, free registration is required to download the papers.

Chapter 2 - http://pubs.acs.org/cgi-bin/download.pl?jp711340b/o498

Chapter 4 - http://pubs.acs.org/cgi-bin/download.pl?ja074897c/Q7Lo

Table of Contents

List of Figures

List of Tables

Chapter 1

Motivation and Introduction

1.1 Summary

Considering the growing evidence that CO_2 emissions from fossil fuels are a major contributor to anthropogenic global climate change, a source of carbon-neutral energy will be needed at the scale of our current global energy consumption. We propose to use solar energy due to its abundance and wide availability, but there are significant challenges to producing cost-competitive solar energy solutions. One strategy to reduce the cost of current solar cells is to decouple the directions of light absorption and charge carrier collection by using materials with highly structured junctions. This principle has been shown to improve the efficiency of low-quality—and therefore inexpensive—materials in simulations, but there are significant challenges and drawbacks associated with using highly structured materials. Some of these include the expected increase in surface and junction recombination, as well as the expected decrease in open circuit voltage due to reduced carrier flux per unit of junction area. The use of semiconductor/liquid junctions provides a robust method of forming highly structured junctions and thus allow the expected challenges to be probed in a controlled fashion. These principles form the foundation of the work carried out in this thesis.

1.2 Global Climate Change

The primary motivational force behind this work thesis is the apparent onset of anthropogenic global climate change. Evidence is mounting that human actions have created circumstances in which the energy flux of the Earth is slightly out of balance, causing a rise in the global average temperature, and climate models predict that this temperature change may bring with it a host of sweeping changes in the weather patterns and coastlines of the world. The increased levels of CO_2 and other greenhouse gases in the atmosphere are key contributors to global climate change, and the chief source of CO_2 emissions is the burning of fossil fuels for energy. As a result, finding carbon-neutral alternatives to fossil fuels is an important and active area of research across the sciences, and the focus of this thesis work has been on the understanding and development of silicon devices for solar energy generation.

1.2.1 Radiative Forcing and Warming

When examining the factors contributing to global climate change, it is useful to consider the radiative forcing (RF) associated with each. Radiative forcing is related to the change in energy flux into and out of the Earth's atmosphere, calculated after accounting for thermal equilibration of the stratosphere (upper atmosphere).[1] The RF is measured relative to the preindustrial era (1750), so it primarily represents the changes due to industrialization.[1] Radiative forcing is expected to be generally related to warming and cooling (positive forcing for warming and negative forcing for cooling), but there are many factors affecting the global climate, and sophisticated climate models are needed to predict the precise impact of a given RF on the Earth's temperature.[1] Nevertheless,

radiative forcing is a useful concept because it captures the essence of the climate change problem—that there is an imbalance between the flux of energy into the Earth's atmosphere and out of it. Radiative forcing is also a measurable quantity and therefore independent of global climate models, so that it can be used to assess the likely relative impact of certain conditions without resorting to modeling. As a result, RF is usually discussed in the context of comparing the relative impact of different contributors to global climate change.

The key motivation for moving away from fossil fuels and other sources of CO_2 is the expected impact of increased CO_2 concentrations on global climate change. Figure 1.1 shows the radiative forcing values associated with different human and natural activities.[1] Note that the expected RF due to CO_2 emissions is positive (indicating warming) and larger than all of the other long-lived greenhouse gases combined. Furthermore, note that expected total RF for all human activities is roughly equal to that of CO_2 alone. These observations imply that mitigation of CO_2 emissions would be likely to have a stronger impact on global climate change than any other effort. Figure 1.1 also shows that CH_4, N_2O, and halocarbons make a significant positive contribution to RF, and most of these are not a direct result of burning fossil fuels. Thus, complete mitigation of positive RF induced by humans will necessitate addressing the sources of other long-lived greenhouse gases. Also, there are significant human-induced negative contributions to RF, largely due to aerosols—particulate matter that has been released into the atmosphere.[1] The impact of aerosols on RF begins to illustrate the complexity of anthropogenic global climate change, as both aerosols and CO_2 result from industrial

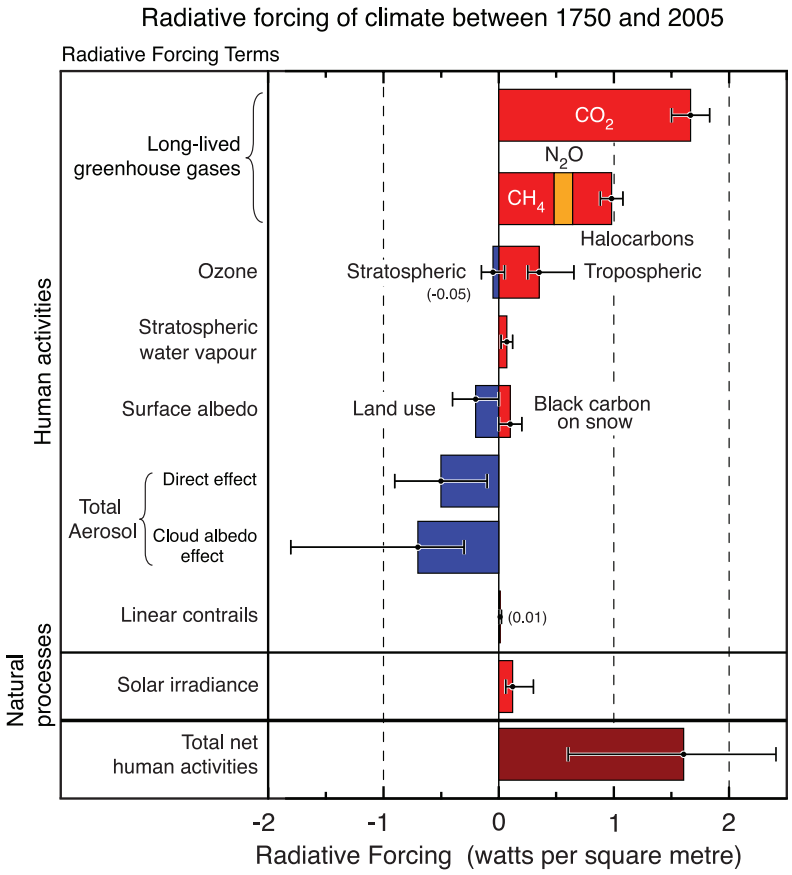

Figure 1.1. *Radiative forcing between 1750 and 2005 (from the IPCC Fourth Assessment Report).[1] Positive forcings are likely to lead to warming while negative forcings are likely to lead to cooling. Note that some contributors (e.g., Surface Albedo) can contribute both positive and negative forcings.*

processes and the burning of fossil fuels, but the effects are in opposing directions. Finally, note that the contribution of natural processes to the RF over this same period of time is expected to be much smaller than those made by human actions.[1] This is compelling evidence for the influence of humans on the observed and predicted global climate change.

Although the impact of radiative forcing on the global average temperature requires climate modeling, changes over the last few years already show a warming trend. Figure 1.2 shows the recent trend in the annual mean global temperature.[2] We can see from this

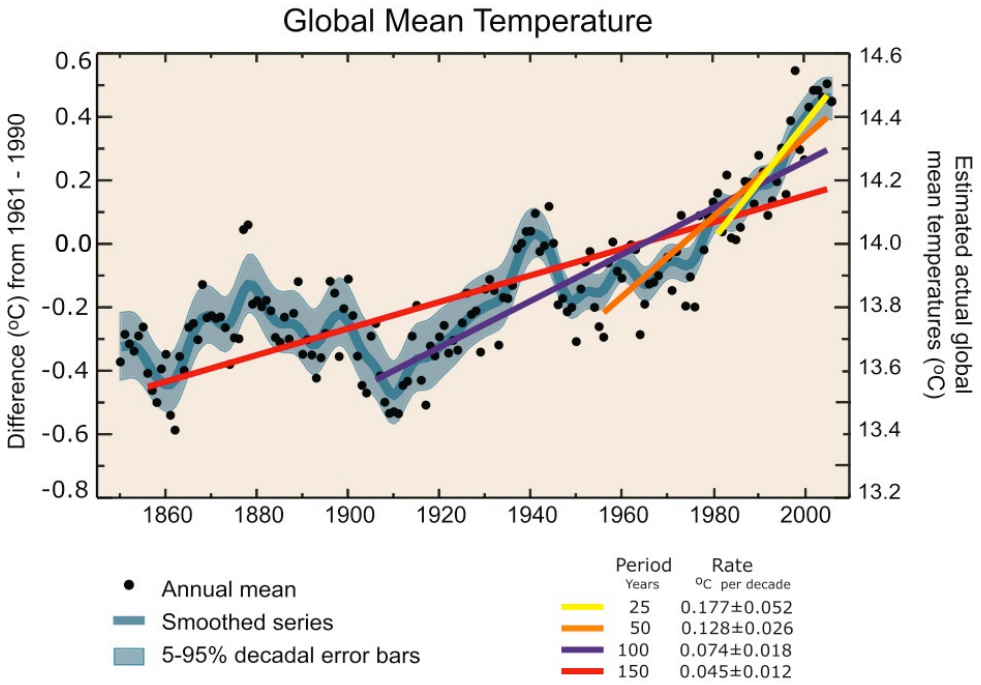

Figure 1.2. *Global average temperature from 1850 to the present (from the IPCC Fourth Assessment Report).[2] Notice that the slope of the temperature increase is rising in recent years, in agreement with the increase in radiative forcing.*

plot that there is a general trend of warming on a global average, although the variation from year to year is quite large. Also plotted are lines showing the averaged behavior over several time periods, and it is immediately apparent that the slopes of these lines are increasing in recent years as compared to the past 150 years.[2] This data does not prove that anthropogenic contributions to radiative forcing are causing an increase in the global temperature, but it does provide an impetus to start reducing the sources of radiative forcing rather than risking the continued increase in global temperature and the subsequent dramatic changes in the global climate. An extremely thorough analysis of the likelihood that global climate change is being caused by human actions, and the probably outcomes of such climate change is available in the Intergovernmental Panel on Climate Change Fourth Assessment Report.[3]

1.2.2 Solar Energy

There are a number of possible choices to replace fossil fuels, but light from the sun is one of the most abundant sources of carbon-neutral energy available.[4] Indeed, the fossil fuels currently used are essentially concentrated energy from the sun stored as chemical bonds. To understand the scale of the available solar energy resource, consider that the solar constant, the energy of incoming sunlight per unit area, is 1.37 kW m^{-2}.[5] The cross-sectional area of the Earth is about 1.27×10^{14} m^2 on average, giving a total incident power from the sun of about 174,000 TW.[5] This is the flux outside the atmosphere of the Earth, so it must be corrected for the total amount of energy that is reflected, which is known as the Earth's albedo and is about 30% on average.[6] This gives a total absorbed power from the sun of about 122,000 TW. This is a vast resource compared to the total global power consumption of only 15 TW currently. Taking this analysis one step further, we can calculate the total land area necessary to generate all of the world's power from the sun. Assuming 10% efficient energy conversion, and given that land mass accounts for only 29.2% of the total surface of the Earth,[5] we find that 0.4% of the Earth's land area would be needed to be covered in solar energy conversion devices in order to power the planet. In contrast, using all of the arable land to grow crops for biomass would only yield a power equivalent of ~8 TW, about half of what is currently being consumed, and there would also be fierce competition between land use for energy crops and for food crops.[4] Thus, solar energy is clearly an attractive avenue for providing significant carbon-neutral energy.

1.3 High Aspect Ratio Structures for Solar Energy

In order to take advantage of the vast solar energy resource in a meaningful way, it will be necessary to develop and manufacture solar energy conversion devices that are cost competitive with fossil fuels and nuclear fission. Although the price of conventional crystalline and multicrystalline silicon solar cells continues to drop due to advances in manufacturing and due to economies of scale,[4] a significant breakthrough in solar energy capture and conversion could lead to a step change in the cost of solar electricity. Furthermore, many groups are vigorously working toward the ultimate goal of a photoelectrochemical fuel-producing device that could be manufactured cheaply at scale. Photon capture and conversion will be an essential component of either photovoltaic or photoelectrochemical energy conversion devices. For these reasons, this work focuses primarily on the photoelectrochemical properties of high-aspect-ratio silicon structures with the goal of understanding the utility of these types of structures for low-cost solar energy capture and conversion.

1.3.1 Decoupling Carrier Collection and Light Absorption

One strategy for mitigating the cost associated with traditional photovoltaics is to enable the use of cheaper materials in the light absorber. In traditional silicon solar cells, the cost of the pure single crystalline silicon typically contributes around 50% of the total module cost,[7] so the impact of using low-cost materials would be significant. However, low-cost semiconductor materials typically suffer from low minority carrier diffusion lengths, leading to inefficient devices due to decreased carrier collection.[8] Since the typical figure of merit used to assess the economic viability of solar modules is the cost

per peak installed watt ($/$W_p$), there is no benefit in sacrificing efficiency (which reduces W_p) in order to reduce the module cost. Thus, strategies must be pursued that maintain high efficiency in inexpensive materials.

One strategy that has been proposed to increase the efficiency of cells constructed from low-cost and low-quality materials is the orthogonalization of light absorption and charge carrier collection (Figure 1.3). In the traditional planar cell, the direction of light

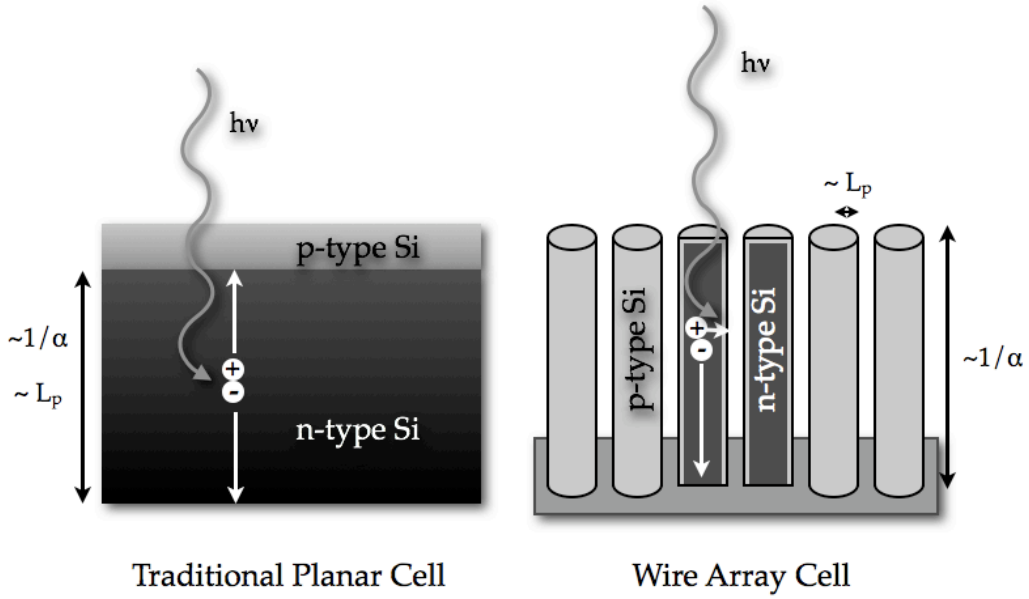

Figure 1.3. *Schematic diagram of a traditional planar solar cell and the proposed wire array geometry. In the planar cell, the absorption length (~1/α) must be comparable to the minority carrier diffusion length (L_p). However, in the wire array cell, the directions of light absorption and minority carrier collection are decoupled, allowing L_p to be independent of 1/α.*

absorption is the same as that of charge carrier collection. Thus, to build an efficient cell, the absorber must be thick enough to absorb all the light (about 100 μm for Si),[9,10] but then the minority carrier diffusion length must be long enough that all of the generated charges are collected. This constraint couples the material absorption to the material purity, typically requiring high purity for indirect semiconductors such as Si.[9] In the

radial junction wire geometry depicted in Figure 1.3, however, the light is still absorbed along the long axis of the wires, while the minority charge carriers can be collected radially. In this case, we expect from an intuitive analysis to be able to build structures from low diffusion length materials while maintaining high efficiencies.

In order to more fully understand the potential benefits and drawbacks of building wire array solar cells, Brendan Kayes carried out detailed 1D diffusion/drift calculations on both planar and radial junction structures.[11] These calculations assumed an abrupt p-n junction, with a p-type base and heavily doped n-type emitter. Furthermore, carrier diffusion along the axis of the wire was not considered in the radial junction case, so that solely radial diffusion was assumed. Under these assumptions, the efficiency surfaces shown in Figure 1.4 were observed.[11] In these simulations, the wire radius was taken to be equal to the minority carrier diffusion length, as this was found to be approximately optimal.[11] The simulations show that, in the absence of traps in the depletion region,

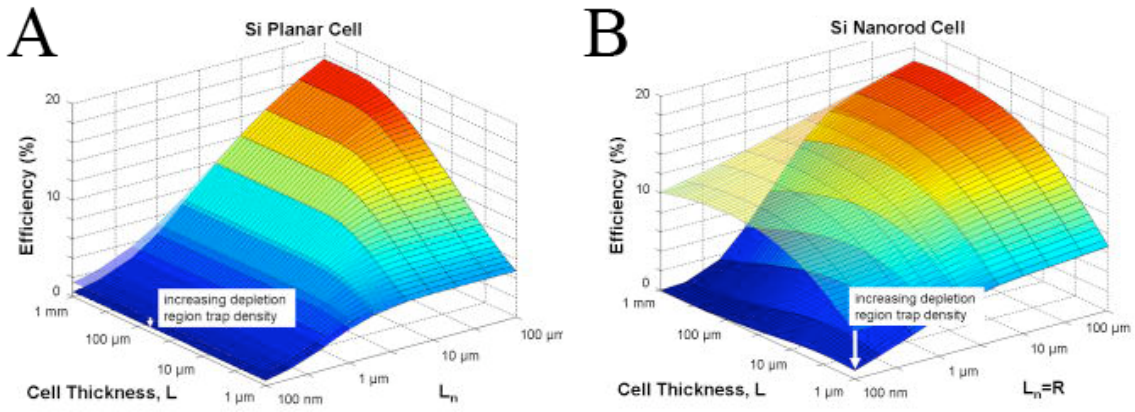

Figure 1.4. *Device physics modeling of the efficiency of planar and wire solar cells.[11] Cell thickness is in the direction of the incident light. A) Traditional planar cell. Note that depletion region recombination has little effect on the observed efficiency. B) Si wire cell. The top curve assumes a low trap density in the depletion region, while the bottom curve assumes uniform trap density throughout the wire. The wire radius is set equal to the minority carrier diffusion length.*

efficiencies in excess of 10% are theoretically possible even for materials with diffusion lengths as low as 100 nm (Figure 1.4B, top curve). However, when the trap density in the depletion region is taken to be equal to that in the quasi-neutral region, the efficiency of the devices is found to drop off sharply at low diffusion lengths (Figure 1.4B, bottom curve). This is to be expected considering the vastly increased depletion area in the very small wires that would need to be employed in materials with low minority carrier diffusion lengths. Nevertheless, there is an area in the 1–10 μm diffusion length regime where an improvement in efficiency is expected with wire array samples over planar samples in the presence of significant depletion region impurities.

Another key consideration arising from simulation of radial junction Si solar cells is the effect of increased junction area on the open circuit voltage (V_{oc}) in the light (Figure 1.5). From Figure 1.5B, it is clear that, even in the absence of significant depletion region recombination, the V_{oc} for a wire array cell is expected to decrease with both

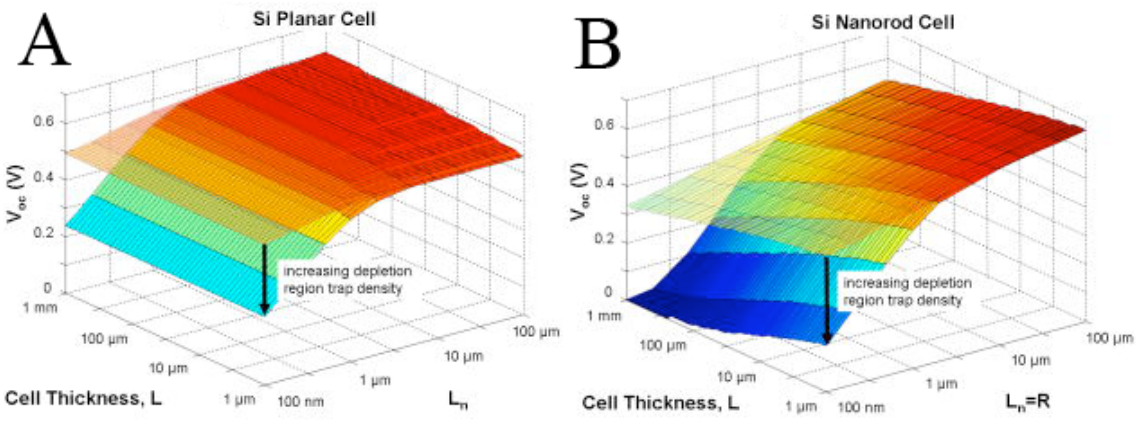

Figure 1.5. *Device physics modeling of the V_{oc} of planar and wire solar cells.[11] Cell thickness is in the direction of the incident light. The top curves assume a low trap density in the depletion region, while the bottom curves assume uniform trap density throughout the wire. A) Traditional planar cell. B) Si wire cell. The wire radius is set equal to the minority carrier diffusion length. Note that the V_{oc} decreases with cell thickness and L_n even in the absence of depletion region recombination.*

decreasing minority carrier diffusion length and decreasing cell thickness.[11] Thus, an increase in the total expected junction area will give rise to a decrease in the observed V_{oc}. This is also expected from a basic analysis of the dependence of V_{oc} on dark and light currents as given for the case in which recombination in the bulk (or quasi-neutral region) is the primary mechanism for recombination:[12]

$$V_{oc} = \frac{AkT}{q} \ln\left(\frac{J_{ph}}{J_0}\right) = \frac{AkT}{q} \ln\left(\frac{I_{ph}}{\gamma I_0}\right), \tag{1.1}$$

where k is Boltzmann's constant, T is the temperature, q is the charge on an electron, A is the diode quality factor, I_{ph} and J_{ph} are the photocurrent and photocurrent density, I_0 and J_0 are the dark current and dark current density, and γ is the surface area enhancement, the ratio of the total junction area to the projected area of the device. Thus, we can see that an increased junction area is expected to predictably lower the value of V_{oc} in the case where the carriers are collected uniformly over the entire junction. This is due to the reduced splitting in the quasi-fermi levels observed when the charge carriers are diluted over a larger junction area.[13-16] In the detailed simulation of Kayes et al. the increase in junction area was convoluted with a decrease in the minority carrier diffusion length,[11] but the analysis based on bulk recombination assumes no such reduction in the diffusion length. Both analyses point to a reduction of about 60 mV in the V_{oc} for every 10-fold increase in junction area relative to projected area. The change in V_{oc} with junction area will be explored primarily in chapters 2 and 3 of this work.

1.3.2 Macroporous Silicon for Physical Model Systems

In the interest of obtaining a more complete understanding of the important factors involved in the design of a highly structured solar cell, physical model systems were initially sought. Macroporous silicon is an excellent candidate for such a model system because it can be readily fabricated from materials of known crystallinity and purity, eliminating the need to simultaneously probe effects originating from the bulk material properties and the structured nature of the junction. Macroporous silicon can be readily fabricated by etching n-type Si in HF containing solutions under illumination from the back of the sample.[17-23] The pore etching typically proceeds in the <100> direction and pore formation is believed to take place primarily under hole-limited conditions, where holes generated at the back of n-type silicon diffuse toward the front and are collected at the pore tips.[17-23]

Samples of n-type porous silicon can then be used as a model system for wire array cells because there is significant potential for the radial diffusion of minority charge carriers and their subsequent collection at a junction formed at the pore sidewalls. By forming semiconductor/liquid junctions with macroporous silicon devices, conformal contact can be made to the pore sidewalls and carriers can be harvested at the sidewalls. Chapters 2 and 3 of this work describe photoelectrochemical experiments conducted on n-type macroporous silicon.

1.3.3 Chemical Vapor Deposition Growth of Wires

Growth of silicon wire arrays by chemical vapor deposition (CVD) is a promising route to the inexpensive, scalable synthesis of structured silicon devices starting from

widely available starting materials. CVD by the vapor-liquid-solid (VLS) method was pioneered by Wagner and Ellis in the 1960s for the growth of Si wires.[24,25] In the VLS method (Figure 1.6), silicon precursors (typically SiH_4 or $SiCl_4$) are introduced in the gas phase in the presence of Au particles. At elevated temperatures, the precursors decompose and Si deposits in the Au particle, eventually forming a liquid eutectic mixture. As the particles become supersaturated with Si, rods begin to grow by precipitation of Si with the Au catalyst particle staying on the tips of the rods. CVD growth of wires by VLS is a promising route for the production of low-cost materials because it can be carried out at large scales, and it can be used to produce structured materials directly.[26-31]

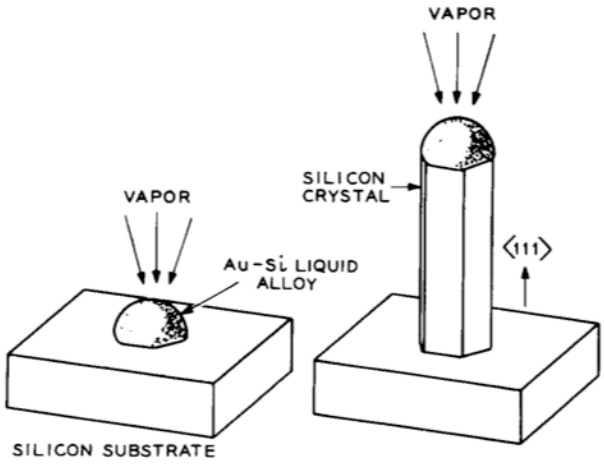

Figure 1.6 *- Schematic of Si wire growth by the CVD-VLS method.[25] Beginning with Au catalyst particles, Si vapor dissolves in the catalyst and then precipitates to form wires that grow preferentially in the <111> direction.*

In particular, work in the Atwater and Lewis groups has demonstrated controlled growth of uniform arrays of Si wires starting from either Au or Cu catalyst particles with $SiCl_4$ as the feed gas.[29] The key to obtaining uniform arrays of Si wires was the use of an oxide barrier layer to prevent flow and pooling of the catalyst at the high temperatures used for growth.[29] It was also found that the as-grown wire arrays could be readily removed from the substrate in a thin film of polymer (e.g. polydimethylsiloxane—PDMS), leaving the ends of the wires exposed for further chemistry and measurement.[32]

Finally, it was demonstrated that although a single crystalline substrate is used for templated growth, that substrate can be used repeatedly by removal of the wires from the surface, selective etching of the wire "stumps," and electrodeposition of additional Au catalyst back into the oxide mask.[30] The demonstration of these remarkable fabrication techniques opens the door to many uses of CVD-grown Si wire arrays in devices for solar energy capture and conversion. Chapters 4 and 5 of this work will focus on the photoelectrochemical results obtained from studying these wire arrays.

1.3.4 Solid State Structured Devices

Before the use of wires for solar energy conversion was explored in the literature, other techniques were explored that made use of reduced carrier collection distances. These include the vertical multijunction solar cell[33] and the parallel multijunction solar cell,[34,35] both of which incorporate significantly increased junction areas with commensurate smaller distances for minority carriers to travel before collection. Furthermore, both methods were shown to produce efficient cells using techniques that give rise to high purity silicon.[36,37] These results strengthen the principle that structured solar cells can be produced, but low-cost fabrication methods need to be pursued in order to realize the full utility of large junction areas.

Other methods have also been employed to produce high aspect ratio solar energy conversion devices that do not involve traditional diffused p-n junctions but that nevertheless produce solar cells with no liquid component. Most of the other devices that have been constructed using structured materials have consisted of semiconductor rods or wires embedded in conducting polymer layers.[38-43] In these cases, the conductive

polymer typically acts as the absorber, with the semiconductor rods serve as both the emitter layer and as charge conduction pathways for the minority carriers after they have been collected.[38-41,43] The principle of increasing junction area in order to improve carrier collection in low diffusion length materials is still at work in these studies, however, as there is an enhanced junction area due to contact with the semiconductor wires. In fact, the most successful polymeric solar cells to date have been fabricated using blends of conductive polymer with fullerene derivatives.[44-47] These bulk heterojunction devices are expected to have very large junction areas, which are necessary due to the short exciton diffusion length in conductive polymers (~10 nm).[48]

There have also been an number of studies employing Si nanowires in recent years. In one study, n-type Si nanowires were grown by CVD-VLS on a multicrystalline p-type Si substrate, thus forming the p-n junction during the wire growth process.[49] In this case the junction is axial rather than radial, so the principle of enhanced junction area does not apply. In another study, p-type Si nanowires were grown by CVD-VLS directly on a thin film of Ta_2N on stainless steel, and the solid state junction was formed by conformal deposition of n-type amorphous Si.[50] Square centimeter sized cells were produced in this case, although both the J_{sc} and V_{oc} were found to be limited by shunting and geometrical considerations.[50] In another study, n-type Si wires were created by chemical etching of a Si wafer, and a thin film of p-type amorphous Si was deposited to form the junction.[51] In this case a significant improvement in J_{sc} was observed compared to previous studies.

1.4 Semiconductor Liquid Junctions

The material presented in this section is intended to set the stage for the photoelectrochemistry conducted in this work, but there are a number of excellent books and reviews available describing both semiconductor physics and semiconductor photoelectrochemistry in detail.[9,12,52,53] As an alternative to making metallurgical p-n junction contacts to the structured samples considered here, semiconductor/liquid junctions were formed. Liquid junctions were used primarily to ensure good conformal contact to all of the structures studied, and those employed here are also known to form high barrier height, low surface recombination velocity junctions with Si.

1.4.1 The n-Si/Methanol Junction

There is a significant body of work in the literature concerning non-aqueous semiconductor/liquid junctions, particularly the Si/methanol junction. For both n- and p-type silicon in contact with methanol containing a series of redox couples with solution potentials that vary over 1 V, it was found that the open circuit voltage (V_{oc}) behavior in the light was nearly ideal.[54,55] This indicates that the fermi-level pinning typically observed in Si/metal contacts is not observed under the appropriate conditions in Si/liquid contacts. This allows the redox couple in the liquid phase to be chosen in order to set the barrier height of the junction. For n-type Si, ferrocene$^{+/0}$ and dimethylferrocene$^{+/0}$ give high barrier height contacts.[54] Furthermore, the n-Si/methanol/ferrocene$^{+/0}$ system has been shown to have good interfacial properties for photoelectrochemistry. Studies of the surface recombination velocity (SRV) of various silicon interfaces showed that the SRV for n-Si while in contact with ferrocene$^{+/0}$/methanol is on the order of 20 cm s^{-1}, which is

comparable to or lower than the value found for Si in HF.[56] Furthermore, this low SRV was retained when the samples were removed into a N_2 atmosphere, which is not the case for samples treated in a ferrocene/THF solution.[56] This was taken to indicate surface functionalization of n-Si in methanol in the presence of a one-electron oxidant, most likely due to the formation of a monolayer of methoxy groups on the Si surface.[56,57]

Given the high barrier heights and low SRV values obtainable, the n-Si/methanol/ ferrocene$^{+/0}$ system is expected to produce excellent photoelectrochemical energy conversion devices. With this system, over 10% energy conversion efficiency was found for single crystalline samples,[58-60] and efficiencies as high as 7.2% were achieved for polycrystalline Si.[61] However, when a liquid is used as the contacting phase rather than a metal or a semiconductor, charge conduction in the liquid will necessarily be due to mass transport of the redox species used. These mass transport limitations will change the shape of the measured *J-E* curves in accordance with the behavior of Nernstian redox molecules—a sigmoidal distortion of the curve is expected near the anodic and cathodic mass-transport-limited currents, and there will be a commensurate shift in the curves, even far away from the limiting currents (Figure 1.7).[62] This gives rise to the concentration overpotential loss in the cell, which can also be considered as the energy used to set up the concentration gradient from the electrode to the bulk of the solution. Since the ferrocenium derivatives are deeply colored, they have typically been present in small amounts for photoelectrochemical measurements, giving rise to a reasonably large concentration overpotential loss. This loss can be measured by tracing out the Nernstian *J-E* curve at a Pt electrode and measuring the cathodic and anodic limiting currents.[62,63]

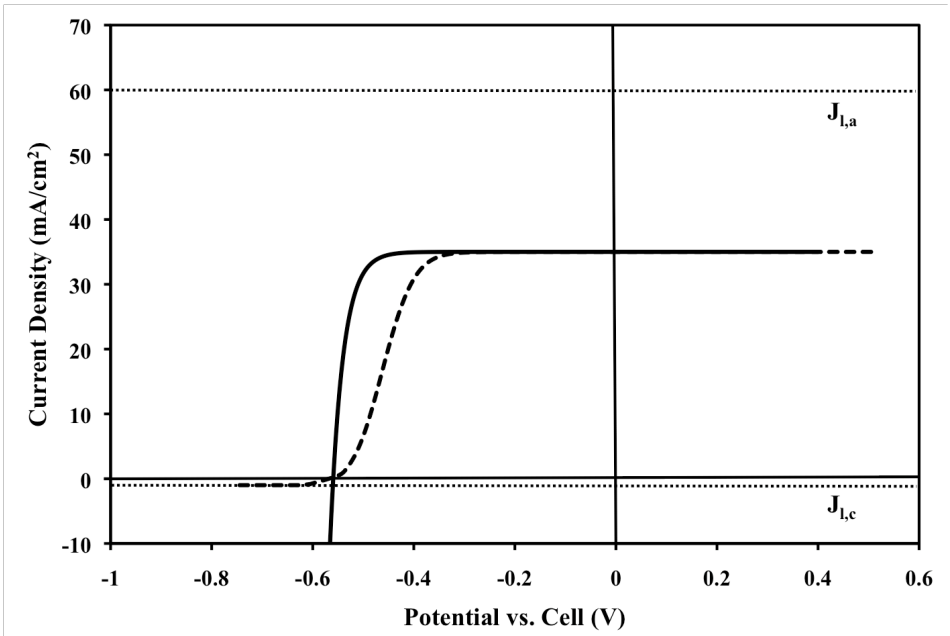

Figure 1.7. *Concentration overpotential effect. The dotted lines indicate the anodic and cathodic mass transport limited currents. The solid line shows a theoretical bulk recombination limited p-n junction photodiode at a typical current density. The dashed line shows the same diode after concentration overpotential has been applied according to the mass transport limited currents. Note that the curve is shifted to more positive potentials even far away from the small cathodic limiting current.*

When the concentration overpotential and series resistances losses are reduced—as they are in a thin layer, two-electrode photoelectrochemical cell—the *J-E* curves for n-type Si show the expected diodic character, and the efficiency values are increased to 14%.[58] Correction for the concentration overpotential and series resistance losses will be an important consideration when measuring structured samples, and this correction is discussed in Chapters 2, 4, and 5 of this work.

1.4.2 Structured Semiconductors in Photoelectrochemical Cells

There are numerous examples of the use of structured semiconductor materials in photoelectrochemical energy conversion devices. Perhaps the most prevalent of such devices is the dye-sensitized solar cell (DSSC) initially developed by Grätzel and O'Regan,[64] which has since been studied extensively, reaching efficiencies greater than

10%.[65-67] The DSSC consists of nanoparticles of TiO_2 or another large band-gap metal oxide sensitized with a dye that absorbs in the visible (Figure 1.8). Upon excitation, the dye can rapidly inject an electron into the TiO_2. The electron travels through the TiO_2 to the back contact, and through the external circuit to a counter electrode, where it can reduce I_3^- to I^-. Finally, the reduced form of the dye is regenerated by reaction with I^-. Thus, the cell is a regenerative photoelectrochemical cell using a structured material, where the structure serves the primary function of increasing the area for dye absorption. DSSCs have been developed in which the metal oxide component consists of oriented arrays of wires,[68-71] but these devices retain the essential elements of nanoparticle DSSCs in that the semiconductor is functioning primarily as a charge collector rather than as the

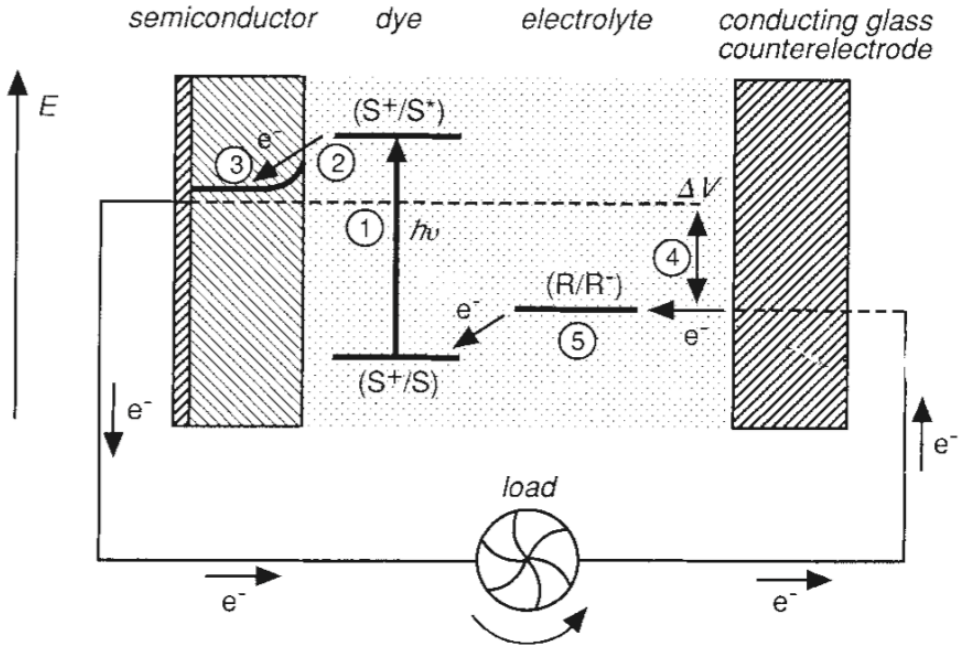

Figure 1.8. *Schematic of the dye-sensitized solar cell.[64] The semiconductor typically consists of nanoparticles of TiO_2. 1) Excitation of the dye by incident light. 2) Charge injection from the dye excited state. 3) Electron transport to the back contact. 4) The expected V_{oc} of the cell is given by the difference shown. 5) The dye is regenerated by a mediator.*

absorber. However, the use of metal oxide wires is also expected to give rise to improvements in the majority carrier charge transport properties of these devices.

There are also examples of using structured semiconductor materials as the main absorber in photoelectrochemical cells. In particular, work by Kelly and co-workers. showed that significant improvements in the charge carrier collection efficiency in GaP could be obtained by subjecting the substrate to porous etching.[72,73] This result directly demonstrates the principle that decoupling the directions of light absorption and charge carrier collection in low-quality semiconductors can lead to improved carrier collection. The use of macroporous Si in this work is analogous to the previous studies by Kelly and co-workers, except that Si can be made routinely with much longer minority carrier diffusion lengths. In addition, recent studies have shown photoelectrochemical measurements on silicon wire arrays produced by CVD-VLS growth[74] and by top-down etching to produce wires.[75]

1.5 Conclusions

The evidence for anthropogenic contributions to radiative forcing, and therefore to global climate change, is overwhelming. In particular, the emissions of CO_2 from the burning of fossil fuels forms a large portion of the radiative forcing, and therefore the elimination of fossil fuels is an excellent target for current research. Furthermore, of the currently available sources of carbon-neutral energy, solar energy is one of the most promising because the incident power from the sun is nearly five orders of magnitude greater than our current global energy consumption. Harvesting this energy requires the widespread deployment of solar energy conversion devices, but the current cost of solar

photovoltaics is too high relative to the cost of fossil fuels to drive this deployment. Therefore, reducing the cost of solar cells and other solar energy conversion devices would have a dramatic impact on global CO_2 emissions.

One strategy for producing inexpensive solar energy conversion devices is to decouple the directions of light absorption and charge carrier collection, thereby allowing the use of low-cost materials that have low minority carrier diffusion lengths. This decoupling can, in theory, be accomplished by producing arrays of semiconductor wires having radial junctions, and simulations have shown that a significant benefit in efficiency should be possible for materials with diffusion lengths in the range of 1-10 μm. Although the efficiency improves under these conditions, it is partially lowered due to an expected loss in V_{oc} with increasing junction area.

Based on the simulation results, there are several fruitful avenues of research. One approach is to use a physical model system, such as macroporous silicon, in which all other factors but the junction geometry are held constant, in order to determine the effect of junction structure on carrier collection and V_{oc}. Demonstrating the efficiency of macroporous silicon samples would also confirm that no other deleterious effects are expected in high junction area devices. The controlled reduction of the minority carrier lifetime in physical model systems would also be a way to demonstrate the principle of decoupling charger carrier collection from light absorption. In addition to physical model systems, working on devices produced by inexpensive techniques, such as CVD, has the potential to show the feasibility of producing low-cost solar energy conversion devices by

using semiconductor wire arrays. These research directions are the primary ones pursued in this thesis and will be discussed in Chapters 2-5.

1.6 References

1. Forster, P.; Ramaswamy, V.; Artaxo, P.; Bernsten, T.; Betts, R.; Fahey, D. W.; Haywood, J.; Lean, J.; Lowe, D. C.; Myhre, G.; Nganga, J.; Prinn, R.; Raga, G.; Schulz, M.; Van Dorland, R., 2007: Changes in Atmospheric Constituents and in Radiative Forcing. *In: Climate Change 2007: The Physical Science Basis. Contribution to Working Group I to the Fourth Assessment Report of the Intergovernmental Panel on Climate Change* [Solomon, S., Qin, D., Manning, M., Chen, Z., Marquis, M., Averyt, K. B., Tignor, M., Miller, H. L. (eds.)]. Cambridge University Press, Cambridge, United Kingdom and New York, NY, USA.
2. Trenberth, K. E.; Jones, P. D.; Ambenje, P.; Bojariu, R.; Easterling, D.; Klein Tank, A.; Parker, D.; Rahimzadeh, F.; Renwick, J. A.; Rusicucci, M.; Soden, B.; Zhai, P., 2007: Observations: Surface and Atmospheric Climate Change. *In: Climate Change 2007: The Physical Science Basis. Contribution of Working Group I to the Fourth Assessment Report of the Intergovernmental Panel on Climate Change* [Solomon, S., Qin, D., Manning, M., Chen, Z., Marquis, M., Averyt, K. B., Tignor, M., Miller, H. L. (eds.)]. Cambridge University Press, Cambridge, United Kingdom and New York , NY, USA.
3. IPCC Fourth Assessment Report - Working Group I Report "The Physical Science Basis", 2007.
4. Sims, R. E. H.; Schock, R. N.; Adegbululgbe, A.; Fenhann, J.; Konstantinaviciute, I.; Moomaw, W.; Nimir, H. B.; Schlamadinger, B.; Torres-Martinez, J.; Turner, C.; Uchiyama, Y.; Vuori, S. J. V.; Wamukonya, N.; Zhang, X., 2007: Energy Supply. *In: Climate Change 2007: Mitigation. Contribution of Wroking Group III to the Fourth Assessment Report of the Intergovernmental Panel on Climate Change* [Metz, B., Davidson, O. R., Bosch, P. R., Dave, R., Meyer, L. A. (eds.)]. Cambridge University Press, Cambridge, United Kingdom and New York, NY, USA.
5. *CRC Handbook of Chemistry and Physics*; 77th ed.; Lide, D. R., Ed.; CRC Press: New York, 1996.

6. Goode, P. R.; Qiu, J.; Yurchyshyn, V.; Hickey, J.; Chu, M. C.; Kolbe, E.; Brown, C. T.; Koonin, S. E. *Geophys. Res. Lett.* **2001**, *28*, 1671-1674.
7. Tao, M., 2008: Inorganic Photovoltaic Solar Cells: Silicon and Beyond. *In: The Electrochemical Society Interface*
8. Schlosser, V. IEEE Trans. Electron Devices **1984**, 31, 610-613.
9. Sze, S. M. *Physics of Semiconductor Devices*; 2nd ed.; John Wiley & Sons: New York, 1981.
10. ASTM Standard G173, 2003e1, "Standard Tables for Reference Solar Spectral Irradiances: Direct Normal and Hemispherical on 37º Tilted Surface," ASTM International, West Conshohocken, PA, 2003, DOI: 10.1520/G0173-03E01.
11. Kayes, B. M.; Atwater, H. A.; Lewis, N. S. *J. Appl. Phys.* **2005**, *97*, 114302.
12. Tan, M. X.; Laibinis, P. E.; Nguyen, S. T.; Kesselman, J. M.; Stanton, C. E.; Lewis, N. S. In *Progress In Inorganic Chemistry, Vol 41*; John Wiley & Sons Inc: New York, 1994; Vol. 41, p 21-144.
13. Kenyon, C. N.; Tan, M. X.; Kruger, O.; Lewis, N. S. *J. Phys. Chem. B* **1997**, *101*, 2850-2860.
14. Kruger, O.; Kenyon, C. N.; Tan, M. X.; Lewis, N. S. *J. Phys. Chem. B* **1997**, *101*, 2840-2849.
15. Tan, M. X.; Kenyon, C. N.; Kruger, O.; Lewis, N. S. *J. Phys. Chem. B* **1997**, *101*, 2830-2839.
16. Tan, M. X.; Kenyon, C. N.; Lewis, N. S. *J. Phys. Chem.* **1994**, *98*, 4959-4962.
17. Lehmann, V. Electrochemistry of Silicon: Instrumentation, Science, Materials and Applications; Wiley-VCH, 2002.
18. Lehmann, V. *Thin Solid Films* **1995**, *255*, 1-4.
19. Lehmann, V.; Stengl, R.; Luigart, A. Mater. Sci. Eng. B-Solid State Mater. Adv. Technol. **2000**, 69, 11-22.
20. Lehmann, V. J. Electrochem. Soc. **1993**, 140, 2836-2843.
21. Lehmann, V.; Grüning, U. *Thin Solid Films* **1997**, *297*, 13-17.
22. Lehmann, V.; Föll, H. *J. Electrochem. Soc.* **1990**, *137*, 653-659.
23. Al Rifai, M. H.; Christophersen, H.; Ottow, S.; Carstensen, J.; Foll, H. *J. Electrochem. Soc.* **2000**, *147*, 627-635.

24. Wagner, R. S.; Ellis, W. C. Transactions of the Metallurgical Society of Aime **1965**, 233, 1053-&.

25. Wagner, R. S.; Ellis, W. C. *Appl. Phys. Lett.* **1964**, *4*, 89-&.

26. Cui, Y.; Lauhon, L. J.; Gudiksen, M. S.; Wang, J. F.; Lieber, C. M. *Appl. Phys. Lett.* **2001**, *78*, 2214-2216.

27. Wu, Y.; Cui, Y.; Huynh, L.; Barrelet, C. J.; Bell, D. C.; Lieber, C. M. *Nano Lett.* **2004**, *4*, 433-436.

28. Lombardi, I.; Hochbaum, A. I.; Yang, P.; Carraro, C.; Maboudian, R. *Chem. Mat.* **2006**, *18*, 988-991.

29. Kayes, B. M.; Filler, M. A.; Putnam, M. C.; Kelzenberg, M. D.; Lewis, N. S.; Atwater, H. A. *Applied Physics Letters* **2007**, 103110-1-3.

30. Spurgeon, J. M.; Plass, K. E.; Kayes, B. M.; Brunschwig, B. S.; Atwater, H. A.; Lewis, N. S. *Appl. Phys. Lett.* **2008**, *93*.

31. Gowrishankar, V.; Miller, N.; McGehee, M. D.; Misner, M. J.; Ryu, D. Y.; Russell, T. P.; Drockenmuller, E.; Hawker, C. J. *Thin Solid Films* **2006**, *513*, 289-294.

32. Plass, K. E.; Filler, M. A.; Spurgeon, J. M.; Kayes, B. M.; Maldonado, S.; Brunschwig, B. S.; Atwater, H. A.; Lewis, N. S. *Adv. Mater.* **2009**, *21*, 325-328.

33. Rahilly, W. P. Record of the Ninth IEEE Photovoltaic Specialists Conference|Record of the Ninth IEEE Photovoltaic Specialists Conference **1972**, 44-52|xii+388.

34. Green, M. A.; Wenham, S. R. *Appl. Phys. Lett.* **1994**, *65*, 2907-2909.

35. Wenham, S. R.; Green, M. A.; Edmiston, S.; Campbell, P.; Koschier, L.; Honsberg, C. B.; Sproul, A. B.; Thorpe, D.; Shi, Z.; Heiser, G. *Sol. Energ. Mat. Sol.* **1996**, *41-2*, 3-17.

36. Wohlgemuth, J.; Scheinine, A. Fourteenth IEEE Photovoltaic Specialists Conference 1980| Fourteenth IEEE Photovoltaic Specialists Conference 1980 **1980**, 151-5|1411.

37. Zheng, G. F.; Wenham, S. R.; Green, M. A. *Progress in Photovoltaics* **1996**, *4*, 369-373.

38. Takanezawa, K.; Hirota, K.; Wei, Q. S.; Tajima, K.; Hashimoto, K. *J. Phys. Chem. C* **2007**, *111*, 7218-7223.

39. Wei, Q. S.; Hirota, K.; Tajima, K.; Hashimoto, K. *Chem. Mat.* **2006**, *18*, 5080-5087.

40. Gur, I.; Fromer, N. A.; Geier, M. L.; Alivisatos, A. P. *Science* **2005**, *310*, 462-465.

41. Huynh, W. U.; Dittmer, J. J.; Alivisatos, A. P. *Science* **2002**, *295*, 2425-2427.

42. Kang, Y. M.; Park, N. G.; Kim, D. *Appl. Phys. Lett.* **2005**, *86*, 113101.

43. Lin, Y. T.; Zeng, T. W.; Lai, W. Z.; Chen, C. W.; Lin, Y. Y.; Chang, Y. S.; Su, W. F. *Nanotechnology (UK)* **2006**, *17*, 5781-5785.

44. Brabec, C. J.; Sariciftci, N. S.; Hummelen, J. C. *Adv. Funct. Mater.* **2001**, *11*, 15-26.

45. Kim, J. Y.; Lee, K.; Coates, N. E.; Moses, D.; Nguyen, T. Q.; Dante, M.; Heeger, A. J. *Science* **2007**, *317*, 222-225.

46. Li, G.; Shrotriya, V.; Huang, J. S.; Yao, Y.; Moriarty, T.; Emery, K.; Yang, Y. *Nat. Mater.* **2005**, *4*, 864-868.

47. Liang, Y.; Wu, Y.; Feng, D.; Tsai, S.-T.; Son, H.-J.; Li, G.; Yu, L. *J Am Chem Soc* **2009**, *131*, 56-7.

48. Haugeneder, A.; Neges, M.; Kallinger, C.; Spirkl, W.; Lemmer, U.; Feldmann, J.; Scherf, U.; Harth, E.; Gugel, A.; Mullen, K. *Phys. Rev. B* **1999**, *59*, 15346-15351.

49. Stelzner, T.; Pietsch, M.; Andra, G.; Falk, F.; Ose, E.; Christiansen, S. *Nanotechnology (UK)* **2008**, *19*.

50. Tsakalakos, L.; Balch, J.; Fronheiser, J.; Korevaar, B. A.; Sulima, O.; Rand, J. *Appl. Phys. Lett.* **2007**, *91*.

51. Garnett, E. C.; Yang, P. D. *J. Am. Chem. Soc.* **2008**, *130*, 9224-+.

52. Lewis, N. S.; Rosenbluth, M. L. In *Photocatalysis: Fundamentals and Applications*; Serpone, N., Pelizzetti, E., Eds.; Wiley Interscience: New York, 1989, p 45-121.

53. Pierret, R. F. *Advanced Semiconductor Fundamentals*; 2nd ed.; Prentice Hall: Upper Saddle River, NJ, 2003; Vol. 6.

54. Lewis, N. S. J. Electrochem. Soc. **1984**, 131, 2496-2503.

55. Rosenbluth, M. L.; Lewis, N. S. *J. Phys. Chem.* **1989**, *93*, 3735-3740.

56. Gstrein, F.; Michalak, D. J.; Royea, W. J.; Lewis, N. S. *J. Phys. Chem. B* **2002**, *106*, 2950-2961.

57. Groner, M. D.; Koval, C. A. *J. Electroanal. Chem.* **2001**, *498*, 201-208.

58. Gibbons, J. F.; Cogan, G. W.; Gronet, C. M.; Lewis, N. S. *Appl. Phys. Lett.* **1984**, *45*, 1095-1097.

59. Gronet, C. M.; Lewis, N. S.; Cogan, G. W.; Gibbons, J. F. *Proc. Natl. Acad. Sci.* **1983**, *80*, 1152-1156.

60. Rosenbluth, M. L.; Lieber, C. M.; Lewis, N. S. *Appl. Phys. Lett.* **1984**, *45*, 423-425.

61. Cogan, G. W.; Gronet, C. M.; Gibbons, J. F.; Lewis, N. S. *Appl. Phys. Lett.* **1984**, *44*, 539-541.

62. Bard, A. J.; Faulkner, L. R. *Electrochemical Methods: Fundamentals and Applications*; 2nd ed.; John Wiley & Sons, Inc.: Hoboken, NJ, 2001.

63. Hamann, T. W.; Gstrein, F.; Brunschwig, B. S.; Lewis, N. S. *J. Am. Chem. Soc.* **2005**, *127*, 7815-7824.

64. Oregan, B.; Gratzel, M. *Nature* **1991**, *353*, 737-740.

65. Gratzel, M.; Kalyanasundaram, K. *Curr. Sci.* **1994**, *66*, 706-714.

66. Hagfeldt, A.; Gratzel, M. *Accounts Chem. Res.* **2000**, *33*, 269-277.

67. Gratzel, M. J. Photochem. Photobiol. C-Photochem. Rev. **2003**, 4, 145-153.

68. Baxter, J. B.; Aydil, E. S. *Appl. Phys. Lett.* **2005**, *86*.

69. Law, M.; Greene, L. E.; Johnson, J. C.; Saykally, R.; Yang, P. D. *Nat. Mater.* **2005**, *4*, 455-459.

70. Law, M.; Greene, L. E.; Radenovic, A.; Kuykendall, T.; Liphardt, J.; Yang, P. D. *J. Phys. Chem. B* **2006**, *110*, 22652-22663.

71. Beermann, N.; Vayssieres, L.; Lindquist, S. E.; Hagfeldt, A. *J. Electrochem. Soc.* **2000**, *147*, 2456-2461.

72. Erné, B. H.; Vanmaekelbergh, D.; Kelly, J. J. *J. Electrochem. Soc.* **1996**, *143*, 305-314.

73. Erné, B. H.; Vanmaekelbergh, D.; Kelly, J. J. *Adv. Mater.* **1995**, *7*, 739-742.

74. Goodey, A. P.; Eichfeld, S. M.; Lew, K. K.; Redwing, J. M.; Mallouk, T. E. *J. Am. Chem. Soc.* **2007**, *129*, 12344-+.

75. Dalchiele, E. A.; Martín, F.; Leinen, D.; Marotti, R. E.; Ramos-Barrado, J. R. *J. Electrochem. Soc.* **2009**, *156*, K77-K81.

Chapter 2

Macroporous Silicon as a Model System for Silicon Wire Array Solar Cells

2.1 Abstract

Macroporous silicon samples have been investigated in photoelectrochemical cells, and their behavior has been compared to that of conventional, planar, Si/liquid junctions. The liquid electrolyte junction provided a conformal contact to the macroporous Si, and allowed assessment of the trade-offs between increased surface area and decreased carrier collection distances in such systems relative to the behavior of planar semiconductor/ liquid photoelectrochemical junctions. The electrolyte contained the dimethylferrocene/ dimethylferrocenium redox system in methanol because this system has been shown previously to produce bulk recombination-diffusion limited contacts at planar Si(100) electrodes under 100 mW cm^{-2} of simulated air mass 1.5 illumination. Introduction of a network of ~2-3 μm diameter, ~80 μm long pores into the Si was found to slightly reduce the short-circuit photocurrent density and the open-circuit voltage of the system, but energy-conversion efficiencies in excess of 10% were nevertheless obtained from such samples. This system therefore validates the concept of using interpenetrating networks to produce efficient solar energy conversion devices in systems that do not have long carrier collection distances.

2.2 Introduction

A key constraint in planar solar cell designs is that the minority-carrier collection length, including both the diffusion length and the width of the electric-field region, must be comparable to, or preferably should exceed, the absorption depth of the material for the relevant photon energies of the solar spectrum. In typical planar-junction devices, this restriction imposes a purity related, and therefore an associated cost-related, constraint on the absorber material, because the diffusion length in the absorber must be sufficient to allow photogenerated carriers to arrive in the space-charge region, where they can be effectively separated and ultimately collected at the external contacts.

One approach to enable the use of cheaper materials in solar cells involves orthogonalization of the directions of light absorption and charge-carrier collection. For example, in an oriented array of semiconductor nanorods having radial p-n junctions, the light can be absorbed along the long axis of the rod, whereas the charge carriers can diffuse a short distance radially to the junction (Figure 2.1). In this design, devices exhibiting high energy-conversion efficiencies can in principle be produced from an absorber material that has a much smaller diffusion length than that needed for high efficiency in a planar solar cell configuration. Specifically, an analytical study of the governing generation, transport, and recombination equations has shown that high efficiencies can be maintained in oriented rod array solar cells provided that the diffusion length in the material is comparable to the radius of the rod.[1] Materials with diffusion lengths as low as 100 nm, or even 10 nm, can thus in principle be used in efficient solar cells, provided that the rods are sufficiently small in diameter. The principle applies to

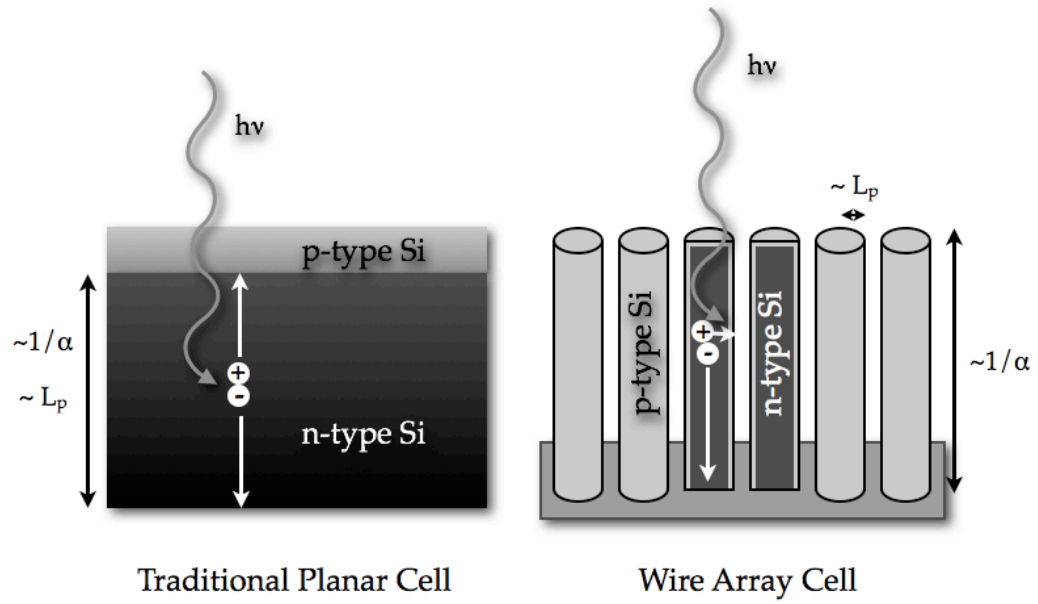

Figure 2.1. *Schematic drawing of the difference between a traditional planar solar cell and a wire array solar cell. In the planar cell, the minority carrier diffusion length (L_p) must be comparable to the absorption length (1/α). In the wire array cell, the minority carriers can diffuse radially to the junction, while light is still absorbed along the axial dimension of the wire.*

indirect band-gap semiconductors, such as Si, for which an increased diffusion length is associated with an increased purity and cost of the absorber material, and applies to earth-abundant, inexpensive materials, such as Fe_2O_3,[2] that are generally nonstoichiometric and therefore have short diffusion lengths.

The nanorod-based solar cell design does, however, involve a design rule trade-off. Relaxation of the constraint on the purity of the absorber material comes at the expense of a larger surface area per unit of projected area of the device. To obtain high energy-conversion efficiencies, analytical simulations have shown that the rod array device design requires very low surface recombination velocities as well as extremely low junction recombination rates.[1] Increased carrier collection has been observed previously for porous n-GaP and n-SiC photoelectrodes in anodic photocorrosion processes,[3-5] but

there is no information on whether the open-circuit voltage of stable, regenerative photoelectrochemical cells is degraded as a result of the introduction of porosity to the electrode material. To date, photovoltaic cells have been made from nanorods of CdSe, CdTe, Fe_2O_3, TiO_2, and ZnO, but demonstrated efficiencies in such systems are less than 5%, and typically less than 1-2%.[6-13] Although the modest observed energy-conversion efficiencies are believed to primarily reflect poor light harvesting efficiencies in the structures prepared to date, it is not clear whether the observed efficiencies are also influenced by too low diffusion lengths for the nanorod radii employed to date, excessive junction or surface recombination, and/or whether the analytical description of this device design has omitted a key physical process that prevents efficient photovoltaic performance from being obtained through the wire array approach.

In this work, we have investigated a model light absorption and charge-carrier orthogonalization device implementation using macroporous Si as the light-absorbing medium. Macroporous Si can be made from bulk Si wafers, whose purity and diffusion length can be controlled, and measured, prior to fabrication of the pillared, light absorbing, phase.[14] The junctions have been made using CH_3OH that contains the 1,1'-dimethylferrocenenium/ferrocene ($Me_2Fc^{+/0}$) redox couple, because such liquid junctions conform to the morphology of the pillared light absorber. Additionally, the CH_3OH-$Me_2Fc^{+/0}$ system has been shown to create an inversion layer on n-type Si(100) surfaces, producing an in-situ p^+-n junction structure having sufficiently low interfacial and junction recombination rates to produce bulk diffusion-limited open-circuit voltages of ~670 mV under 100 mW cm^{-2} of air mass (AM) 1.5 illumination.[15,16]

Porous silicon can be fabricated from a wide variety of bulk Si materials.[14,17-23] Although microporous silicon has been studied more extensively due to its potential applications to optoelectronics and sensors,[24-29] macroporous silicon is better-suited as a model system for evaluating the orthogonalized photovoltaic device design principles because the geometric structure of macroporous Si more closely resembles that of free-standing Si rods. By etching a planar, bulk Si substrate in HF(aq) under back-side illumination, n-type Si can be etched to produce long, straight-walled, uniform pores having micron-sized dimensions.[14,17,18,20,23] The pore formation in n-type silicon is believed to occur through a hole-limited silicon dissolution process.[14,17,19-22,28,30,31] As pores develop in the sample, holes generated at the back diffuse through the silicon and are preferentially harvested at the pore tips, where the tip curvature causes the electric field to be the largest.[28,30,31] The space between the pores is believed to be completely depleted, inhibiting holes from diffusing between the pores to dissolve the sidewalls.[14,28] The pore diameter and spacing can be controlled by the current density of the etching, the applied voltage, and the doping of the sample, while the pore length can be controlled independently by adjusting the etching time.[28] Thus, samples having different pore lengths, but similar pore structures, can be fabricated and used as working electrodes in photoelectrochemical energy conversion devices.

The behavior of silicon photoelectrodes has been explored extensively.[15,32-41] Systems using methanol as the solvent, $LiClO_4$ as the supporting electrolyte, and ferrocene/ferrocenium derivatives have achieved energy conversion efficiencies of 10-14%.[32,36,37] The highest efficiencies (14.1%) have been achieved using thin-layer two-

electrode photoelectrochemical solar cells, which minimize many of the mass transport, resistance, and optical absorption issues encountered in more traditional three-electrode, potentiostatically controlled, electrochemical systems.[32] The thin-layer set-up is not well-suited for reproducibly testing a large number of different types of porous samples, however, so the more common three-electrode cell was used for the experiments described herein. Efficiencies of 7.8% have been previously observed using this cell geometry for polished, planar n-Si(100) samples in contact with (1-hydroxy)ethylferrocene$^{+/0}$ in CH_3OH.[37] Higher efficiencies have been obtained by etching the samples to reduce optical reflection losses, and by use of more highly doped substrates to minimize bulk recombination. Dimethylferrocene$^{+/0}$ ($Me_2Fc^{+/0}$) in methanol is known to form large barrier heights (~1 V) in contact with n-Si surfaces.[42] These large barrier heights have been shown to result in low surface recombination, due to the low concentration of majority carriers at the surface of the sample.[16] In addition, some of the surface passivation persists after the sample is removed from solution, implying that the surface is modified with methoxy groups as a result of exposure to the solution.[16] These characteristics make the CH_3OH-$Me_2Fc^{+/0}$ system an attractive choice for the comparison of behavior of macroporous Si and planar Si photoelectrodes. Samples of macroporous Si with varying pore lengths have been investigated, and the results have been compared to the behavior of planar (100)- and (110)-oriented silicon samples in the same electrolyte solution. In addition, cyclic voltammetry has been used to evaluate the internal junction area and carrier transport distances of the macroporous Si photoelectrodes relative to those of planar Si samples.

2.3 Experimental

2.3.1 Reagents

Methanol (BakerDry, Baker, Phillipsburg, NJ), sodium dodecylsulfate (SDS) (Sigma-Aldrich, St. Louis, MO), 49% (27 M) HF(aq) (Transene, Inc., Danvers, MA), and buffered HF(aq) (Transene) were used without further purification. Water (18 MΩ cm resistivity) was obtained from a Barnstead Nanopure system. Lithium perchlorate, $LiClO_4$ (Sigma-Aldrich), was fused under vacuum and stored under an inert atmosphere until use. Me_2Fc (Sigma-Aldrich) was sublimed at ~ 45 ºC under vacuum and was stored under an inert atmosphere until use. Dimethylferrocenium tetrafluoroborate (Me_2FcBF_4) was synthesized from Me_2Fc by addition of excess HBF_4 in the presence of 0.5 equivalents of benzoquinone. The reaction was conducted under argon in an ice-water bath. The resulting solid was dried under vacuum and stored in an inert atmosphere. Me_2Fc and Me_2FcBF_4 were stored in light-protected bottles.

Silicon (Czochralski, n-type, (100)-oriented, P-doped) was obtained from either Virginia Semiconductor (Fredericksburg, VA, 1-10 Ω cm resistivity) or Wacker Siltronic (Munich, Germany, 4-8 Ω cm resistivity). Silicon (float zone, n-type, (110)-oriented, P-doped, 0.7-1.3 Ω cm resistivity) was obtained from the Institute of Electronic Materials Technology (ITME, Warsaw, Poland). The Si-(100) wafers were 500 ± 25 μm thick, polished on one side, and had measured resistivities between 5 and 7 Ω cm. The Si-(110) wafers were 250 ± 25 μm thick, polished on both sides, and had resistivities of 0.8 Ω cm.

2.3.2 Fabrication of Macroporous Silicon

Etching of planar Si was performed in an aqueous solution of 5% HF(aq) that contained 10 mM SDS. The etching was performed potentiostatically at 5 V, with vigorous stirring, in a teflon cell equipped with a Pt counter/pseudoreference electrode. Prior to etching, the teflon cell, o-rings, and Pt mesh counter electrode were cleaned in aqua regia (3:1 HCl:HNO_3 by volume) for 30 min. Silicon samples were rinsed sequentially with water, methanol, acetone, methanol, and water, and were then dried under a stream of N_2(g). Approximately 2 cm^2 of the polished side of the Si was then exposed to the etching solution.

The illumination intensity was adjusted to maintain a constant 10 mA cm^{-2} of current during etching, with the light intensity controlled by connecting the lamp power supply to a variable resistor. Samples were etched for 15, 30, 45, or 60 min. The samples were then rinsed thoroughly in water and dried under a stream of N_2(g). To remove the microporous Si layer, the samples were etched in 10% KOH(aq) for 10-20 s, and were then rinsed sequentially with water, methanol, acetone, methanol, and water, followed by drying under a stream of N_2(g).

2.3.3 Scanning Electron Microscopy

Scanning electron microscopy (SEM) data were obtained using a LEO 1550 VP Field Emission SEM (FE SEM) using the in-lens detector at an accelerating voltage of 10 kV. Porous samples were scored on the back and cracked along the (100) directions to obtain cross sectional images, and the resulting pieces were mounted to the SEM stub using carbon tape.

2.3.4 Preparation of Photoelectrodes

For photoelectrochemistry, the planar and macroporous silicon samples were scored and cracked to produce ~ 5 mm x 5 mm electrodes. The samples were then etched for 30 s in buffered HF(aq), rinsed with water, and dried under a stream of N_2(g). Ga/In eutectic was then immediately scratched into the back-side of the samples. Ag paint was then used to affix the back of each sample to a coil of tinned Cu wire. The front surface of the samples was covered with Epoxies, Etc. (Cranston, RI) 20-3004 LV epoxy to leave an exposed area of ~ 1-2 mm^2. The silicon sample and the Cu wire were then sealed in a glass tube using Hysol 1C epoxy (Loctite, Rocky Hill, CT), with the sample surface oriented perpendicular to the long axis of the glass tube. Most of the LV epoxy was covered with Hysol epoxy. The LV epoxy was needed due to the tendency of the Hysol epoxy to form bubbles on the porous Si surface. Both epoxies are opaque and resistant to methanol, and the Hysol epoxy provided strong structural support. Before use in photoelectrochemical experiments, electrodes were allowed to cure for at least 24 h at room temperature. The projected area of each electrode was measured by taking an image at 800 dpi of the electrodes and a 1 cm x 1 cm calibration square, using a flat-bed scanner, and analyzing the resulting image using the Image SXM software.

2.3.5 Photoelectrochemistry

Photoelectrochemical experiments were conducted in a sealed glass cell under a positive pressure of Ar. The measurement solution (CH_3OH, 1 M $LiClO_4$, 200 mM Me_2Fc, ~0.1 mM Me_2FcBF_4) was prepared and introduced into the measurement cell under an inert atmosphere. Silicon electrodes were etched (30 s in buffered HF(aq) for

planar samples; 2 min in 1:1 (v:v) 27 M HF(aq):ethanol for porous samples) to remove the native oxide, rinsed with water, and then thoroughly dried under a stream of N_2(g). The electrodes were then immediately introduced into the cell (Figure 2.2), under a positive flow of Ar. The reference electrode was a Luggin capillary, with an outer tip diameter of ~ 100 μm, that contained a Pt wire and a sample of the same solution as in the working electrode compartment. A Pt mesh was used as a counter electrode. The cell had a flat quartz bottom, and the working and reference electrodes were positioned as close as possible to the bottom of the cell, with the tip of the Luggin capillary directly underneath the Si surface and as close as possible to the Si without touching its surface. The solution was stirred vigorously during all data collection.

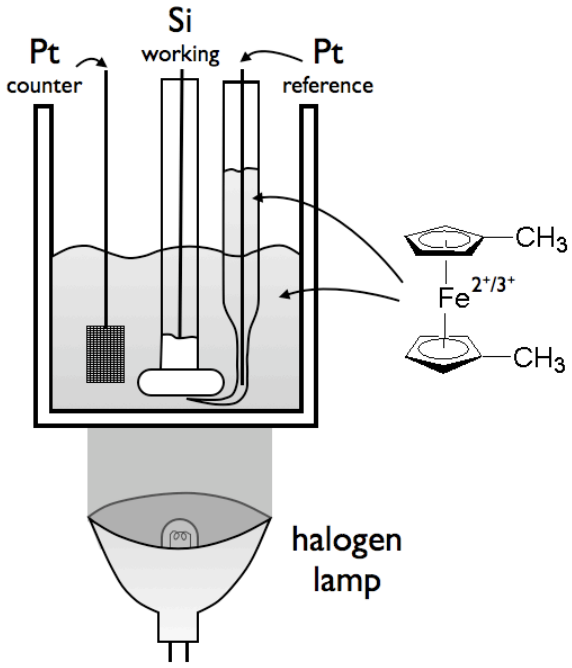

Figure 2.2. *Schematic diagram of the photoelectrochemical cell employed. The bottom window of the cell was quartz, and illumination was from a 300 W ELH bulb at 100 mW/cm^2. The cell contained 200 mM Me_2Fc, ~ 0.1 mM Me_2FcBF_4, and 1.0 M $LiClO_4$ in anhydrous methanol. The Luggin capillary was filled with the same solution. The cell was stirred vigorously during measurements and kept under positive pressure of Ar.*

Illumination of the bottom of the cell was provided by a 300 W ELH-type W-halogen bulb equipped with a dichroic rear reflector.[43] The illumination intensity was measured using a calibrated Si photodiode that was in turn calibrated relative to a

secondary standard Si solar cell. The secondary standard Si solar cell had been calibrated by an independent calibration laboratory with respect to a reference AM 1.0 spectrum at 100 mW cm^{-2} of illumination intensity. For Si photoelectrodes in this same cell configuration and electrolyte/redox system, this calibration method has been shown previously to produce short-circuit photocurrent densities that are very close to those obtained under the same intensity of actual sunlight.[32,37]

All current density-potential (*J-E*) measurements were recorded using a Solartron model 1287 potentiostat. In a typical experiment, the *J-E* behavior of the electrode was measured at 10 mV s^{-1} in the dark, then under ~10 mW cm^{-2} of illumination, followed by a measurement under 100 mW cm^{-2} of illumination, and then measured again in the dark. The open-circuit voltage, V_{oc}, was measured between each *J* vs *E* measurement. The short-circuit current density, J_{sc}, was calculated as the average current density for potentials within 10^{-4} V of 0 V versus the Nernstian potential of the cell. The values of V_{oc} and the presented *J-E* behavior are reported with respect to the Nernstian cell potential, which was measured with respect to the reference electrode for each working electrode. The Nernstian potential was typically 10-30 mV vs. the reference electrode potential, due to drift in the composition of the cell solution compared to the composition of the solution in the Luggin capillary. The point of maximum power was calculated as the average of 10 data points, after eliminating the 10 largest measured points (to remove any erroneous spikes). The efficiency and fill factor were calculated by conventional methods. The *J-E* data shown in the figures were obtained on representative samples, while the values reported in the text and tables for J_{sc}, V_{oc}, fill factors, and energy

conversion efficiencies are the means of values measured on six electrodes for each type (three for (110) samples), with the error reported as the standard error of the mean.

Cyclic voltammograms were collected at various scan rates under the same conditions used for the *J-E* data, except that the solution composition was 1.0 M $LiClO_4$ with 0.3 mM Me_2Fc in CH_3OH, with no Me_2FcBF_4 initially present, and the solution was not stirred. Scans were collected using a Princeton Applied Research Model 173 potentiostat with a Model 175 programmer interfaced to a DAQ card. All experiments were conducted under >100 mW cm^{-2} of ELH-type illumination, with identical illumination conditions for all samples. The reported cyclic voltammetric data are the average of the behavior for three electrodes for each sample type, with the error bars representing the standard error of the mean. The diffusion coefficient of Me_2Fc in methanol was calculated from the measured steady-state current at a Pt microelectrode under similar conditions.

2.3.6 Correction for Series Resistance and Concentration Overpotential

Corrections for concentration overpotential and series resistance losses were performed according to equations (2.1) and (2.2):[44]

$$\eta_{conc} = \frac{k_B T}{nq}\left\{\ln\left(\frac{J_{l,a}}{-J_{l,c}}\right) - \ln\left(\frac{J_{l,a} - J}{J - J_{l,c}}\right)\right\} \tag{2.1}$$

$$E_{corr} = E_{meas} - iR_S - \eta_{conc} \tag{2.2}$$

where k_B is Boltzmann's constant, T is the absolute temperature, q is the charge on an electron, n is the number of electrons transferred in the redox process (n = 1 for Me_2Fc), $J_{l,c}$ and $J_{l,a}$ are the cathodic and anodic limiting current densities, respectively, and R_s is

the series resistance. The limiting cathodic and anodic current densities were determined as -0.2 mA cm^{-2} and 60 mA cm^{-2}, respectively, by use of a Pt foil working electrode in the same geometry as the Si working electrode, in contact with the same electrolyte solution and in the same cell configuration. The series resistance was calculated by using equation (2.1) to correct the *J-E* data obtained using the Pt electrode for concentration overpotential losses. The inverse of the slope of the linear portion of the resulting *J-E* data, around 0 V vs the cell potential, was then evaluated to produce a value for R_s. Although the series resistance varied from measurement to measurement, due primarily to small differences in the placement of the Luggin capillary, the value was typically in the range of 130-180 Ω. To minimize the possibility of overcorrection, a value of 100 Ω was chosen as the value of the series resistance used in the calculations. This value should be an underestimate of the actual series resistance, particularly because the contact resistance and the series resistance of the silicon are not accounted for by the resistance data obtained using the platinum working electrode. Hence, the photoelectrode efficiencies calculated herein are conservative. Correction of the observed *J-E* behavior at the Si photoelectrodes for both series resistance and concentration overpotentials thus produced the values of E_{corr} reported herein for each measured potential, E_{meas}.

2.3.7 Analysis of Cyclic Voltammograms

The lithographic-galvanic (LIGA) electrodes analyzed by Neudeck and Dunsch in terms of their cyclic voltammetry behavior are similar to the porous electrodes used in this study.[45] The LIGA electrodes are hexagonal arrays of pores with regular pore dimensions and pore-pore spacing. The porous electrodes used in this study, although not

regular in pore dimension and spacing, are structurally similar, and therefore their normalized peak current behavior with respect to scan rate can be modeled using the same approach.

Derivation of the expression for the peak potential requires several equations that relate the dimensionless radius, p, to the dimensionless potential, ξ, and the dimensionless current ψ, under various conditions. These quantities can be defined as:

$$p = r\sqrt{\frac{nFv}{RTD}} \tag{2.3}$$

$$\xi = -\frac{nF}{RT}\left(E - E^0\right) \tag{2.4}$$

$$\psi = \frac{I}{nFAc\sqrt{nFvD/RT}} \tag{2.5}$$

where r is the radius of the electrode, n is the number of moles of electrons involved in the reaction (n = 1 for Me_2Fc), F is Faraday's constant, v is the scan rate, R is the gas constant, T is the absolute temperature, D is the diffusion coefficient (measured to be 1.02 x 10^{-5} cm^2 s^{-1} for Me_2Fc in methanol), E is the electrode potential, E^0 is the standard potential, A is the electrode area, and I is the current.

For a tubular electrode, at the peak potential, one obtains:

$$\xi_{tube,p} = 1.11\frac{\tanh\left[2.589\left(\log[p] - 0.4318\right)\right] + 1}{2} \tag{2.6}$$

$$\psi_{tube,p} = 0.446\frac{\tanh\left[1.755\left(\log[p] - 0.2706\right)\right] + 1}{2} \tag{2.7}$$

The dimensionless tubular current at the peak current for a planar electrode is given by:

$$\psi_{tube,1.11} = 0.446\frac{\tanh\left[1.999\left(\log[p] - 0.3285\right)\right] + 1}{2} \tag{2.8}$$

Finally, calculating the dimensionless charge at a tubular electrode at the peak potential for tubular and planar electrodes yields:

$$q_{tube,p} = 0.529 - 0.493\frac{\tanh\left[2.271\left(\log[p] - 0.2706\right)\right] + 1}{2} \tag{2.9}$$

$$q_{tube,1.11} = 0.781 - 0.747\frac{\tanh\left[2.063\left(\log[p] - 0.6965\right)\right] + 1}{2} \tag{2.10}$$

These quantities enable calculation of the peak current at a LIGA-produced macroporous metallic electrode, which will be used to approximate the mass-transport-limited current at a macroporous silicon electrode under high levels of illumination. Defining s_w as the pore width, s_b as the pore-pore spacing, and s_h as the pore length, along with $R_h = s_h/s_w$ and $R_b = s_b/s_w$, produces an expression for the peak potential at a LIGA electrode as:

$$\xi_{LIGA,p}\left[R_b, R_h, p\right] = \xi_{tube,p}[p] + \frac{0.446\left(1.11 - \xi_{tube,p}[p]\right)}{0.446 + \psi_{part}\left[R_b, R_h, p\right]} \tag{2.11}$$

where

$$\psi_{part}\left[R_b, R_h, p\right] = \frac{2R_h\psi_{tube,p}[p]}{\left(1 + R_b\right)^2} \tag{12}$$

The dimensionless partial current and charge in the pores can then be approximated as follows:

$$\psi_{tube}^{LIGA,p}\left[R_b, R_h, p\right] = f_{\text{int}}\left[1.11, \psi_{tube,1.11}[p], \xi_{tube,p}[p], \psi_{tube,p}[p], \xi_{LIGA,p}\left[R_b, R_h, p\right]\right] \tag{2.13}$$

$$q_{tube}^{LIGA,p}\left[R_b, R_h, p\right] = f_{\text{int}}\left[1.11, q_{tube,1.11}[p], \xi_{tube,p}[p], q_{tube,p}[p], \xi_{LIGA,p}\left[R_b, R_h, p\right]\right] \tag{2.14}$$

where

$$f_{\text{int}}\left[x_1,y_1,x_2,y_2,x\right]=y_1+\frac{\left(y_2-y_1\right)\left(x-x_1\right)}{\left(x_2-x\right)} \tag{2.15}$$

The dimensionless current at a planar electrode can be approximated by:

$$\psi_{disc}=0.3801-0.1251\xi-0.0642\xi^2+0.00439\xi^3 \tag{2.16}$$

Given these values, the dimensionless peak current at the LIGA electrode can be calculated using:

$$\begin{aligned}&\psi_{LIGA,p}\left[R_b,R_h,p\right]=\psi_{disc}\left[\xi_{LIGA,p}\left[R_b,R_h,p\right]\right]\\&+\left(2R_h\psi_{tube}^{LIGA,p}\left[R_b,R_h,p\right]+\psi_{disc}\left[\xi_{LIGA,p}\left[R_b,R_h,p\right]\right]\times\left(q_{ttube}^{LIGA,p}\left[R_b,R_h,p\right]-1\right)\right)\\&\times\left(\left(1+R_b\right)^2\right)^{-1}\end{aligned} \tag{2.17}$$

The peak current is then given by:

$$I_{LIGA,p}=nFA_{disc}c\sqrt{\frac{nFvD}{RT}}\times\psi_{LIGA,p}\left[R_b,R_h,\frac{s_w}{2}\sqrt{\frac{nFv}{RTD}}\right] \tag{2.18}$$

where A_{disc} is the projected area of the electrode. Equation (2.18) can be rearranged to obtain the desired result in terms of the normalized peak current:

$$J_{p,proj}=\frac{I_{LIGA,p}}{A_{disc}}=nFc\sqrt{\frac{nFvD}{RT}}\times\psi_{LIGA,p}\left[R_b,R_h,\frac{s_w}{2}\sqrt{\frac{nFv}{RTD}}\right] \tag{2.19}$$

These calculations were performed to fit the peak currents for the porous electrodes normalized by their projected area, $J_{\text{p,proj}}$. At each scan rate, the expected peak currents were calculated based on the equations above, and the sum of the squares of the deviations from the measured data was calculated. The value of s_b (which approximates the pore-pore spacing) was then systematically varied to obtain the minimum sum of squares value, while all other parameters were held constant. Each fit always produced a

clear minimum in the sum of squares with respect to s_b, typically at $s_b \approx 2$ μm, which is consistent with the pore-to-pore spacing observed in the SEM images.

2.4 Results

2.4.1 Morphology of the Macroporous Silicon Samples

Figure 2.3 depicts the macroporous Si samples obtained from the anodic etching process. The pores were ~2-3 μm diameter, approximately circular in cross-section, and reasonably uniform over large areas. In addition to fully developed pores, circular etch pits (light gray in Figure 2.3) were observed, which is expected for anodization of n-type

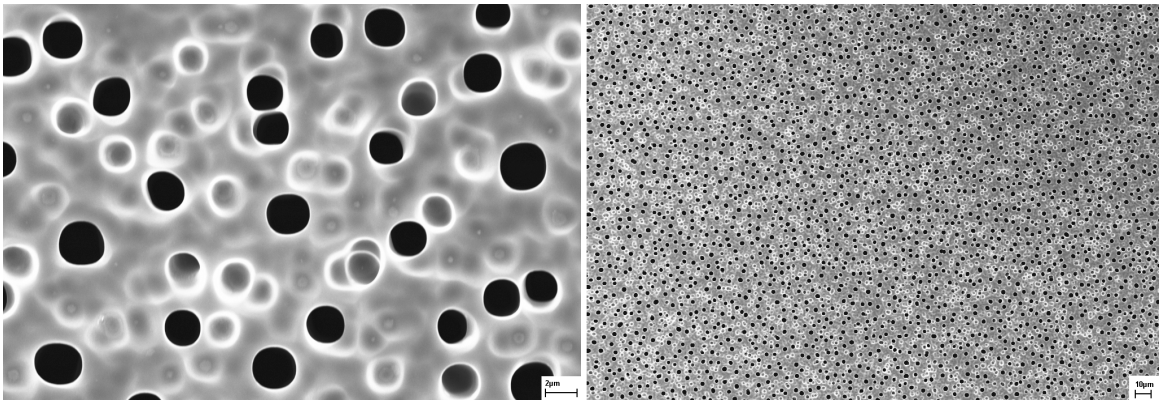

Figure 2.3. *Left: Plan view of macroporous silicon etched for 30 min at 10 mA cm^{-2}. The scale bar is 2 μm. Right: Plan view showing the consistency of the porous surface over a large area. The scale bar is 10 μm.*

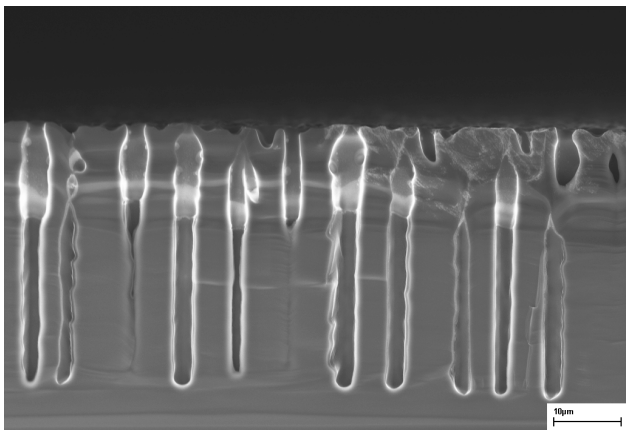

Figure 2.4. *Cross sectional view of macroporous silicon etched for 30 min at 10 mA cm^{-2}. The scale bar is 10 μm.*

silicon under back-side illumination without prior formation of lithographically defined etch pits.[14] Cross-sectional SEM data indicated that the pores were approximately the same length across a given sample, with only minimal branching (Figure 2.4).

Anodization of the samples for 15, 30, 45, and 60 min, respectively, under otherwise nominally identical conditions, produced pores of increasing length. Over the range of times investigated, the pore length varied linearly with etching time (Figure 2.5), and a maximum pore length of ~85 μm was obtained for the times used in this study. However, the pore diameter was nearly independent of etch time.

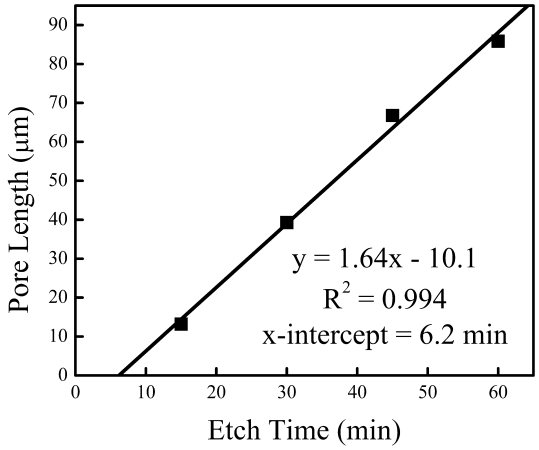

Figure 2.5. *Plot of pore length vs. etch time. The growth rate was ~1.6 μm min^{-1}, with a pore initiation time of ~6 min.*

The time intercept of a fit of pore length vs. time was ~6 min, which is consistent with a pore initiation phase during the initial etching, followed by uniform pore growth. The illumination intensity required to produce 10 mA cm^{-2} of current density dropped rapidly after 6-8 min of etching time, and then dropped much more slowly thereafter. These observations are consistent with a pore initiation phase followed by a steady pore growth phase.

2.4.2 *J-E* Behavior

Figure 2.6 shows the *J-E* behavior of planar (100)- and (110)-oriented n-Si samples, and of macroporous Si electrodes made from (100) n-Si, in contact with the CH_3OH-

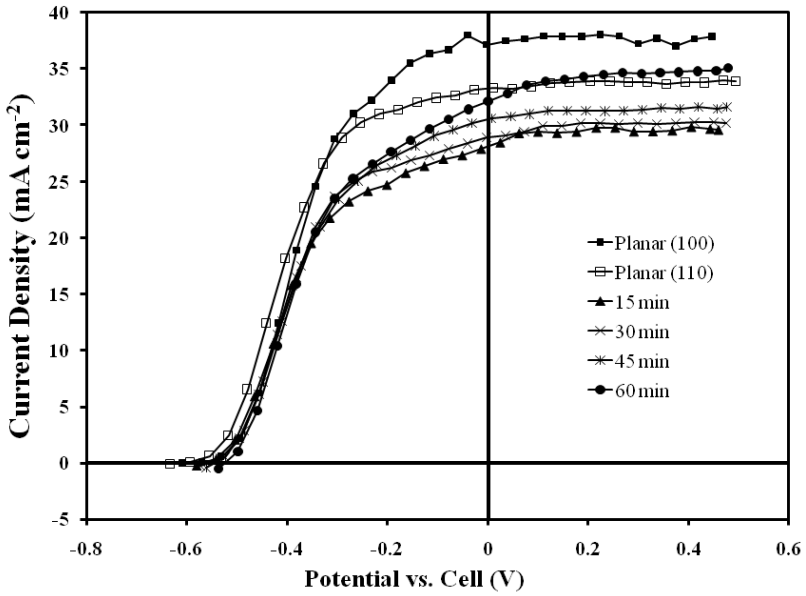

Figure 2.6. *J-E data at 10 mV s^{-1} under 100 mW cm^{-2} of illumination.*

$Me_2Fc^{+/0}$ electrolyte under 100 mW cm^{-2} of ELH-type simulated AM 1.5 illumination. The short-circuit photocurrent densities were 5-7 mA cm^{-2} lower for the macroporous samples than for the planar (100) sample, but J_{sc} was relatively independent of the pore length.

The open-circuit voltage decreased slightly as the pore length increased, however V_{oc} was still greater than 480 mV even for samples with the longest pores (Table 2.1).

Table 2.1. *Figures of merit for raw data*

Etch Time	J_{sc} (mA cm^{-2})	V_{oc} (mV)	Fill Factor (%)	Efficiency (%)
Planar (100)	36.2 ± 2.6	566 ± 2	44.6 ± 1.6	9.1 ± 0.5
15 min	30.6 ± 1.7	552 ± 3	46.0 ± 1.6	7.7 ± 0.3
30 min	29.4 ± 0.9	543 ± 3	44.8 ± 1.9	7.1 ± 0.2
45 min	29.3 ± 1.2	517 ± 8	42.4 ± 1.3	6.4 ± 0.3
60 min	31.5 ± 1.8	485 ± 12	41.3 ± 0.8	6.3 ± 0.5
Planar (110)	31.8 ± 0.8	601 ± 2	46.2 ± 0.9	8.8 ± 0.2

Planar samples exhibited V_{oc} values of 566 mV for the (100)-oriented samples and 600 mV for the (110)-oriented samples. Both of these values are near the bulk recombination/ generation limit for the injection level and the doping level in each sample, which are 573 mV and 612 mV for the (100) and (110) samples, respectively.[36] In contrast, macroporous Si samples that had been etched for 60 min from the same stock as the (100)-oriented planar Si samples exhibited $V_{oc} \sim 485$ mV.

Under 100 mW cm^{-2} of ELH-type simulated solar illumination, all of the *J-E* data exhibited small limiting cathodic current densities, due to the very small concentration of electron acceptor in the solution (~0.1 mM of Me_2Fc^+). Photoelectrode energy conversion efficiencies from these data have been shown previously to underestimate the actual energy conversion performance of such systems, due to the appreciable concentration overpotentials and series resistance losses in this cell configuration.[32,36,46] Consistently, the fill factors of both the planar and porous photoelectrodes increased as the light intensity was lowered to 10 mW cm^{-2}, in accord with expectations for reduced current-dependent losses in the cell at lower J_{sc} values.

Table 2.2. *Figures of merit for corrected data*

Etch Time	J_{sc} (mA cm^{-2})	V_{oc} (mV)	Fill Factor (%)	Efficiency (%)
Planar (100)	36.4 ± 2.6	566 ± 2	70.3 ± 1.4	14.4 ± 0.9
15 min	32.6 ± 2.0	552 ± 3	69.1 ± 2.0	12.2 ± 0.7
30 min	30.7 ± 1.2	543 ± 3	68.9 ± 3.1	11.4 ± 0.5
45 min	30.7 ± 1.4	517 ± 8	64.7 ± 1.9	10.2 ± 0.5
60 min	34.0 ± 2.0	485 ± 12	63.9 ± 1.8	10.6 ± 0.8
Planar (110)	32.1 ± 1.1	601 ± 2	73.7 ± 2.9	14.2 ± 0.4

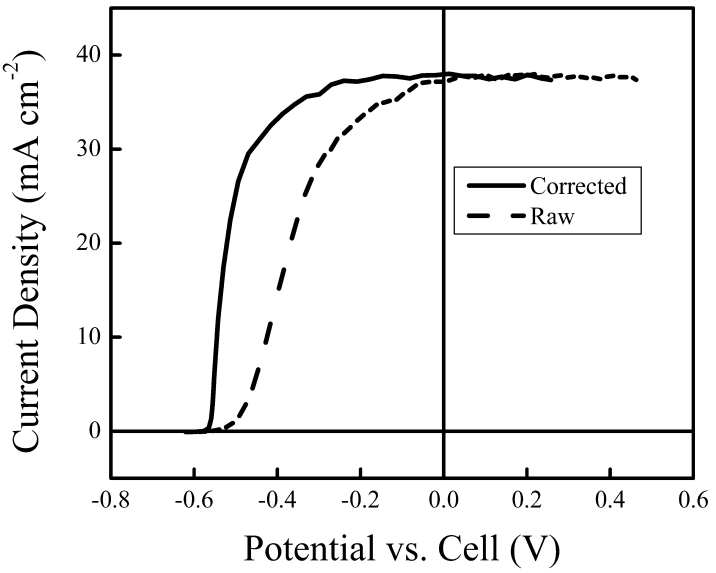

Figure 2.7. *Comparison between raw J-E data and data corrected for series resistance and concentration overpotentials under 100 mW cm^{-2} illumination.*

Figure 2.7 shows the *J-E* behavior after correction for series resistance and concentration overpotentials.[44] The planar electrodes had three-electrode (photoelectrode) energy conversion efficiencies of ~14% from incident energy into electrical energy, whereas the macroporous Si samples exhibited photoelectrode efficiencies of 10-12% (Table 2.2).

2.4.3 Cyclic Voltammetry of Planar and Macroporous Si Samples

When the peak current is limited by mass transport of redox species to the electrode surface, as opposed to being under light-limited conditions, the cyclic voltammetric behavior of photoelectrodes probes the morphology of the solid/liquid contact and provides a measure of the junction area accessible to photogenerated minority carriers. Cyclic voltammetric data as a function of scan rate were thus collected to evaluate the

photoactive junction area for the macroporous Si electrodes relative to those of the planar Si electrodes.

The planar Si(100) samples showed the expected linear relationship between the cyclic voltammetric peak anodic current density and the square root of the scan rate (Figure 2.8). In solutions similar to those used for the cyclic voltammetry experiments, the diffusion coefficient of Me_2Fc in methanol was measured at a Pt microelectrode to be 1.02 x 10^{-5} cm^2 s^{-1}. The planar Si samples thus generally exhibited slightly smaller peak currents than expected based on the concentration of Me_2Fc used and the measured diffusion coefficient of Me_2Fc in methanol, but behaved in general in accord with expectations.

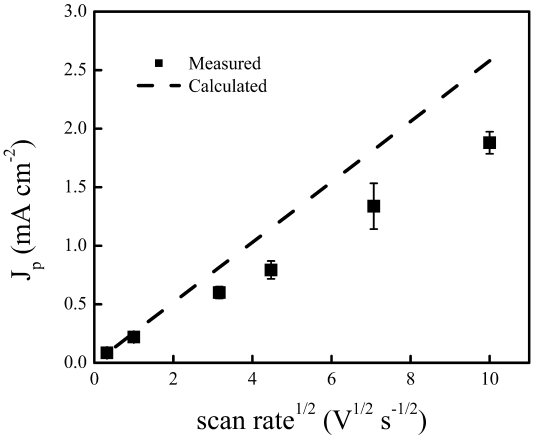

Figure 2.8. *Peak current density versus square root of the scan rate for planar (100)-oriented Si samples in methanol with 0.3 mM Me_2Fc and 1.0 M $LiClO_4$. The dashed line indicates the calculated peak current density for these samples based on the measured electrode area and diffusion coefficient of Me_2Fc, and is not a fit to the data. Error bars represent the standard error of the mean.*

The peak current data measured from the cyclic voltammetric behavior of macroporous Si electrodes, normalized to the projected area of the electrodes, are displayed in Figure 2.9. At fast scan rates, v, all of the porous electrode samples showed significantly higher projected-area-normalized peak current densities, $J_{p,proj}(v)$, than the mass-transport-limited current densities measured at, or expected theoretically for, planar Si electrodes. At any given high scan rate, $J_{p,proj}(v)$

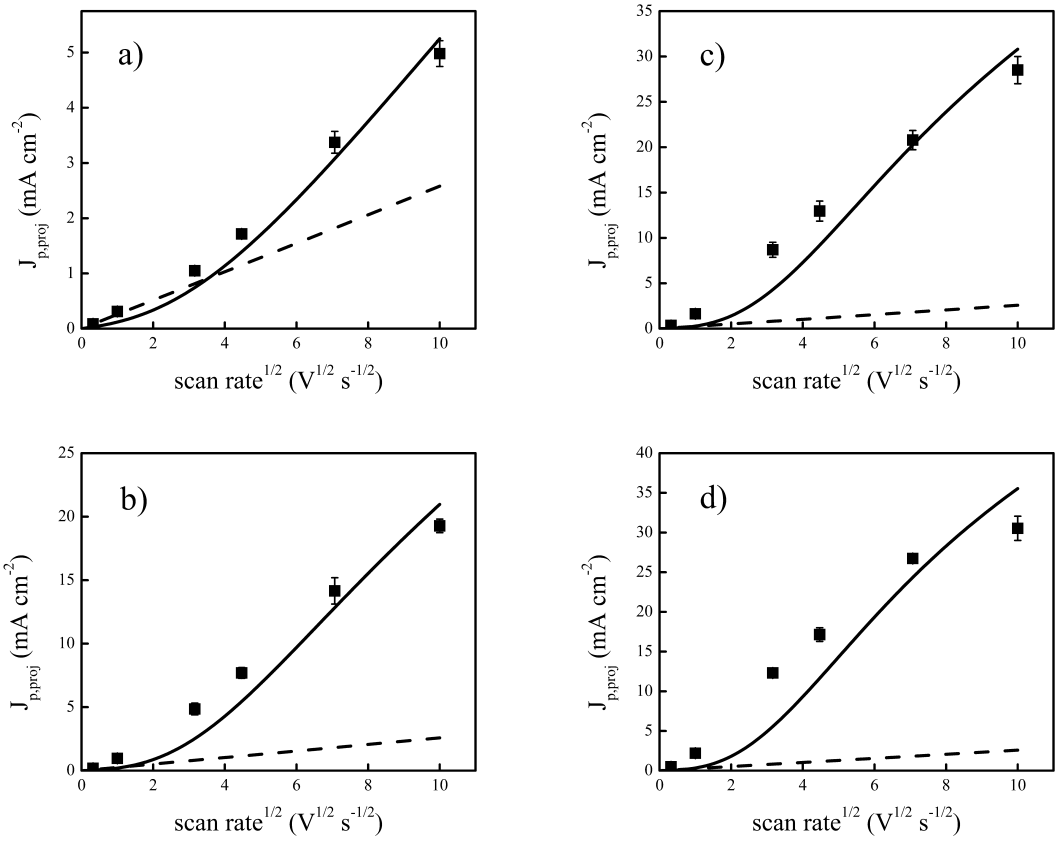

Figure 2.9. *Peak current density normalized to the projected area versus square root of the scan rate for macroporous Si electrodes produced by etching (100)-oriented Si samples for a) 15 min, b) 30 min, c) 45 min, and d) 60 min. The data were obtained in methanol with 0.3 mM Me_2Fc and 1.0 M $LiClO_4$. The solid lines indicate the fit to the data using the model of Neudeck and Dunsch and allowing the pore-pore spacing as the only adjustable parameter.[45] The dashed line indicates the calculated peak current density for these samples based on the measured electrode area and diffusion coefficient of Me_2Fc assuming a planar electrode, and are not a fit to the data. Error bars are the standard error of the mean.*

consistently increased with increasing pore length, as produced by an increase in etching time and as measured by SEM data. The pore morphology was largely unchanged with increasing etch time, while the pore length increased linearly, so the surface area and thus the values of $J_{p,proj}(v)$ are expected to increase with etching time, in accord with observations.

The normalized peak current data for the macroporous Si photoelectrodes were fitted using a theory that has been developed previously for the voltammetric behavior of microstructured metal electrodes that have a geometry very similar to that of the macroporous Si electrodes described herein.[45] The pore-pore spacing was allowed to vary while the pore diameter and pore length were fixed to the values measured from SEM images. The fit typically yielded values of the pore-pore spacing on the order of 2 μm, which is consistent with the SEM images of the porous samples. The analysis of the cyclic voltammetric data is thus consistent with a model in which photogenerated minority carriers can access the entire surface area of the solid/liquid junction on the macroporous Si photoelectrode samples studied herein.

2.5 Discussion

The *J-E* data under simulated AM 1.5 illumination suggest that the macroporous Si electrodes, despite their rough surface and high surface area, can provide high solar energy conversion efficiencies. The open-circuit voltage remained relatively large despite the increase in surface area by a factor of at least 15 for the macroporous samples relative to the planar samples, based on estimates from SEM images. Although these porous silicon samples were made from single crystalline silicon, they demonstrate that it is possible, in a geometry with a high surface area and an irregular surface, to retain good collection of charge carriers without significant surface-based recombination losses. Hence, it ought to be possible to use low diffusion length materials in efficient solar energy conversion devices, provided that the directions of charge-carrier generation and collection can be separated.

The V_{oc} values did, however, decrease measurably with increasing pore length. Specifically, planar (100)-oriented Si samples exhibited V_{oc} ~ 566 mV, while the macroporous Si samples with the longest pores exhibited V_{oc} ~ 485 mV under the same conditions. A fundamental factor that contributes to this decrease is that V_{oc} is expected to be smaller at electrodes that have a high junction area per unit of projected area, because a constant excitation carrier flux from a fixed intensity light source will produce a lower flux of photogenerated charge carriers through the larger accessible junction area. The cyclic voltammetry data clearly indicate that the junction area is electrically active and that minority carriers are capable of being transferred across the entire exposed surface area of all of the macroporous Si samples investigated herein. The steady-state charge-carrier concentrations at the junction set the positions of the quasi-Fermi levels, which in turn determine V_{oc}. A lower minority-carrier flux will thus produce a lower quasi-Fermi level splitting, and therefore a lower value of V_{oc}, at systems having a high junction area per unit of projected area.[39,47,48] The V_{oc} of 566 mV observed for the planar Si(100) electrode is close to the bulk recombination/generation limit for such samples. If the flux of photogenerated carriers is instead distributed uniformly over a much larger junction area, the bulk recombination/generation limit on V_{oc} will be reduced, as given by the diode equation:

$$V_{oc} = \frac{k_B T}{q} \ln\left(\frac{J_{sc}}{\gamma J_0}\right) \tag{2.20}$$

where J_0 is the saturation current density, J_{sc} is the short-circuit current per unit of projected device area, and γ is the actual junction area per unit of projected area of the

device. For the limit of a uniform minority carrier flux with $\gamma = 15$, characteristic of the macroporous Si samples with the longest pores studied herein, equation (2.20) implies that V_{oc} will be reduced by ~70 mV relative to the situation with $\gamma = 1$, in accord with the observed decrease from 566 mV to ~485 mV between the planar and macroporous Si samples investigated herein. The estimated value of γ assumes smooth pore sidewalls with no branching, and is therefore a lower limit on the actual junction area per unit of projected area. Surface recombination may also contribute somewhat to the observed decrease in V_{oc}, because increasing the junction area would also result in an increased rate of surface-derived recombination for the macroporous Si samples, which have a higher solid/liquid junction area per unit of projected area than a planar device. However, surface recombination at n-Si surfaces in contact with CH_3OH-$Me_2Fc^{+/0}$ is very low, on the order of 20 cm s^{-1}.[16] The porous surfaces contain exposed off-angle planes, but measurements of V_{oc} for (110)-oriented Si samples, performed herein, also yielded bulk recombination-limited photovoltages for the planar, (110)-oriented, n-Si surfaces. Hence, surface recombination is expected to provide a relatively small contributon to the 80 mV decrease in V_{oc} observed for the macroporous Si samples having the longest pores. A precise assessment of the exact value of the theoretically expected reduction in V_{oc} in the system of interest under white light excitation will require a detailed 2-dimensional description of the carrier generation and transport profiles in the macroporous Si samples of concern.

The decrease in V_{oc} with increasing junction area represents a fundamental limitation on micro- and nano-structured semiconductor devices for solar energy

conversion, and should be carefully considered in any new design scheme involving either nanoparticles, nanorods, interpenetrating networks, or other systems having a high junction area per unit of projected device area. This factor highlights the importance of selecting a device geometry that has short path lengths for minority carrier collection, while insuring that the microscopic junction area is as small as possible. Regardless, the high efficiencies observed in this study establish that it is indeed possible to efficiently convert light energy into electrical energy using highly structured materials.

2.6 References

1. Kayes, B. M.; Atwater, H. A.; Lewis, N. S. *J. Appl. Phys.* **2005**, *97*, 114302.
2. Anderman, M.; Kennedy, J. H. In *Semiconductor Electrodes*; Finklea, H. O., Ed.; Elsevier: New York, 1988, p 147-202.
3. Erné, B. H.; Vanmaekelbergh, D.; Kelly, J. J. *J. Electrochem. Soc.* **1996**, *143*, 305-314.
4. Erné, B. H.; Vanmaekelbergh, D.; Kelly, J. J. *Adv. Mater.* **1995**, *7*, 739-742.
5. van de Lagemaat, J.; Plakman, M.; Vanmaekelbergh, D.; Kelly, J. J. *Appl. Phys. Lett.* **1996**, *69*, 2246-2248.
6. Beermann, N.; Vayssieres, L.; Lindquist, S. E.; Hagfeldt, A. *J. Electrochem. Soc.* **2000**, *147*, 2456-2461.
7. Baxter, J. B.; Aydil, E. S. *Appl. Phys. Lett.* **2005**, *86*.
8. Takanezawa, K.; Hirota, K.; Wei, Q. S.; Tajima, K.; Hashimoto, K. *J. Phys. Chem. C* **2007**, *111*, 7218-7223.
9. Wei, Q. S.; Hirota, K.; Tajima, K.; Hashimoto, K. *Chem. Mat.* **2006**, *18*, 5080-5087.
10. Kang, Y. M.; Park, N. G.; Kim, D. *Appl. Phys. Lett.* **2005**, *86*, 113101.
11. Huynh, W. U.; Dittmer, J. J.; Alivisatos, A. P. *Science* **2002**, *295*, 2425-2427.
12. Law, M.; Greene, L. E.; Johnson, J. C.; Saykally, R.; Yang, P. D. *Nat. Mater.* **2005**, *4*, 455-459.
13. Law, M.; Greene, L. E.; Radenovic, A.; Kuykendall, T.; Liphardt, J.; Yang, P. D. *J. Phys. Chem. B* **2006**, *110*, 22652-22663.
14. Lehmann, V.; Föll, H. *J. Electrochem. Soc.* **1990**, *137*, 653-659.
15. Rosenbluth, M. L.; Lewis, N. S. *J. Am. Chem. Soc.* **1986**, *108*, 4689-4695.
16. Gstrein, F.; Michalak, D. J.; Royea, W. J.; Lewis, N. S. *J. Phys. Chem. B* **2002**, *106*, 2950-2961.
17. Lehmann, V. J. Electrochem. Soc. **1993**, 140, 2836-2843.
18. Ottow, S.; Lehmann, V.; Foll, H. *J. Electrochem. Soc.* **1996**, *143*, 385-390.

19. Föll, H.; Christophersen, M.; Carstensen, J.; Hasse, G. *Mater. Sci. Eng. R-Rep.* **2002**, *39*, 93-141.

20. Lehmann, V. *Thin Solid Films* **1995**, *255*, 1-4.

21. Chazalviel, J. N.; Wehrspohn, R. B.; Ozanam, F. *Mater. Sci. Eng. B-Solid State Mater. Adv. Technol.* **2000**, *69*, 1-10.

22. Ross, F. M.; Oskam, G.; Searson, P. C.; Macaulay, J. M.; Liddle, J. A. *Philos. Mag. A-Phys. Condens. Matter Struct. Defect Mech. Prop.* **1997**, *75*, 525-539.

23. Ottow, S.; Lehmann, V.; Foll, H. *Appl. Phys. A-Mater. Sci. Process.* **1996**, *63*, 153-159.

24. Shapley, J. D. L.; Barrow, D. A. *Thin Solid Films* **2001**, *388*, 134-137.

25. Sailor, M. J.; Lee, E. J. *Adv. Mater.* **1997**, *9*, 783-793.

26. Propst, E. K.; Rieger, M. M.; Vogt, K. W.; Kohl, P. A. *Appl. Phys. Lett.* **1994**, *64*, 1914-1916.

27. Doan, V. V.; Sailor, M. J. *Appl. Phys. Lett.* **1992**, *60*, 619-620.

28. Lehmann, V. Electrochemistry of Silicon: Instrumentation, Science, Materials and Applications; Wiley-VCH, 2002.

29. Parkhutik, V. Solid-State Electron. **1999**, 43, 1121-1141.

30. Zhang, X. G. J. Electrochem. Soc. **2004**, 151, C69-C80.

31. Searson, P. C.; Macaulay, J. M.; Ross, F. M. *J. Appl. Phys.* **1992**, *72*, 253-258.

32. Gibbons, J. F.; Cogan, G. W.; Gronet, C. M.; Lewis, N. S. *Appl. Phys. Lett.* **1984**, *45*, 1095-1097.

33. Forbes, M. D. E.; Lewis, N. S. *J. Am. Chem. Soc.* **1990**, *112*, 3682-3683.

34. Tan, M. X.; Laibinis, P. E.; Nguyen, S. T.; Kesselman, J. M.; Stanton, C. E.; Lewis, N. S. In *Progress In Inorganic Chemistry, Vol 41*; John Wiley & Sons Inc: New York, 1994; Vol. 41, p 21-144.

35. Lewis, N. S.; Rosenbluth, M. L. Photocatalysis: Fundamentals and Applications; Wiley Interscience: New York, 1989.

36. Rosenbluth, M. L.; Lieber, C. M.; Lewis, N. S. *Appl. Phys. Lett.* **1984**, *45*, 423-425.

37. Gronet, C. M.; Lewis, N. S.; Cogan, G. W.; Gibbons, J. F. *Proc. Natl. Acad. Sci.* **1983**, *80*, 1152-1156.

38. Rosenbluth, M. L.; Lewis, N. S. *J. Phys. Chem.* **1989**, *93*, 3735-3740.

39. Tan, M. X.; Kenyon, C. N.; Lewis, N. S. *J. Phys. Chem.* **1994**, *98*, 4959-4962.

40. Lewis, N. S. J. Electrochem. Soc. **1984**, 131, 2496-2503.

41. Lewis, N. S. Accounts Chem. Res. **1990**, 23, 176-183.

42. Pomykal, K. E.; Fajardo, A. M.; Lewis, N. S. *J. Phys. Chem.* **1996**, *100*, 3652-3664.

43. Lewis, N. S.; Gronet, C. M. *Appl. Phys. Lett.* **1983**, *43*, 115-117.

44. Fajardo, A. M.; Lewis, N. S. *J. Phys. Chem. B* **1997**, *101*, 11136-11151.

45. Neudeck, A.; Dunsch, L. *J. Electroanal. Chem.* **1994**, *370*, 17-32.

46. Hamann, T. W.; Gstrein, F.; Brunschwig, B. S.; Lewis, N. S. *J. Am. Chem. Soc.* **2005**, *127*, 7815-7824.

47. Kruger, O.; Kenyon, C. N.; Tan, M. X.; Lewis, N. S. *J. Phys. Chem. B* **1997**, *101*, 2840-2849.

48. Kenyon, C. N.; Tan, M. X.; Kruger, O.; Lewis, N. S. *J. Phys. Chem. B* **1997**, *101*, 2850-2860.

Chapter 3

Physical Model Systems of Wire Array Solar Cells: Low Minority Carrier Diffusion Length Materials and Reactive Ion Etched Pillars

3.1 Abstract

In order to understand the fundamental constraints of using structured materials to enable cost-effective solar energy devices, both macroporous silicon and reactive ion etched (RIE) silicon pillars have been used as photoelectrodes. Macroporous Si was doped with Au in order to systematically lower the minority carrier diffusion length for the purpose of mimicking devices made from structured low-cost materials. Control over the charge carrier lifetime was demonstrated, with lifetimes between 1 and 15 μs achievable by varying the Au drive-in temperature. Photoelectrochemical measurements in methanol with dimethylferrocene$^{+/0}$ showed significant decreases in both short circuit current density (J_{sc}) and open circuit voltage (V_{oc}) with increasing Au doping. Furthermore, at the highest Au concentrations tested, the porous samples outperformed the planar samples, demonstrating that structuring of the absorber can lead to improvements in charge carrier collection, as expected from computational models. Finally, in order to independently test the claim that the increased junction area per unit of projected area found in structured electrodes gives rise to a decrease in the V_{oc}, pillars were etched in high quality silicon by cryogenic RIE, and photoelectrochemical measurements were made.

3.2 Introduction

Chapter 2 presents a comparison of the performance of high quality crystalline silicon in structured (macroporous) form and planar form.[1] The results shown there demonstrate primarily that there is a small but significant impact of creating structured samples on the measured open circuit voltage (V_{oc}) under illumination. This chapter continues the exploration of physical model systems of silicon wire arrays by exploring two consequences of using structured materials as the absorber in energy conversion devices. These studies are motivated by theoretical work suggesting that significant efficiency gains can be expected by employing radial junctions in materials with diffusion lengths of about 1-10 μm.[2] Reactive ion etching has been used to produce pillars of high quality silicon,[3,4] which were designed to verify the reduction of V_{oc} with increased junction area per unit of projected area. Additional studies have also been pursued with macroporous silicon, including photolithographic templating of pores as a method for producing well-defined materials. Furthermore, doping with Au was pursued as a means to measure the performance of low-quality materials in both porous and planar structures.

3.2.1 Macroporous Silicon

The formation of porous silicon was originally discovered by Uhlir and Turner at Bell Labs in the 1950s, but its study was not popularized until the discovery of the photoluminescent properties of porous silicon.[5-8] Although many studies have explored the synthesis and applications of microporous silicon,[9-14] we are primarily concerned with macroporous silicon, which makes a better model of wire array solar cells due to the

highly vertical nature of the pores that are formed. Lehmann et al. originally reported that n-type silicon could be etched to produce long, straight-walled, uniform pores with micron-sized dimensions by etching in aqueous HF solutions under back-side illumination.[15-19] Although there are several theories about why pores form on n-type silicon surfaces under these conditions, it is widely believed that a hole-limited silicon dissolution reaction is primarily responsible for pore formation in n-type silicon.[10,15,18-24] In the presence of fluoride anions and holes, Si-H surface bonds can be converted to Si-F bonds with the release of H_2 (Figure 3.1).[10,23] The polarity of the Si-F bonds weakens the Si-Si bonds to the lattice, allowing HF to attack and release SiF_4 from the surface. SiF_4 is then quickly converted to SiF_6^{2-}, which is the reported product of dissolution.[10,18] In the presence of water, it is also postulated that oxidation of the Si-Si bond to the lattice may follow the initial Si-F bond formation and that subsequent dissolution of this oxide by HF may be responsible for the dissolution process (Figure 3.1).[23] For both of these

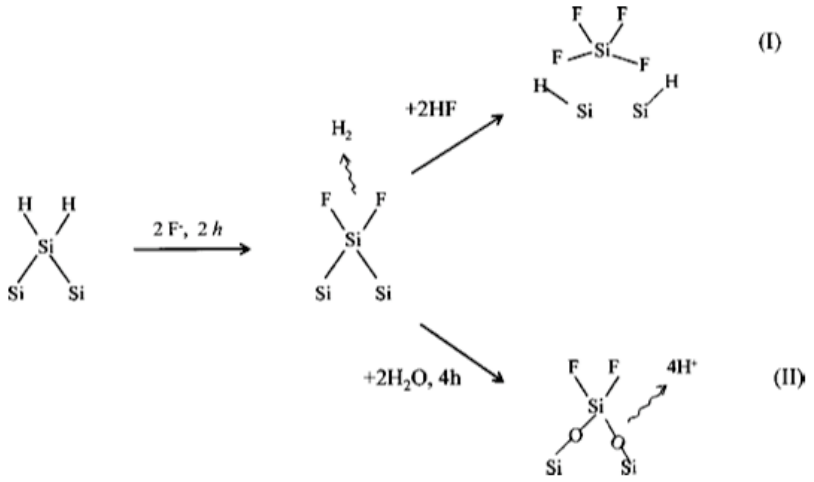

Figure 3.1. *Proposed mechanisms of Si dissolution under anodic conditions.[23] The initial step requires the presence of both holes and fluoride ions, and the subsequent step can proceed both in the absence (I) or presence (II) of water.*

mechanisms, it is necessary that both holes and fluoride ions be present at the interface for the initial step, and therefore the reaction rate will be limited in the absence of either.

Examining a typical *J-E* curve of p-type Si in HF reveals that the current increases with increasing anodic potential to a peak, commonly labeled as J_{ps} (Figure 3.2).[10,23] The *J-E* curves of n-type Si in HF are found to match those of p-type silicon, but the n-type Si are hole limited in the dark.[18,25] Therefore the current in n-type Si is limited by the hole supply provided by illumination, and the *J-E* curve reaches a plateau at the hole supply limit.[10,18] It is found that for all current densities below J_{ps}, porous silicon can form, but that at J_{ps}, electropolishing occurs.[10,23] Thus, J_{ps} is believed to be the point at which the hole supply is no longer limiting and the HF supply has become limiting.[10,22] In n-type silicon under back-side illumination, pore formation occurs by preferential collection of holes at the curved pore tips, where the electric field is the highest (Figure 3.3).[10,23,24] Pores formed on polished substrates first proceed through an initiation period where etch pits are formed, and some of these pits subsequently develop into pores.[18] However, by producing lithographically defined etch pits in the surface, the pore positions can be templated because the photogenerated holes will be preferentially harvested at the highly curved etch pit tips.[18]

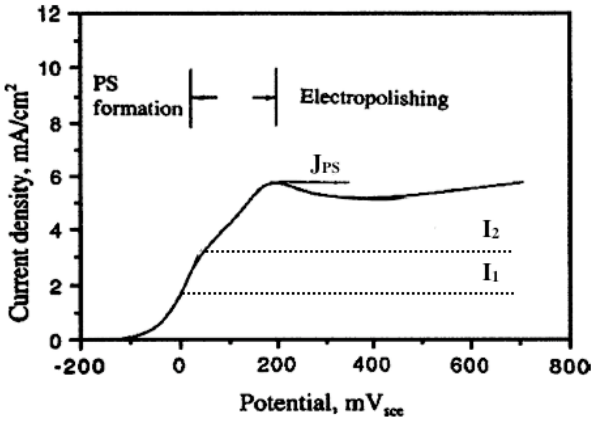

Figure 3.2. *Typical J-E curve for p-type Si in aqueous HF solution (Solid line).[23] J_{ps} indicates the onset of electropolishing. For n-type Si, the curves are limited by the light, and two cases are shown by dotted lines, with $I_2 > I_1$.*

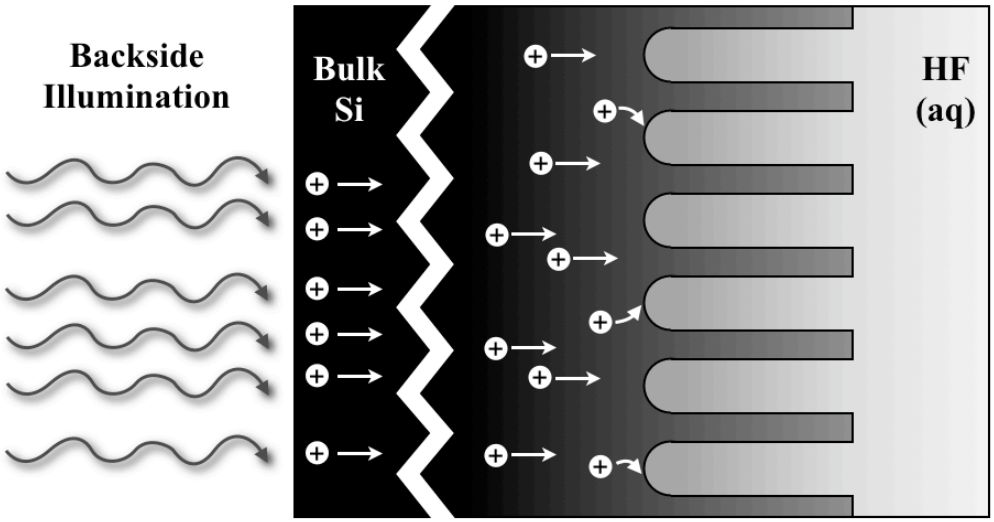

Figure 3.3. *Schematic of pore etching in n-type Si. Illumination incident from the back of the sample generates holes that subsequently diffuse through the bulk of the Si. At the Si/HF(aq) interface, the holes enable the dissolution of Si, and they are preferentially harvested at the curved pore tips.*

Under anodic etching conditions, there will be a significant space charge layer in n-type Si, and it has been proposed that the size of this space charge layer is roughly half of the pore-pore spacing.[18] If the pores were spaced farther apart, holes would be able to diffuse into the neutral region between pores and would then be collected at the pore side walls rather than at the pore tips, causing etching of the side walls. Thus, the pore spacing is expected to be twice the depletion width, given for n-type Si by:[26]

$$W = \sqrt{\frac{2\varepsilon_s \left(V_{bi} + V_{app}\right)}{qN_d}} \tag{3.1}$$

where W is the depletion width, ε_s is the static dielectric constant of silicon, q is the charge on an electron, N_d is the donor density, V_{bi} is the built-in voltage (band bending), and V_{app} is the applied voltage. Thus the pore-pore spacing will depend on $N_d^{-1/2}$ and $V_{app}^{1/2}$, but much greater variability in the dopant density is accessible (orders of magnitude) as compared to the accessible range of applied voltages. Therefore, the

primary mechanism of controlling pore spacing is to change the dopant density of the Si used. It has been found that when pores are templated by photolithography, if the pore spacing is too large (depletion region too small for the template), then the pores will branch to form pores with smaller spacing.[10,18] Similarly, joining of pores is observed when the templated pits are too close together. Since the pore spacing depends on the depletion width, it is important to match the doping of the samples used with the lithographic template to be employed.

It has also been found that the pore area is related to the current density, *J*, used for etching by:[15]

$$\rho = J/J_{ps} \tag{3.2}$$

where ρ is the porosity of the sample—the ratio of the total projected pore area to the total projected surface area. Thus, if the pore spacing is set by the dopant density, different porosities will generate different pore sizes with the unit cell dimensions remaining approximately constant.[10] The pore shape can also be controlled to some extent by changing the applied voltage (which will also change the depletion width), but round pores—which are obtained at relatively low voltages—are usually desired for their uniformity.[10,18] Finally, the pore length is controlled by the etching time without greatly affecting the pore diameter, shape, or pore-pore distance.[10] Thus, with anodic etching of n-type Si under back-side illumination, the pore size, pore-pore distance, pore shape, and pore length can all be controlled independently by varying the etching current (set by the illumination intensity), the sample doping, the applied voltage, and the etching time, respectively. Since these structures can be made from silicon of known quality and

materials properties, macroporous silicon is an ideal system for studying the effects of structure on device performance, keeping all other factors the same.

Both microporous silicon and macroporous silicon have found application in many areas. Microporous silicon has been studied extensively due to its luminescent properties and therefore its potential integration into optoelectronic systems.[7,11,12] Microporous silicon has also been used in conjunction with solar cells, but not as the absorbing medium. Instead, it has been explored as a potential antireflective coating[27,28] and as a method for layer transfer of thin-layer planar silicon solar cells.[29] The applications of macroporous silicon, which has a much smaller surface area/volume ratio, have been largely optical in nature. Etching all the way through a sample to produce long, narrow, and uniform channels enabled the production of optical short-pass filters with cutoffs in the near UV range.[30] Macroporous silicon has also been used as a photonic band-gap material—porous samples with straight pore walls have been used to produce 2D photonic band-gap materials,[31] and porous structures with controlled pore deletion defects have been used to produce waveguides.[32] More advanced etching techniques also allow the production of pores with widely varying diameter along the length of the pore, enabling the fabrication of cubic lattice materials that show 3D photonic band-gaps.[33-36]

For solar energy applications, most work on macroporous silicon has focused on its antireflective properties, and it has not typically been used as the absorber layer in solar energy conversion devices.[37-45] To the best of our knowledge, there is only one other report, aside from the work presented in Chapter 2,[1] in which macroporous silicon was used as the absorber layer in a solar energy conversion device.[46] In this work a solid state

junction was produced in macroporous n-type Si for the purpose of both photovoltaic and betavoltaic energy conversion. In this case p-type Si was used as the absorber layer, giving rise to much thinner pore walls than those produced in n-type Si, and the primary goal was to increase the diode junction area in order to increase the area for injection of beta particles.[46]

In addition to silicon, other semiconductors can be etched anodically to produce porous structures, including GaP.[47] The principle of improving the carrier collection properties of a material by decoupling the directions of light absorption and charge carrier collection was demonstrated in porous GaP as an increase in current following porous etching.[48,49] These studies show that carrier collection can be significantly increased by increasing the junction area in a collection-limited material having the right minority carrier diffusion length (~1-10 μm). The efforts reported in this chapter to controllably lower the minority carrier diffusion length of macroporous Si complement this work because the detailed effects of diffusion length on collection can only be ascertained in a semiconductor than can be made with very long diffusion lengths, such as Si.

3.2.2 Photoelectrochemistry of Silicon

Liquid junctions present a natural way to make conformal junctions to structured materials, and they have been used exclusively in this chapter to make contact to both macroporous silicon and silicon pillars produced by reactive ion etching. For n-Si in methanol, ideal behavior of the V_{oc} with changing barrier height has been demonstrated, and ferrocene and some of its derivatives (dimethyl- and acetyl-) are known to give bulk-limited values of V_{oc}.[50,51] Furthermore, studies of the surface recombination velocity

(SRV) of various silicon interfaces showed that the SRV for n-Si while in contact with ferrocene$^{+/0}$/methanol is on the order of 20 cm s^{-1}, which is comparable to or lower than the value found for Si in HF.[52] Both formation of an inversion layer at the surface and possible methoxylation of the surface in the presence of a one-electron oxidant are thought to be responsible for the low SRV values observed.[52,53]

Given the high barrier heights and low SRV values obtainable, the n-Si/methanol/ ferrocene$^{+/0}$ system is expected to produce excellent photoelectrochemical energy conversion devices. When using this system with ferrocene or its derivatives, over 10% energy conversion efficiency was found for single crystalline samples,[54-56] and efficiencies as high as 7.2% were achieved on polycrystalline Si.[57] Given these characteristics, the use of dimethylferrocene$^{+/0}$/methanol as the contacting phase when studying structured Si samples is a promising route to readily form high quality junctions. Much of the work presented in this chapter concerns the *J-E* curves of macroporous Si and reactive ion etched Si pillars in contact with this phase.

3.3 Experimental

3.3.1 Reagents

Methanol (BakerDry, Baker, Phillipsburg, NJ), sodium dodecylsulfate (SDS) (Sigma-Aldrich, St. Louis, MO), AZ-5214-E photoresist (Clariant, Somerville, NJ), AZ-300MIF developer (Clariant), 1,1,1,3,3,3-Hexamethyldisilazane (Sigma-Aldrich), potassium hydroxide (Mallinckrodt, Hazelwood, MO), 99.9+% gold wire (Aldrich), 49% (27 M) HF(aq) (Transene, Inc., Danvers, MA), and buffered HF(aq) (Transene) were used without further purification. Water (18 MΩ cm resistivity) was obtained from a

Barnstead Nanopure system. Lithium perchlorate, $LiClO_4$ (Sigma-Aldrich), was fused under vacuum and stored under an inert atmosphere until use. Dimethylferrocene (Me_2Fc, Sigma-Aldrich) was sublimed at ~45 ºC under vacuum and was stored under an inert atmosphere until use. Dimethylferrocenium tetrafluoroborate (Me_2FcBF_4) was synthesized from Me_2Fc by addition of excess HBF_4 in the presence of 0.5 equivalents of benzoquinone. The reaction was conducted under argon in an ice-water bath. The resulting solid was dried under vacuum and stored in an inert atmosphere. Me_2Fc and Me_2FcBF_4 were stored in light-protected bottles.

Silicon (Czochralski, n-type, (100)-oriented, P-doped) was obtained from either Virginia Semiconductor (Fredericksburg, VA, 1-10 Ω cm resistivity) or Wacker Siltronic (Munich, Germany, 4-8 Ω cm resistivity). These wafers were 500 ± 25 μm thick, polished on one side, and had measured resistivities between 5 and 7 Ω cm. Silicon (float zone, n-type, (111)-oriented, 4-8 kΩ cm resistivity, 350 ± 25 μm) was obtained from Topsil (Santa Clara, CA).

3.3.2 Photolithographic Patterning of Etch Pits

When lithographic etch pits were produced, a thermal oxide was first grown on n-type (100), 4-8 Ω-cm silicon. Silicon wafers were first rinsed with water, methanol, acetone, methanol, and then water and then dried under a stream of N_2 and transfered to a clean quartz slide. Samples were then oxidized in a tube furnace under wet air for 2.5 hours at 1000 ºC. Thermally oxidized samples were then cleaned with water, methanol, acetone, methanol, and water, and dried under a stream of N_2. 1,1,1,3,3,3-hexamethyldisilazane (HMDS) was then spin-coated onto the samples for 10 s at 3000

rpm. AZ-5214-E photoresist was then immediately spin-coated onto the samples for 30s at 4000 rpm. The photoresist was soft baked for 60 s at 105ºC on a temperature controlled hot plate, allowed to cool for 60 s, and exposed to the pattern for 30 s in a Karl Suss mask aligner. The pattern (3 μm holes in a dark background, spaced in a square array with 7 μm center-center distance) was chosen to be commensurate with the approximate pore size and spacing found when samples were etched without pre-patterning. Following exposure, the samples were developed for 30 s in undiluted AZ-300MIF developer, rinsed with water and dried. At this point, the patterned samples were subjected to a reversal step to harden the photoresist—the resist was exposed with no mask for 140 s, and then baked for 120 s at 120ºC.

Clear nail polish (Sally Hansen Hard as Nails, with Nylon) was applied to the back of the patterned samples to protect the oxide layer and allowed to cure for 30 min. The pattern was developed in the front oxide layer by etching 65-70 s in buffered HF, and the samples were rinsed with water. The patterned samples were subsequently etched in KOH (10% w/w) for 11-12 min at ~80ºC with vigorous stirring. During this step, both the photoresist and the clear nail polish were removed from the surface within the first few seconds of etching. The samples were rinsed with water and dried under a stream of N_2 and then examined under an optical microscope to verify the presence of fully developed pyramidal etch pits. Finally, the remaining oxide on both the front and back of the samples was removed by etching 60-70 s in buffered HF.

3.3.3 Fabrication of Macroporous Silicon

Macroporous silicon samples were produced both with and without lithographically defined etch pits. Etching of planar Si was performed in an aqueous solution of 5% HF(aq) that contained 10 mM SDS. The etching was performed potentiostatically at 5 V, with vigorous stirring, in a teflon cell equipped with a Pt counter/pseudoreference electrode. Prior to etching, the teflon cell, o-rings, and Pt mesh counter electrode were cleaned in aqua regia (3:1 HCl:HNO_3 by volume) for 30 min. Silicon samples were rinsed sequentially with water, methanol, acetone, methanol, and water, and were then dried under a stream of N_2(g). Approximately 2 cm^2 of the polished side of the Si was then exposed to the etching solution.

The illumination intensity was adjusted to maintain a constant 10 mA cm^{-2} of current during etching, with the light intensity controlled by connecting the lamp power supply to a variable resistor. Samples were etched for 15, 30, 45, or 60 min. The samples were then rinsed thoroughly in water and dried under a stream of N_2(g). To remove the microporous Si layer, the samples were etched in 10% KOH(aq) for 10-20 s, and were then rinsed sequentially with water, methanol, acetone, methanol, and water, followed by drying under a stream of N_2(g).

3.3.4 Doping of Planar and Macroporous Samples with Gold

Gold was introduced into both planar and macroporous samples in order to reduce the minority carrier lifetime in a controlled fashion. Gold was diffused into both float-zone, double-side polished (DSP), 4-8 kΩ-cm n-type (111) samples, having thickness 350 ± 25 μm and both planar and porous samples composed of Czochralski, single-side

polished (SSP), 4-8 Ω-cm n-type (100) silicon with thickness 525 ± 25 μm. The float-zone samples were used to calibrate the gold concentration in the samples (given by the diffusion temperature and the solubility limit of Au in Si at that temperature) with the observed minority carrier lifetime as determined by RF photoconductivity measurements.

SSP samples (planar or porous), were placed face down in a thermal evaporator and 5-20 nm Au was deposited onto the backside, as measured by a quartz crystal microbalance (QCM). For DSP samples, this procedure was performed twice to deposit Au on both polished surfaces of the sample. Following deposition, the Au was driven into the Si samples in a tube furnace at various temperatures under N_2 or 95%/5% N_2/H_2 (forming gas). Since the solubility limit of Au in Si at various temperatures is known,[58-60] the temperature of the tube furnace was used to set the Au doping level. The amount of time to allow to reach a relatively flat diffusion profile was calculated by solving the diffusion equation, Fick's Second Law:

$$\frac{\partial C(x,t)}{\partial t} = D\frac{\partial^2 C(x,t)}{\partial x^2} \tag{3.3}$$

where *C(x,t)* is the concentration of Au with position and time, and *D* is the diffusion coefficient of Au in Si. If we take the sample width to be *W*, then $x = 0$ is the front face of the sample, and $x = W$ is the back face. For samples with Au on both sides, the initial conditions were:

$$C(0,t) = C(W,t) = C_{max} \tag{3.4}$$

$$C(0 < x < W, 0) = 0 \tag{3.5}$$

where C_{max} indicates the solubility limit of Au in Si at the desired temperature. In the case of samples having Au on only one side, the boundary conditions employed were:

$$C(0,t) = C_{max} \tag{3.6}$$

$$C(x>0,0) = 0 \tag{3.7}$$

$$\left.\frac{\partial C(x,t)}{\partial x}\right|_{(W,t)} = 0 \tag{3.8}$$

The condition on the derivative of $C(x,t)$ ensures that there is no concentration gradient at the back face of the sample and therefore no diffusion of Au out of the back face, which is the expected condition when Au is present on only the front face.

By numerically solving the diffusion equation as described above for a series of time points, the time at which the total variation in concentration across the sample width was less than 5% could be calculated. This was taken to be the minimum necessary time at the target temperature in order to guarantee a uniform concentration of Au. Typically samples were held at the target temperature for 2-3 times longer than the calculated time to ensure a consistent diffusion profile. Table 3.1 lists values of C_{max} and D for Au in Si as well as the calculated times for one- or two-sided diffusion for the two widths of interest in these studies (350 μm for DSP, float-zone wafers, and 500 μm for SSP planar or porous Czochralski wafers).

Following deposition and drive-in of Au, the excess Au was removed by a variety of procedures. In a typical treatment, the samples were first etched 10 s in 49% HF to remove any surface oxide that might have formed during drive-in. They were subsequently treated for 30 min in aqua regia (3:1 concentrated HCl:concentrated HNO_3)

Table 3.1 *- Maximum solubility and diffusion coefficients of Au in Si.[58-60] Times shown are calculated by solving the diffusion equation.*

			Two-Sided		One-Sided	
T **(ºC)**	C_{max} **(cm^{-3})**	***D*** **($cm^2\ s^{-1}$)**	**350 µm Time (h)**	**500 µm Time (h)**	**350 µm Time (h)**	**500 µm Time (h)**
1100	6.3×10^{16}	1.3×10^{-6}	0.11	0.19	0.36	0.72
1000	1.0×10^{16}	6.1×10^{-7}	0.19	0.39	0.75	1.50
900	1.8×10^{15}	2.6×10^{-7}	0.44	0.92	1.78	3.58
800	5.0×10^{14}	9.0×10^{-8}	1.25	2.53	4.97	10.11
700	1.0×10^{14}	2.6×10^{-8}	4.36	8.86	17.39	35.47
600	2.0×10^{13}	5.5×10^{-9}	20.22	41.28	80.86	165.03

to remove the outer layer of Au. The samples were subsequently oxidized in piranha solution (3:1 conc. H_2SO_4:30% H_2O_2), etched in 49% HF to remove the oxide formed, and soaked again for 30 min in aqua regia to further remove Au from the surface. Samples were finally etched one more time in 49% HF prior to photoconductivity measurements or electrode fabrication.

3.3.5 RF Photoconductivity Measurements

Radio-frequency (RF) photoconductivity decay measurements are a contactless way to measure the minority carrier lifetime in a semiconductor sample. In the basic operation of the RF photoconductivity instrument a sample of Si is used as a resonant element in an RF circuit driven by a high-frequency signal generator. A 10 ns pulse of light from an Nd:YAG (1064 nm) laser induces an increase in the number of charge carriers and thus an increase in the conductivity of the Si, and the decay back to steady state is measured after the pulse. A detailed description of the instrument and its

components is available in the literature.[52] In order to mitigate contributions from surface recombination, all samples were measured with a thin layer of HF on both faces of the sample. The HF/Si interface is known to have a low surface recombination,[52] so the bulk lifetime can be measured in this way.

Some processes involved degreasing float-zone samples in order to remove an organic contaminants prior to measurement in the RF photoconductivity system. In this case, DSP samples were degreased by sonication for 5 min each in water, methanol, acetone, 1,1,1-trichloroethane, dichloromethane, 1,1,1-trichloroethane, acetone, methanol, and water, with a rinse in the next solvent in between each sonication step. They were subsequently etched in hot piranha (in a boiling water bath) for at least 60 min.

3.3.6 Production of Si Pillars by RIE

Reactive ion etching (RIE) was used to produce silicon pillar arrays from n-type <100> Si with a resistivity of 1-10 Ω-cm. The arrays consisted of 5, 10, 20, and 50 μm diameter spots in a hexagonal pattern with the spot to spot separation (edge to edge) equal to the spot diameter in each array. Each of the arrays was patterned over an area of about 2 x 2 mm^2, with multiple areas of each size of array patterned simultaneously on one sample. The hexagonal pillar arrays were photolithographically defined by using AZ-5214-E as an etch mask. Following exposure and development of the photoresist, the silicon sample was mounted on a carrier silicon wafer using a thin film of Fomblin oil (Solvay-Solexis, Thorofare, NJ). The Fomblin oil was found to make excellent thermal contact to the silicon carrier wafer. Prior to RIE, the chamber was cleaned with a high

pressure SF_6 plasma and then conditioned for 30 minutes under the etching conditions with a blank wafer. The RIE was then carried out cryogenically in an Oxford Instruments PlasmaLab System100 ICP-RIE 380. Typical conditions for etching are shown in Table 3.2. For the samples shown here, the etching was carried out in two steps of ~35 minutes each. Between the two etching steps, the samples were removed and blown with a stream of N_2 to remove any residual SF_6 that had accumulated near the base of the pillars. This was found to be an effective way to extend the growth of the pillars to longer dimensions.

Following reactive ion etching, the samples were treated for 60 min in piranha (3:1 conc. H_2SO_4:30% H_2O_2) to remove the thermal paste and etched in buffered HF for 4 min. The samples were then oxidized in a tube furnace under wet air at 850ºC for 90 min, etched in buffered HF 3 min and dried under a stream of N_2. Finally, the samples were annealed at 400ºC in the tube furnace under 95%:5% N_2:H_2 (forming gas).

Table 3.2 *- Reactive ion etching parameters used for typical samples.*

SF_6	O_2	He	ICP	RIE	Temp	Pressure
70 sccm	6 sccm	10 Torr	900 watts	5 watts	-140 ºC	10 mTorr

3.3.7 Scanning Electron Microscopy

Scanning electron microscopy (SEM) data were obtained using a LEO 1550 VP Field Emission SEM (FE SEM) using the in-lens detector at an accelerating voltage of 10 kV. Samples were scored on the back and cracked along the (100) directions to obtain cross sectional images, and the resulting pieces were mounted to the SEM stub using carbon or copper tape.

3.3.8 Preparation of Photoelectrodes

For photoelectrochemistry, the samples were scored and cracked to produce ~5 mm x 5 mm electrodes. The samples were then etched for 10-30 s in buffered HF(aq), rinsed with water, and dried under a stream of N_2(g). Ga/In eutectic was then immediately scratched into the back side of the samples. Ag paint was then used to affix the back of each sample to a coil of tinned Cu wire. In the case of macroporous silicon electrodes, the front surface of the samples was covered with Epoxies, Etc. (Cranston, RI) 20-3004 LV epoxy to leave an exposed area of ~1-2 mm^2. The silicon sample and the Cu wire were then sealed in a glass tube using Hysol 1C epoxy (Loctite, Rocky Hill, CT), with the sample surface oriented perpendicular to the long axis of the glass tube. When the LV epoxy was applied, most of it was covered with Hysol epoxy. The LV epoxy was needed due to the tendency of the Hysol epoxy to form bubbles on the porous Si surface. Both epoxies are opaque and resistant to methanol, and the Hysol epoxy provided strong structural support. Before use in photoelectrochemical experiments, electrodes were allowed to cure for at least 24 h at room temperature. For RIE pillar array samples, the same procedure as above was followed, except that LV epoxy was not use. The projected area of each electrode was measured by taking an image at 800 dpi of the electrodes and a 1 cm x 1 cm calibration square, using a flat-bed scanner, and analyzing the resulting image using the Image SXM software.

3.3.9 Photoelectrochemistry

Photoelectrochemical experiments were conducted in a sealed glass cell under a positive pressure of Ar. The standard measurement solution (CH_3OH, 1 M $LiClO_4$, 200

mM Me_2Fc, ~0.1 mM Me_2FcBF_4) was prepared and introduced into the measurement cell under an inert atmosphere. Silicon electrodes were etched (10-30 s in buffered HF(aq) for planar or RIE-etched pillar samples; 2 min in 1:1 (v:v) 27 M HF(aq):ethanol for porous samples) to remove the native oxide, rinsed with water, and then thoroughly dried under a stream of N_2(g). The electrodes were then immediately introduced into the cell (Figure 3.4), under a positive flow of Ar. The reference electrode was a Luggin capillary, with an outer tip diameter of ~ 100 μm, that contained a Pt wire and a sample of the same solution as in the working electrode compartment. A Pt mesh was used as a counter electrode. The cell had a flat quartz bottom, and the working and reference electrodes were positioned as close as possible to the bottom of the cell, with the tip of the Luggin capillary directly underneath the Si surface and as close as possible to the Si without touching its surface. The solution was stirred vigorously during all data collection.

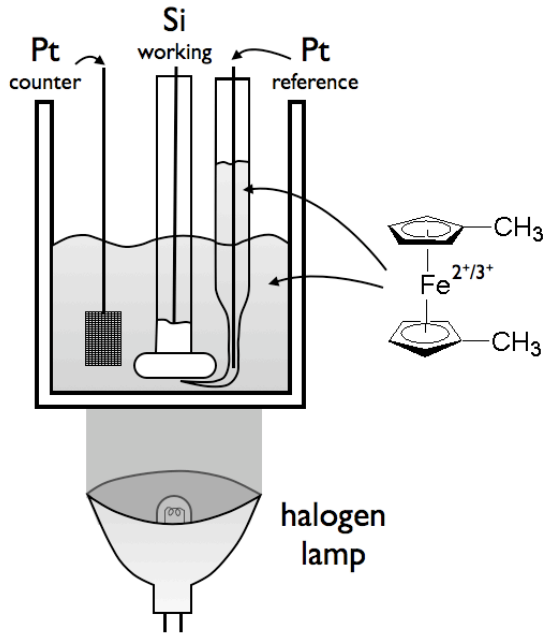

Figure 3.4. *Schematic diagram of the cell used. The filling solution is 1 M $LiClO_4$, 200 mM Me_2Fc, and ~0.1 mM Me_2FcBF_4 in methanol.*

Illumination of the bottom of the cell was provided by a 300 W ELH-type W-halogen bulb equipped with a dichroic rear reflector.[61] The illumination intensity was measured using a calibrated Si photodiode that was in turn calibrated relative to a

secondary standard Si solar cell. The secondary standard Si solar cell had been calibrated by an independent calibration laboratory with respect to a reference AM 1.5 spectrum at 100 mW cm^{-2} of illumination intensity. For Si photoelectrodes in this same cell configuration and electrolyte/redox system, this calibration method has been shown previously to produce short-circuit photocurrent densities that are very close to those obtained under the same intensity of actual sunlight.[54,55]

All current density-potential (*J-E*) measurements were recorded using a Solartron model 1287 potentiostat. In a typical experiment, the *J-E* behavior of the electrode was measured at 10 mV s^{-1} in the dark, then under 100 mW cm^{-2} of illumination, and then measured again in the dark. The open-circuit voltage, V_{oc}, was measured between each *J* versus *E* measurement. The short-circuit current density, J_{sc}, was calculated as the average current density for potentials within 10^{-4} V of 0 V versus the Nernstian potential of the cell. The values of V_{oc} and the presented *J-E* behavior are reported with respect to the Nernstian cell potential, which was measured with respect to the reference electrode for each working electrode. The Nernstian potential was typically 10-30 mV versus. the reference electrode potential, due to drift in the composition of the cell solution compared to the composition of the solution in the Luggin capillary. The point of maximum power was calculated as the average of 10 data points, after eliminating the 10 largest measured points (to remove any erroneous spikes). The efficiency and fill factor were calculated by conventional methods.

3.3.10 Correction for Series Resistance

To correct curves for a series resistance, equation (3.9) was employed:

$$E_{corr} = E_{meas} - iR_s \tag{3.9}$$

where E_{corr} is the corrected potential, E_{meas} is the measured potential, i is the signed current, and R_s is the series resistance. The potential was corrected at each point based on the absolute current and plotted as J vs. E as usual.

3.4 Results and Discussion

3.4.1 Photolithographic Pore Definition

In many studies of macroporous n-type silicon, photolithography and etch pit definition was used to produce ordered arrays of pores rather than the randomly arranged pores shown in Chapter 2.[10,15,18,19,33] In order to template pore growth, n-type, (100) Si

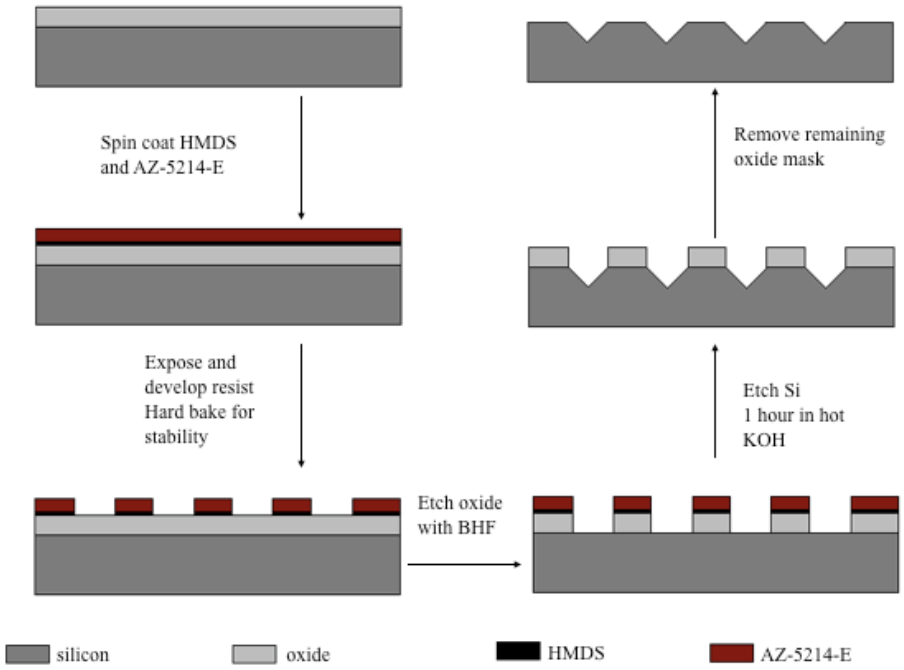

Figure 3.5. *Schematic of etch pit preparation. The photoresist mask is used to etch the oxide layer, and the oxide layer is used to etch the silicon pits.*

was first patterned with an array of pyramidal etch pits. It is expected that pyramidal etch pits will act as seed points for the growth of macropores due to the high electric field at the tips of the pyramids.[10] Thus, a higher degree of control over the structure of the porous samples is attainable through photolithographic templating.

A schematic illustration of the patterning procedure is shown in Figure 3.5. Photolithography is used to define openings in the SiO_2 layer, after which the SiO_2 layer serves as a mask for the KOH etching step. Both SiO_2 and Si_3N_4 serve as effective etch masks for KOH, allowing the definition of pits, but SiO_2 was chosen due to the ease of growing a thermal oxide layer on unmodified Si wafers. As shown in Figure 3.6, pyramidal pits are formed on the (100) surface after KOH etching. The formation of pyramidal pits is expected due to the enhanced stability of the (111) plane to KOH etching compared to the other low index planes of Si. Starting with a (100)-oriented wafer and assuming the etch planes are (111) planes, then we expect to see an angle of about 55º, and we observe an angle of about 52º. The slight deviation from the expected

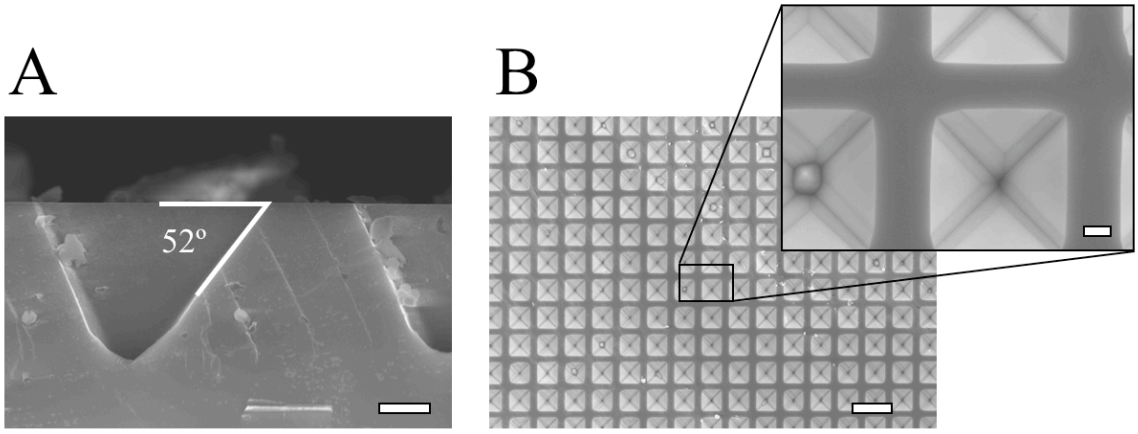

Figure 3.6. *SEM images of etch pits. A) Cross section showing the angle between the (100) surface and the pit side wall, which should be a (111) plane. Scale bar, 1 µm. B) Plan view showing the pyramidal nature of the etch pits. Scale bar, 10 µm. The inset is a higher-resolution image of the indicated area. Scale bar, 1 µm.*

value, as well as the asymmetry observed in the cross section may be due to slightly off-axis cleaving of the wafer prior to SEM.

When patterned samples were anodized in HF in the presence of surfactant, it was found that pore growth was initiated from the etch pits, as expected (Figure 3.7). The pores are wide near the surface of the sample and show a smooth transition from the surface etch pits into the pores. However, there is significant branching observed in the pore side walls, which indicates a mismatch between the pattern dimensions and the natural pore size and spacing given by the etching conditions employed.[10,18] It has been shown previously that the pore spacing is primarily influenced by the dopant concentration in the sample, and that pore branching is observed when the doping of the sample is too high for the pattern employed. [10,18]

The mismatch between the pattern used and the sample doping was unexpected because the pattern was designed based on the previous etching behavior of the silicon used. The mask used to generate the etch pit pattern consisted of 3 μm pores in a square

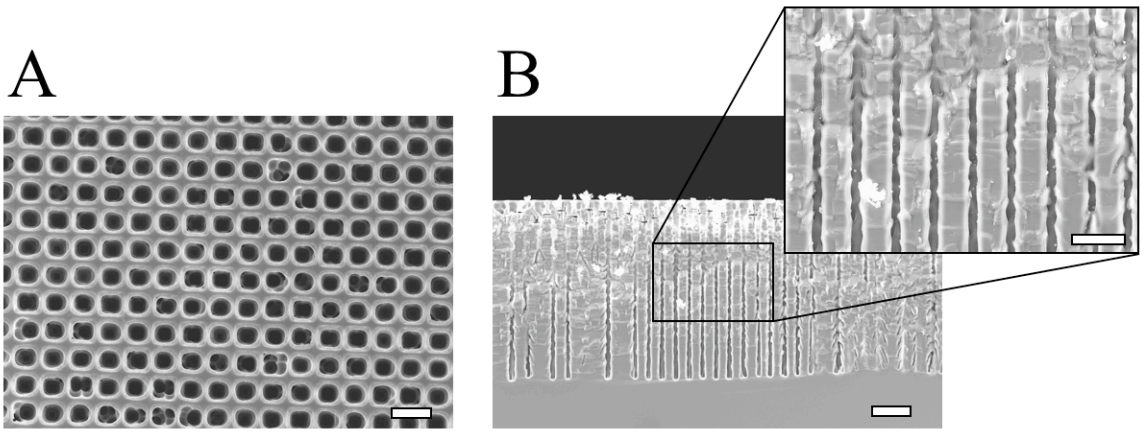

Figure 3.7. *SEM images of photolithographically templated pores. A) Plan view showing the visible pore branching and the wide pore mouths. Scale bar, 10 μm. B) Cross section showing pores etched for 60 minutes. Scale bar, 20 μm. The inset shows the pore branching in the cross section. Scale bar, 10 μm.*

array, with 7 μm center-to-center distance. These values were chosen after a careful examination of the growth tendencies of randomly seeded macropores (e.g., the porous samples considered in Chapter 2). By counting the number of pores in a given area of the sample, the unit cell for each pore was determined to be about 49 μm^2 in area, giving a square unit cell 7 μm to a side. Furthermore, the average pore diameter was found to be 3 μm in randomly initiated pores. Thus, the pattern used was expected to be appropriate for the doping level and etching conditions employed, but significant branching was still observed.

Although the templated macropores produced here do not show the uniformity and fidelity of those shown in the literature, they do demonstrate pore initiation from patterned etch pits. Further optimization of the mask used or the dopant concentration of the Si employed would produce samples consistent with those that have been shown in the past. However, given the care that must be taken in matching the mask to the dopant concentration, further studies conducted on macroporous silicon were carried out using randomly initiated pores. The possibility for radial charge carrier collection, which is the key property of macroporous Si being explored in this work, should be available in an average sense in randomly initiated pores. In fact, a square array of pores leads to more large contiguous areas of Si that might actually increase the average distance minority carriers must travel before being collected relative to a random arrangement of pores. Thus, all other results involving macroporous silicon, both in this chapter and in Chapter 2, refer to macroporous Si with randomly initiated pores.

3.4.2 Gold Doping of Macroporous Silicon

In order to demonstrate the principle that structured materials enable the orthogonalization of light absorption and charge carrier collection, macroporous silicon samples and planar silicon samples were doped with Au and the resulting low lifetime materials were tested to ascertain their photoelectrochemical properties. In the course of trying to produce materials with well-defined minority carrier lifetimes, however, there were significant challenges in material preparation. Both the challenges faced and the initial photoelectrochemistry results will be presented below.

3.4.2.1 Bulk Lifetime of Pure Samples

In order to demonstrate the controlled reduction of the sample lifetime by introduction of Au dopants into the Si lattice, samples consisting of double-side polished (DSP) float-zone Si were used. With high-purity float-zone Si, extremely long bulk minority carrier lifetimes are expected, typically on the order of 1 ms or greater.[52] Starting with (111)-oriented, n-type 4-8 kΩ-cm Si, lifetimes of about 1 ms were consistently measured when both faces of the sample were immersed in HF, which is known to create a low surface recombination velocity (SRV) interface with Si.[52] In n-type Si, the hole diffusion coefficient, D_p, is about 10 $cm^2\ s^{-1}$.[62] Therefore, we calculate the minority carrier diffusion length from[62]

$$L_p = \sqrt{D_p \tau} \tag{3.10}$$

This gives a minority carrier diffusion length of approximately 1.4 mm. This implies that minority carriers can traverse the width of the sample several times over before recombining, thus further confirming the low SRV of the HF-Si contact. This

measurement does not eliminate the possibility that the observed value is still limited by surface recombination, but in either case, the measured lifetime gives a lower bound on the bulk lifetime of the starting material used.

In order to demonstrate that the reduction in lifetime observed after Au doping (see below) is due to the presence of deep-level trap states introduced by Au, pristine Si wafers from the same stock that gave 1 ms minority carrier lifetimes were subjected to the conditions of the Au drive-in step, but in the absence of any Au. This consisted mainly of heating the samples in a tube furnace at various temperatures under ultra high-purity Ar or forming gas (95%:5% N_2:H_2). Heating degreased Si samples under inert gas caused a dramatic decrease in the measured lifetime. After heating at 700ºC for 4.5 hours, the minority carrier lifetime was measured to be about 15 μs, corresponding to a minority carrier diffusion length of about 170 μm. After heating at 1000ºC for less than an hour, the measured lifetime was only 10 μs. The reduction in lifetime was found to be independent of the surface treatment of the samples either before or after the heating step.

It should be possible to thermally treat Si in this way without significantly impacting the minority carrier diffusion length of the material. Thus, there must be an impurity that is introduced during the treatment. Careful degreasing of the wafers by sonication in series of organic and aqueous solvents, coupled with cleaning in piranha solution, should remove any surface contaminants prior to placing the samples in the tube furnace, but presence of such contaminants cannot be ruled out without further characterization. It is also possible that contaminants have been introduced to the samples from either the quartz tube (which is only used for pure Si, never with Au

contaminated samples) or from the gas delivery system itself. Any impurities introduced into the Si lattice during heating under an inert atmosphere are not likely due to the inert gas supply because different inert atmospheres produced the same drop in diffusion length.

This reduction in lifetime in the absence of the intentional introduction of impurities severely limits our ability to controllably produce Si samples having lifetimes between 10 μs and 1 ms. However, this does not preclude the possibility of studying the effects of Au impurity concentration on the photoelectrochemical properties of planar and porous samples. Even with a lifetime of 10 μs, the the minority carrier diffusion length is expected to be on the order 140 μm, which is enough that even the planar samples should retain most of their photoactivity. For porous samples, the pore-pore spacing is on the order of 5 μm, so diffusion lengths of 140 μm should give nearly 100% quantum yield.

3.4.2.2 Bulk Lifetime After Gold Doping

By controllably introducing Au into the Si samples, the lifetime could be lowered from the value measured after only heating the samples. A schematic of the diffusion process is shown in Figure 3.8. It has been shown previously that the equilibrium solubility of Au in Si is strongly dependent on temperature.[58,60] Therefore, by depositing Au on the Si surface at low temperature and driving it in at high temperature, the bulk concentration of Au should be set at the solubility limit of the drive-in temperature. After drive-in, any remaining Au film was removed from the Si surface. Furthermore, the near-surface region is expected to have a higher concentration of Au due accumulation of excess Au at surface defect sites. For that reason, after an initial treatment in aqua regia

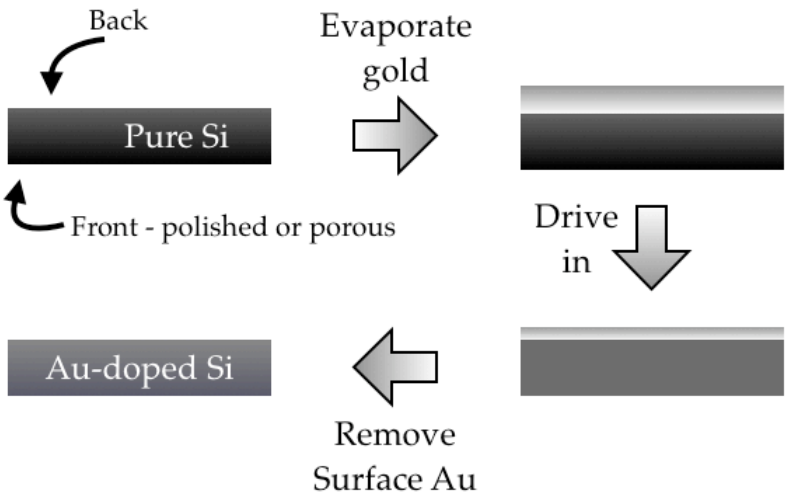

Figure 3.8. *Schematic of Au doping process. Au is evaporated on one or both sides, (one side shown), then driven in at elevated temperatures. Subsequent removal of the Au film leaves the doped substrate.*

to remove the film of excess Au, the samples were oxidized briefly in piranha solution and the resulting oxide layer removed in HF. Finally, any exposed surface Au was removed in aqua regia again. Since the bulk lifetime was measured by the contactless RF photoconductivity decay method, it was important to produce clean interfaces that could be well passivated in HF. As above, the observed lifetimes give a lower bound on the bulk lifetime and surface recombination.

Float-zone Si samples with Au diffused from both sides were used to calibrate the dependence of the bulk minority carrier lifetime on the expected Au concentration based on the drive-in temperature. As shown in Table 3.3, there was a significant effect of the drive-in temperature on the measured lifetime. The expected solubility limits at each temperature are also given in the table as C_{max}. However, as described in Section 5.2.1, the expected lifetime at a Au concentration of 10^{16} cm^{-3} is much smaller than the measured lifetime. Thus, it is expected that the actual Au concentration in the samples was significantly lower than the solubility limit.

Table 3.3. *Lifetime values measured by RF photoconductivity decay and the corresponding calculated values of the diffusion length at each temperature for Au drive in. The drive-in time was calculated as described in the Experimental Section.*

Temperature (°C)	C_{max} (cm^{-3})	τ (μs)	L_p (μm)
1000	6.3×10^{16}	1.3	51
900	1.0×10^{16}	1.4	53
800	1.8×10^{15}	6.7	120
600	5.0×10^{14}	15	170
1000 (No Au)	-	10	140
No bake, No Au	-	1000	1400

It is evident from Table 3.3 that controlling the temperature of the drive-in step affords some control over the lifetime, and therefore the minority carrier diffusion length, in these DSP float-zone samples. However, even at the highest temperature used, the minority carrier diffusion length is still an order of magnitude larger than the approximate pore-pore spacing found in randomly templated macroporous Si. Thus, little decrease in the photoelectrochemical performance of porous silicon samples is expected, even with the highest concentrations of Au explored. For planar Si, the penetration depth of white light exceeds 100 μm, so a significant reduction in current is expected for planar samples with the highest concentrations of Au.

3.4.2.3 Photoelectrochemical Measurements of Gold Doped Samples

Photoelectrochemical measurements were carried out on planar and macroporous samples derived from Czochralski-grown (100) n-type Si with a resistivity of 4-8 Ω-cm. The macroporous samples were etched for 60 min to produce pores with a length of approximately 85 μm (see Chapter 2).[1] For the porous samples, it was found that the

porous structure had to be produced first before the Au diffusion step—when anodizing Au-doped samples, the light intensity needed to produce the desired current was not achievable with the typical pore etching setup. Since the mechanism of pore etching on n-type Si is proposed to be due to a hole-limited reaction at the pore tips,[10,18] the inability to pass enough current through Au-doped samples during etching further corroborates the lowering of the minority carrier diffusion length by Au doping, implying recombination of photogenerated holes in the bulk. Since the pores could not be etched after Au doping, the drive-in step was carried out in a one-sided fashion from the back of porous samples. Au is only evaporated onto the back of the sample to avoid contamination of the highly structured front surface. The drive-in time was corrected appropriately for the one-sided diffusion process.

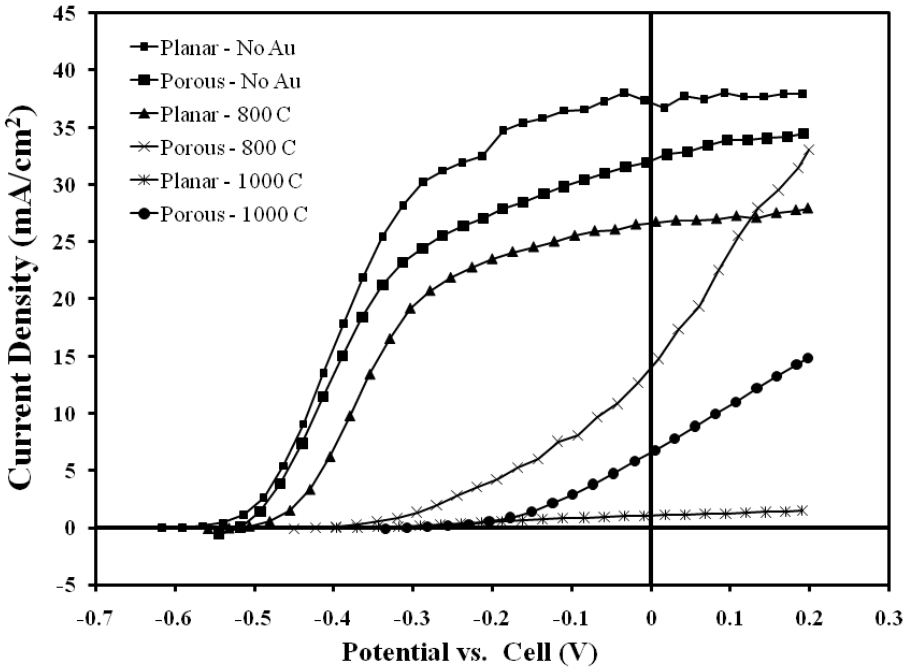

Figure 3.9. *J-E curves for porous and planar samples with various levels of gold doping. The curves were taken in the cell as described in the Experimental Section. All curves were collected under simulated AM 1.5 illumination, and the Au drive-in temperature is indicated. Samples designated as "No Au" were never in contact with Au and were not heated. These curves are representative for each type of sample.*

Representative *J-E* curves obtained under AM 1.5 illumination with both planar and porous Au-doped samples are shown in Figure 3.9. Samples were produced at two different drive in temperatures—800ºC and 1000ºC. It is apparent from the figure that the planar sample with drive in at 800ºC still shows good performance. The planar samples are expected to perform well at this Au concentration due to the long minority carrier diffusion lengths, as calculated above (~120 μm). The macroporous Si samples, however, show significant degradation even at the low concentration of Au. In particular, there seems to be a significant shunt or a very high resistance present. It is possible that the behavior observed is due to a high resistance at the back contact of the sample and not to poor performance in the porous sample. It is also possible that Au accumulates at defect sites on the porous front surface, and that these defect sites are not efficiently etched by the Au removal procedure.

Both the macroporous and planar samples show decreased performance when the Au drive-in temperature is increased to 1000ºC, particularly in the fill factor. A summary of the relevant solar cell figures of merit is given in Table 3.4. In particular, we note that,

Table 3.4. *Figures of merit for Au-doped Si electrodes. Temperatures indicated in the Sample Type column are the drive-in temperatures. Data are the mean of three electrodes (six for Au-free electrodes) and errors are the standard error of the mean.*

Sample Type	J_{sc} (mA cm^{-2})	V_{oc} (mV)	Fill Factor (%)	Efficiency (%)
Planar	36.2 ± 2.6	566 ± 2	44.6 ± 1.6	9.1 ± 0.5
Porous	31.5 ± 1.8	485 ± 12	41.3 ± 0.8	6.3 ± 0.5
Planar 800ºC	26.0 ± 0.8	517 ± 1	44.0 ± 0.9	5.9 ± 0.1
Porous 800ºC	10.4 ± 2.1	380 ± 0.1	22.5 ± 1.7	0.9 ± 0.2
Planar 1000ºC	1.9 ± 1.1	362 ± 10	29.0 ± 7.4	0.1 ± 0.1
Porous 1000ºC	7.2 ± 0.3	291 ± 14	18.7 ± 1.0	0.4 ± 0.1

after driving Au in at 1000ºC, the macroporous samples show significantly higher J_{sc} and efficiency than the planar sample. In spite of the poor fill factors, these data show that, at low minority carrier diffusion lengths, structuring of the junction can lead to an improvement in charge carrier collection.

Given the consistently poor fill factor in all but the planar, 800ºC samples, we explored the possibility that Au doping or one of the processing steps was causing an increase the sample resistivity. To accomplish this, planar samples were doped with Au as usual at 1000ºC, and two ohmic contacts were made to the same sample with Ga/In eutectic by the usual procedure (see Experimental). Measurement of the two-point I-V curves on each sample then yielded linear plots from which the total resistance of the contacts and samples could be extracted. The values found from these measurements were typically quite high, in the range of kΩ. When the same experiment is conducted on Si that has not been treated in any way, the contact resistance is usually 10-15 Ω per contact, and the Si resistance is usually about 100-200 Ω for this geometry. Thus, either poor contact is being made to the electrodes, or the resistivity of the Si has increased significantly.

Further studies using the four-point probe technique, which should eliminate any contact resistance,[62] showed very high resistivities in Au-doped Si, on the order of 100 Ω-cm. This is more than an order of magnitude higher than what is observed before Au doping (typically 5-7 Ω-cm). Furthermore, the observed increase in resistivity is certainly due to the evaporation and drive in of Au as heating samples in the absence of Au does not produce a measurable change in their resistivity. The increase in resistance

of samples with high concentrations of gold has been shown previously, where it was observed that the sample resistivity could increase by up to four orders of magnitude when the Au concentration was comparable to or greater than the dopant level in n-type Si.[58] This effect is believed to originate from the ionization of donor atoms into the Au state that is slightly above midgap in Si.[58,62] Thus, for the samples used in this study, which have a doping level near 10^{15} cm^{-3}, a large increase in resistance is expected at high Au concentrations. In this case, the increase is only a little more than one order of magnitude, which provides further evidence that the Au concentration is not as high as expected based on the solubility limit at the drive-in temperature.

The observation of very high resistivity in Au-doped Si accounts only in part for the poor fill factors observed. Even with a resistivity of 100 Ω-cm, the dimensions of the

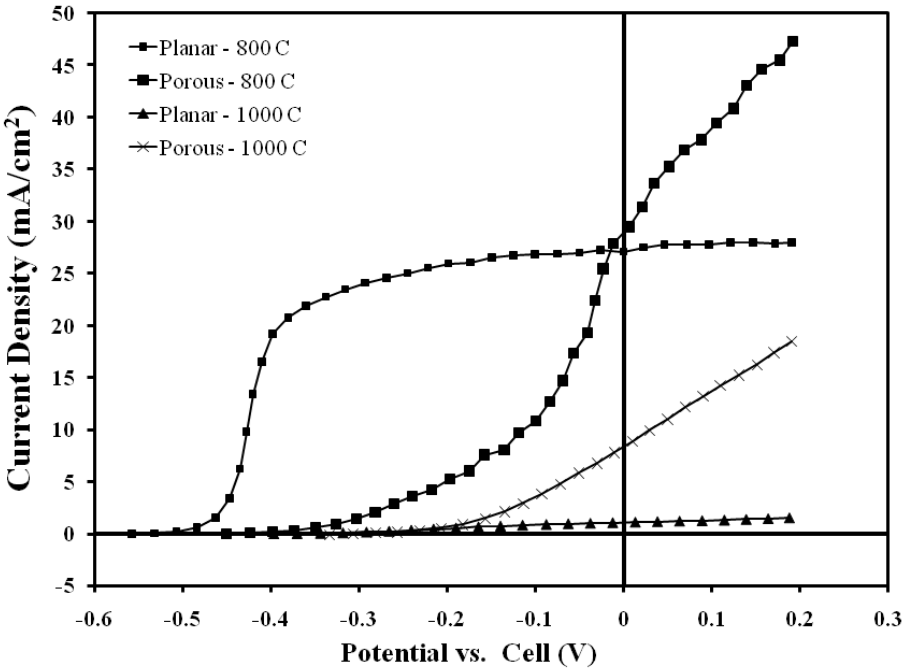

Figure 3.10. *J-E curves for porous and planar samples with significant Au doping after correction for 300 Ω series resistance. These samples are still not corrected for the expected solution resistance or the concentration overpotential losses. Representative samples are shown.*

electrodes are such that the uncompensated resistance due to the sample is expected to be around 300 Ω. The data from Figure 3.9 are replotted in Figure 3.10 after correction for 300 Ω series resistance. For the planar sample driven in at 800ºC, the correction for this resistance is probably too much since the concentration overpotential loss has not been accounted for in this plot, and we expect the resistance to be less for samples treated at 800ºC. For the other Au-doped samples, the fill factor remains quite poor in spite of the correction for the expected resistance. Thus, it is likely that there are other contributors to the observed low fill factors. Nevertheless, these data do show some improvement when changing from planar to porous in samples driven in at 1000ºC.

3.4.2.4 Continuation Advice

Continuation of this work would necessitate the understanding of the two key issues faced in reliably making and measuring Au-doped structured samples as photoelectrodes. First, the mechanism responsible for the decrease in lifetime observed upon heating pristine Si under an inert atmosphere would need to be elucidated. A good starting point for this would be to use a different tube and tube furnace in order to eliminate the equipment used as a possible source of contamination. Even with fine control over the Au doping procedure, the nature of the increased resistivity observed in the presence of high Au concentrations may be another barrier to producing reliable photoelectrochemical measurements. One avenue to pursue on this front would be to use more highly doped Si, although this would significantly change the size of the pores produced during anodization. As another avenue, one could perform diffusion doping on the porous samples after Au doping to lower the sample resistivity. Control of this

system and its further study may also prove beneficial as a method for understanding the materials properties of Si wires grown by chemical vapor deposition from metal catalysts (see chapters 4 and 5).

3.4.3 Reactive Ion Etched Pillars

In order to show experimental evidence that increased junction area leads to a decreased V_{oc}, with all other factors being the same, reactive ion etching (RIE) was used to produce Si pillars from high quality n-type Si with known materials properties.[3,4] A cryogenic inductively coupled plasma (ICP) RIE system was used to produce pillars with extremely high aspect ratios by etching away the surrounding Si (Figure 3.11). The ring visible halfway up the pillars in Figure 3.11 is due to the two-step etching approach that was used to make the wires longer. The initial phase of the etching undercuts the pattern

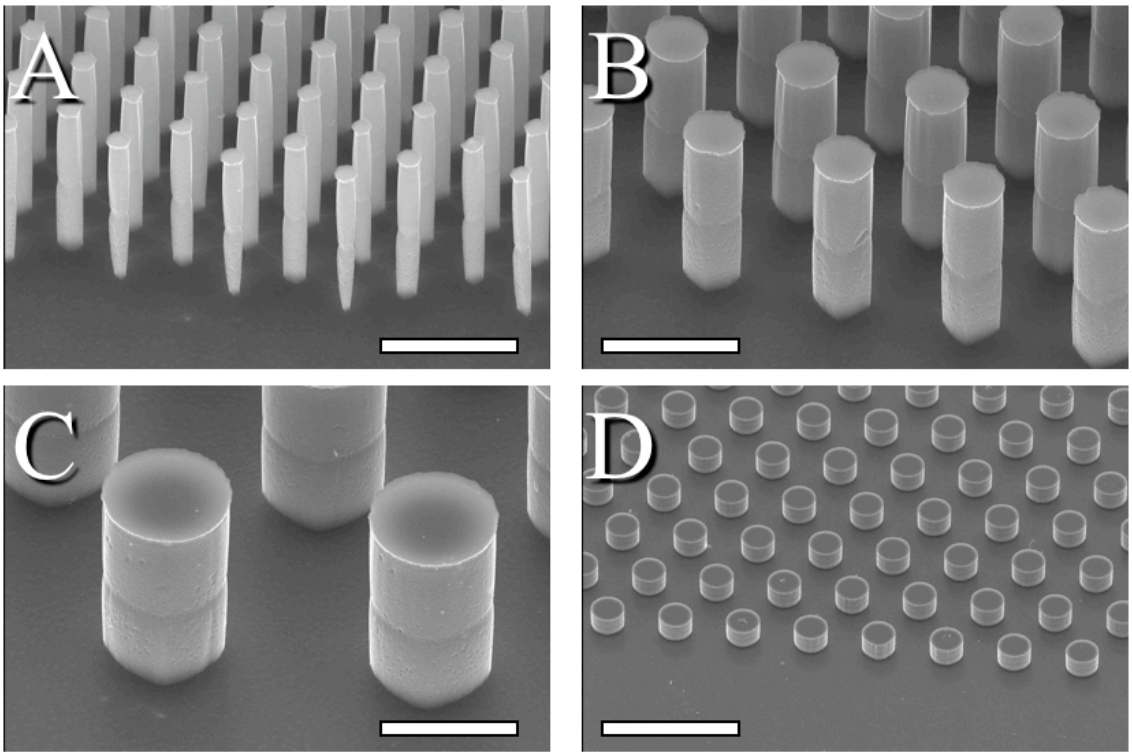

Figure 3.11. *SEM micrographs of RIE pillars. All are shown at a 45° angle. A) 5 µm pillar mask. Scale bar, 20 µm. B) 10 µm pillar mask. Scale bar, 20 µm. C) 20 µm pillar mask. Scale Bar, 20 µm. D) 50 µm pillar mask. Scale bar, 200 µm.*

slightly, giving rise to a ring at the top, and the process is reinitiated after some etching has been accomplished to increase the pillar length, causing another ring in the middle of the pillars. Four different pillar arrays were fabricated with pillar diameters of 5, 10, 20, and 50 μm. Each of the arrays of pillars produced was hexagonally arranged with the closest edge-to-edge distance equal to the diameter of the pillars. In this way, fractional filling area of Si in the pillar layer is the same in each array, so that the primary change is in the total junction area of the array. Thus, we expect to see a decrease in V_{oc} with decreasing pillar diameter due to the increased junction area.

Representative *J-E* curves for RIE pillar arrays are shown in Figure 3.12. The planar sample shown is derived from the sections of the sample that were not patterned and is therefore representative of the state of the wafer surface after the RIE procedure. It

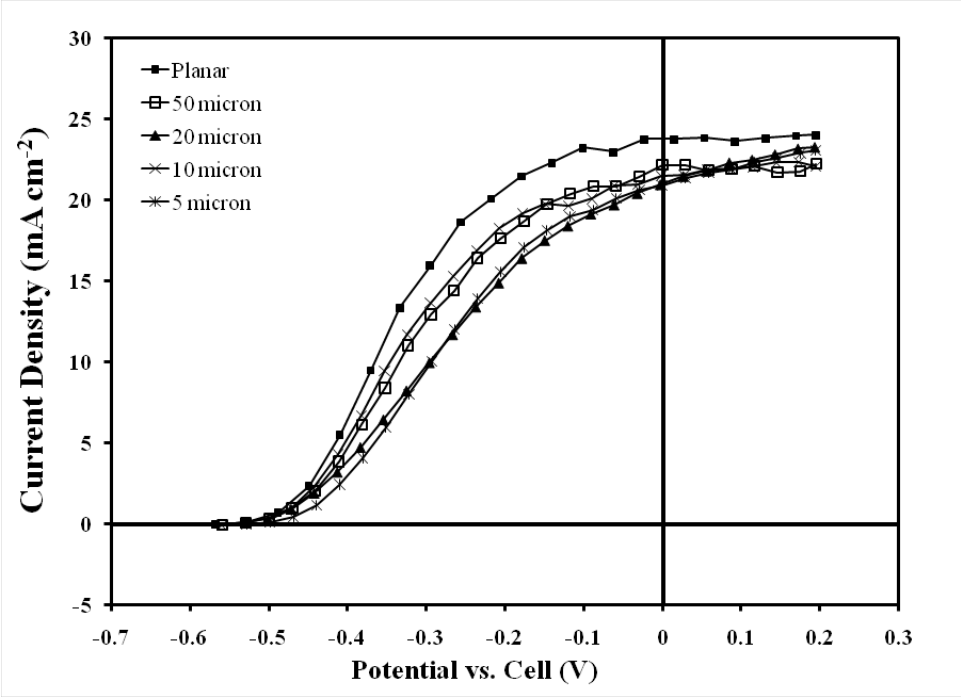

Figure 3.12. *J-E curves of RIE pillar array samples under simulated AM 1.5 illumination. Representative samples are shown. Note that the curves are similar for all array dimensions tested. Cell setup and contents are described in the Experimental Section.*

was found to be vitally important to the photoelectrochemical behavior of the pillar arrays to remove the near surface layer of the Si. Therefore, the results shown in Figure 3.12 are for samples that have been thermally oxidized and etched back to remove approximately the top 50 nm of Si from the surface. From this figure, it is apparent that the *J-E* curves show similar characteristics across all of the pillar diameters tested.

The solar cell performance figures of merit for the pillar arrays are shown in Table 3.5. Most of the figures of merit are the same across all conditions tested to within the error of the measurements. In particular, the measured voltages are indistinguishable. With pillars that are 5 μm in diameter and only 30 μm long, the surface area enhancement factor, γ, is approximately 12 (See Section 1.3.1). Thus, we would expect a decrease in V_{oc} of ~64 mV for 5 μm diameter pillars as compared with the planar sample. Clearly, this trend is not observed in the data presented here. However, the calculation of 60 mV V_{oc} loss per decade of surface area enhancement assumes that the charge carriers are harvested uniformly across all of the junction area. Any deviation from this assumption is expected to decrease the total voltage reduction observed. This is because non-uniform

Table 3.5. *Solar cell figures of merit for pillar arrays. Values reported are the average of three independent electrodes. Planar samples were taken from the same substrate as the pillar array samples. Errors reported are the standard error of the mean.*

Pillar Diameter	J_{sc} (mA cm^{-2})	V_{oc} (mV)	Fill Factor (%)	Efficiency (%)
Planar	26.6 ± 1.9	532 ± 10	37.0 ± 0.4	5.2 ± 0.4
5 μm	22.4 ± 1.5	523 ± 15	34.6 ± 0.9	4.1 ± 0.5
10 μm	20.6 ± 0.8	538 ± 1	37.6 ± 2.0	4.2 ± 0.1
20 μm	18.2 ± 1.3	535 ± 5	34.0 ± 2.9	3.3 ± 0.1
50 μm	21.1 ± 0.2	538 ± 2	37.8 ± 1.5	4.3 ± 0.2

harvesting of minority carriers across the junction will lead to areas with high voltages and areas with low voltages. These localized areas will then behave like diodes connected in parallel with each other, in which case the total observed voltage is expected to be only slightly lower than that in the high voltage regions.[63] Coupled with the fact that a reduced V_{oc} was observed with increasing pore length in Chapter 2, the results presented here therefore imply that there is a nonuniform voltage generated across the sample. Given that the pillars are only 30 μm tall and spaced relatively far apart, we suggest that the observed constant V_{oc} is due to the contribution of the substrate, which is probably absorbing most of the carriers in this geometry. Since the arrays used were designed to have a constant filling fraction of wires, the substrate makes the same contribution in all array sizes. Therefore, we propose that the effect of increased junction area in the pillars is not the primary factor being probed in these experiments, but rather the constant junction area of the underlying substrate.

In order to use RIE pillars to demonstrate the desired dependence of V_{oc} on junction area, it would be necessary to use significantly longer pillars packed much closer together. With more light absorbed by the pillars, their effect on the observed photoelectrochemical properties will be larger. Furthermore, these results demonstrate the danger in assuming uniform distribution of carriers across the junction area when using a light source that is incident from the tops of the structures. In future studies, it will be important to optimize the structures used and to use wavelengths of light that give rise to relatively uniform carrier generation throughout the volume of the structured sample.

3.5 Conclusions

The studies contained in this chapter were directed toward proving that the possibility for radial charge carrier collection should increase J_{sc} in materials of low quality and that increasing junction area at a constant light flux should lead to a lowered V_{oc}. By diffusing Au into Si at high temperatures, an improvement in J_{sc} for porous samples over planar samples was shown for materials with low minority carrier diffusion lengths. However, the performance of both porous and planar samples with high concentrations of Au showed poor fill factors which could not be explained by the observed increase in the resistivity of the substrates following Au drive in. It is interesting to note that low fill factors have also typically been observed in Si wire arrays grown by the chemical vapor deposition method from Au catalyst (see chapters 4 and 5). It is possible that there is a common mechanism leading to the observed poor fill factors in samples having high concentrations of metals, even accounting for a change in the resistivity of the material. Future research on the photoelectrochemical performance of Si wire arrays would benefit from a more detailed understanding of this phenomenon.

Silicon pillar array samples with a range of diameters were found to have nearly identical values of V_{oc} for all sizes of pillars tested and for planar samples. This result does not invalidate the expectation that increased junction area per unit of projected surface area will lead to a decrease in V_{oc}. Rather, it points to the fact that care must be taken in design of physical model systems. In this case, it is likely that the photoelectrochemical behavior of the samples was dominated by contributions from the substrate rather than from the pillars themselves. Thus, further physical model systems

will require either separation of the structured material from the substrate or densification of the structured material so that the majority of the incident radiation is absorbed in the structured layer.

3.6 References

1. Maiolo, J. R.; Atwater, H. A.; Lewis, N. S. *J. Phys. Chem. C* **2008**, *112*, 6194-6201.
2. Kayes, B. M.; Atwater, H. A.; Lewis, N. S. *J. Appl. Phys.* **2005**, *97*, 114302.
3. Henry, M. D.; Walavalkar, S.; Homyk, A.; Scherer, A. *Appl. Phys. Lett.* **2009**, *submitted*.
4. Henry, M. D.; Welch, C.; Scherer, A. *J. Vac. Sci. Technol. A* **2009**, *submitted*.
5. Uhlir, A. Bell. Sys. Tech. J. **1956**, 35, 333-347.
6. Canham, L. T. J. Phys. Chem. Solids **1986**, 47, 363-373.
7. Canham, L. T. *Appl. Phys. Lett.* **1990**, *57*, 1046-1048.
8. Turner, D. R. J. Electrochem. Soc. **1958**, 105, 402-408.
9. Shapley, J. D. L.; Barrow, D. A. *Thin Solid Films* **2001**, *388*, 134-137.
10. Lehmann, V. Electrochemistry of Silicon: Instrumentation, Science, Materials and Applications; Wiley-VCH, 2002.
11. Sailor, M. J.; Lee, E. J. *Adv. Mater.* **1997**, *9*, 783-793.
12. Propst, E. K.; Rieger, M. M.; Vogt, K. W.; Kohl, P. A. *Appl. Phys. Lett.* **1994**, *64*, 1914-1916.
13. Doan, V. V.; Sailor, M. J. *Appl. Phys. Lett.* **1992**, *60*, 619-620.
14. Parkhutik, V. Solid-State Electron. **1999**, 43, 1121-1141.
15. Lehmann, V. J. Electrochem. Soc. **1993**, 140, 2836-2843.
16. Ottow, S.; Lehmann, V.; Foll, H. *Appl. Phys. A-Mater. Sci. Process.* **1996**, *63*, 153-159.
17. Ottow, S.; Lehmann, V.; Foll, H. *J. Electrochem. Soc.* **1996**, *143*, 385-390.
18. Lehmann, V.; Föll, H. *J. Electrochem. Soc.* **1990**, *137*, 653-659.
19. Lehmann, V. *Thin Solid Films* **1995**, *255*, 1-4.
20. Chazalviel, J. N.; Wehrspohn, R. B.; Ozanam, F. *Mater. Sci. Eng. B-Solid State Mater. Adv. Technol.* **2000**, *69*, 1-10.
21. Ross, F. M.; Oskam, G.; Searson, P. C.; Macaulay, J. M.; Liddle, J. A. *Philos. Mag. A-Phys. Condens. Matter Struct. Defect Mech. Prop.* **1997**, *75*, 525-539.
22. Föll, H.; Christophersen, M.; Carstensen, J.; Hasse, G. *Mater. Sci. Eng. R-Rep.* **2002**, *39*, 93-141.

23. Zhang, X. G. J. Electrochem. Soc. **2004**, 151, C69-C80.

24. Searson, P. C.; Macaulay, J. M.; Ross, F. M. *J. Appl. Phys.* **1992**, *72*, 253-258.

25. Al Rifai, M. H.; Christophersen, H.; Ottow, S.; Carstensen, J.; Foll, H. *J. Electrochem. Soc.* **2000**, *147*, 627-635.

26. Tan, M. X.; Laibinis, P. E.; Nguyen, S. T.; Kesselman, J. M.; Stanton, C. E.; Lewis, N. S. In *Progress In Inorganic Chemistry, Vol 41*; John Wiley & Sons Inc: New York, 1994; Vol. 41, p 21-144.

27. Kopitkovas, G.; Mikulskas, I.; Grigoras, K.; Šimkienė, I.; Tomasiunas, R. *Appl. Phys. A* **2001**, *73*, 495-501.

28. Panek, P.; Dutkiewicz, J.; Levy-Clement, C.; Lipinski, M.; Bielanska, E.; Wodnicka, K. *Arch. Metall. Mater.* **2005**, *50*, 417-421.

29. Brendel, R.; Feldrapp, K.; Horbelt, R.; Auer, R. *Phys. Status Solidi A-Appl. Res.* **2003**, *197*, 497-501.

30. Lehmann, V.; Stengl, R.; Reisinger, H.; Detemple, R.; Theiss, W. *Appl. Phys. Lett.* **2001**, *78*, 589-591.

31. Grüning, U.; Lehmann, V.; Ottow, S.; Busch, K. *Appl. Phys. Lett.* **1996**, *68*, 747-749.

32. Müller, F.; Birner, A.; Gösele, U.; Lehmann, V.; Ottow, S.; Föll, H. *J. Porous Mat.* **2000**, *7*, 201-204.

33. Lehmann, V.; Grüning, U. *Thin Solid Films* **1997**, *297*, 13-17.

34. Matthias, S.; Müller, F.; Schilling, J.; Gösele, U. *Appl. Phys. A* **2005**, *80*, 1391-1396.

35. Schilling, J.; Müller, F.; Matthias, S.; Wehrspohn, R. B.; Gösele, U.; Busch, K. *Appl. Phys. Lett.* **2001**, *78*, 1180-1182.

36. Matthias, S.; Müller, F.; Gösele, U. *J. Appl. Phys.* **2005**, *98*.

37. Tian, L.; Ram, K. B.; Ahmad, I.; Menon, L.; Holtz, M. *J. Appl. Phys.* **2005**, *97*.

38. Bastide, S.; Levy-Clement, C. Journal of New Materials for Electrochemical Systems **2006**, 9, 269-275.

39. Gangopadhyay, U.; Dhungel, S. K.; Basu, P. K.; Dutta, S. K.; Saha, H.; Yi, J. *Sol. Energ. Mat. Sol.* **2007**, *91*, 285-289.

40. Huang, M. J.; Yang, C. R.; Chiou, Y. C.; Lee, R. T. *Sol. Energ. Mat. Sol.* **2008**, *92*, 1352-1357.

41. Levy-Clement, C.; Lust, S.; Bastide, S.; Le, Q. N.; Sarti, D. *Phys. Status Solidi A-Appl. Res.* **2003**, *197*, 27-33.

42. Lipinski, M. Arch. Metall. Mater. **2008**, 53, 185-187.

43. Lipinski, M.; Panek, P.; Czternastek, H. *Molecular Physics Reports* **2002**, *36*, 123-6.

44. Panek, P. Opto-Electronics Review **2004**, 12, 45-48.

45. Yae, S.; Kobayashi, T.; Kawagishi, T.; Fukumuro, N.; Matsuda, H. *Sol. Energy* **2006**, *80*, 701-706.

46. Clarkson, J. P.; Sun, W.; Hirschman, K. D.; Gadeken, L. L.; Fauchet, P. M. *Phys. Status Solidi A-Appl. Mat.* **2007**, *204*, 1536-1540.

47. Kelly, J. J.; Vanmaekelbergh, D. In *Electrochemistry of Nanomaterials*; Hodes, G., Ed.; Wiley-VCH: New York, 2001, p 103-139.

48. Erné, B. H.; Vanmaekelbergh, D.; Kelly, J. J. *J. Electrochem. Soc.* **1996**, *143*, 305-314.

49. Erné, B. H.; Vanmaekelbergh, D.; Kelly, J. J. *Adv. Mater.* **1995**, *7*, 739-742.

50. Lewis, N. S. J. Electrochem. Soc. **1984**, 131, 2496-2503.

51. Rosenbluth, M. L.; Lewis, N. S. *J. Phys. Chem.* **1989**, *93*, 3735-3740.

52. Gstrein, F.; Michalak, D. J.; Royea, W. J.; Lewis, N. S. *J. Phys. Chem. B* **2002**, *106*, 2950-2961.

53. Groner, M. D.; Koval, C. A. *J. Electroanal. Chem.* **2001**, *498*, 201-208.

54. Gibbons, J. F.; Cogan, G. W.; Gronet, C. M.; Lewis, N. S. *Appl. Phys. Lett.* **1984**, *45*, 1095-1097.

55. Gronet, C. M.; Lewis, N. S.; Cogan, G. W.; Gibbons, J. F. *Proc. Natl. Acad. Sci.* **1983**, *80*, 1152-1156.

56. Rosenbluth, M. L.; Lieber, C. M.; Lewis, N. S. *Appl. Phys. Lett.* **1984**, *45*, 423-425.

57. Cogan, G. W.; Gronet, C. M.; Gibbons, J. F.; Lewis, N. S. *Appl. Phys. Lett.* **1984**, *44*, 539-541.

58. Bullis, W. M.; Strieter, F. J. *J. Appl. Phys.* **1968**, *39*, 314-&.

59. Wilcox, W. R.; Lachapelle, T. J. *J. Appl. Phys*. **1964**, *35*, 240-&.

60. Struthers, J. D. *J. Appl. Phys.* **1956**, *27*, 1560-1560.

61. Lewis, N. S.; Gronet, C. M. *Appl. Phys. Lett.* **1983**, *43*, 115-117.

62. Sze, S. M. *Physics of Semiconductor Devices*; 2nd ed.; John Wiley & Sons: New York, 1981.

63. Green, M. A. J. Phys. D Appl. Phys. **1976**, 9, L57-L59.

Chapter 4

High Aspect-Ratio Silicon Wire Array Photoelectrochemical Cells

4.1 Abstract

In an effort to develop low-cost solar energy conversion techniques, high uniformity vertically oriented silicon wire arrays have been fabricated. These arrays, which allow for radial diffusion of minority charge carriers, have been measured in a photoelectrochemical cell. Large photovoltages (~400 mV) have been measured, and these values are significantly greater than those obtained from the substrate alone. Additionally, the wire array samples displayed much higher current densities than the underlying substrate, demonstrating that significant energy conversion was occurring due to the absorption and charge-carrier transport in the vertically aligned Si wires. This method therefore represents a step toward the use of collection-limited semiconductor materials in a wire array format in macroscopic solar cell devices.

4.2 Introduction

A key constraint in photon absorbers for solar energy conversion is that the material must be sufficiently thick to absorb most of the solar photons with energies above the material's band gap, yet sufficiently pure to have a high minority-carrier diffusion length for effective collection of the photogenerated charge carriers. This constraint imposes a cost floor on the absorber material by dictating the minimum required purity of the absorber phase. The situation is especially severe for indirect band-gap absorbers, such as Si which requires over 100 μm of thickness to absorb 90% of the energy in sunlight above the 1.12 eV band gap of Si.[1,2]

One approach to circumventing this constraint is to orthogonalize the directions of light absorption and charge-carrier collection.[2] One attractive realization of such an approach involves high aspect-ratio cylindrical absorbers, such as nanowires. A preferred implementation would involve the use of wires that are sufficiently long to absorb most of the incident light, but which have sufficiently small diameters to facilitate efficient radial collection of carriers, even for relatively impure absorber materials. To fabricate such a solar cell, methods are required to prepare large area arrays of vertically aligned nanowires, to make electrical junctions to such wire arrays, and to make electrical contacts to the backsides of these devices. These challenges have been investigated by various means, including chemical vapor deposition (CVD) growth of wire arrays,[3,4] etching of flat substrates to produce wire arrays,[5,6] and conductive-polymer electrical junctions with wires.[7,8] Nanowires have also been used to facilitate collection of majority carriers in ZnO-based dye-sensitized solar cells.[9] We report herein the demonstration of

all of these steps for absorbers that consist of arrays of high aspect-ratio, CVD-grown, crystalline Si wires. Silicon is used in most current solar cells, and the fabrication of devices from Si is technologically well-developed, so methods for using less pure Si in solar energy conversion devices are of significant interest.

4.3 Experimental

4.3.1 Fabrication of Wire Array Samples and Controls

Degenerately doped N-type Si(111) wafers (0.004 Ω-cm) were thermally oxidized to produce a 285 nm oxide film. These wafers were then coated with S1813 photoresist (Microchem), exposed to the pattern (square array of 3 μm holes, 7 μm center to center), and developed in MF319 (Microchem). The wafers were then etched for 4 min in buffered-HF improved (Transene) (CAUTION: fluoride-containing solutions such as 11 M (40% by weight) NH_4F, buffered HF, and 27 M (48% by weight) HF pose a serious contact hazard. Hydrofluoric acid is highly toxic and corrosive and may cause serious burns which may not be immediately painful or visible. Fluoride ions readily penetrate the skin and can cause destruction of deep tissue and bone), followed by thermal evaporation of 500 nm gold and lift-off of the photoresist, to leave the catalyst islands separated by an oxide buffer. The samples were then brought into a tube furnace at 1050°C and annealed in H_2 for 20 min at a flow rate of 1000 sccm. The wires were subsequently grown for 20 min in a mixture of H_2 (1000 sccm) and $SiCl_4$ (20 sccm). Control samples consisted of oxidized wafers that contained patterned openings in the oxide, but no gold was deposited, and wires were not grown on such samples.

4.3.2 Photoelectrochemical Measurements

Following growth, the wire array samples were etched for 10 s in 10% HF(aq) to remove the native oxide. The samples were then soaked for 10 min in TFA solution (Transene), which contains I^-/I_3^-, to etch away the gold particles. SEM images confirmed removal of the bulk of the Au catalyst particle, although a hollow shell of material appeared to remain (See Figure 4.1 A). The wire array samples were subsequently dipped in 1 M HCl(aq) and rinsed with H_2O. The samples were then etched for 10 s in 10% HF(aq) to remove native oxide, rinsed with H_2O, and dried under a stream of N_2. Ga/In was immediately rubbed onto the back of the sample, and the samples were attached to a wire coil using silver paint. The samples were then sealed inside a glass tube, leaving ~ 2 mm^2 of exposed front surface area, using 20-3004 LV epoxy (Epoxies, Etc.) to coat the front face and sealing the rest of the sample with Hysol 1C epoxy (Loctite). Control samples were prepared similarly.

The photoelectrochemical measurements were performed in a solution consisting of 200 mM of dimethylferrocene (Me_2Fc), 0.5 mM of Me_2FcBF_4, and 1 M of $LiClO_4$ in methanol. Methanol was clearly observed to wet the wire array surfaces during both processing and photoelectrochemical measurements. The working electrode was either a wire array sample or a control sample. The counter electrode was a Pt mesh, and the reference electrode was a Pt wire enclosed in a Luggin capillary that contained the same solution as the main cell. All cell components were assembled under an inert atmosphere and were sealed before being placed under positive pressure of Ar. During measurements, the cell was illuminated using a 300 W ELH-type projector bulb. The

light intensity was calibrated using a Si photodiode to produce a photocurrent equivalent to that obtained under 100 mW cm^{-2} of AM1.5 illumination at the working electrode surface. The solution was stirred vigorously during measurement, and a stream of air was used to keep the cell temperature constant under illumination.

Photoelectrochemical measurements were conducted using a Solartron 1287 potentiostat and the CoreWare software. To measure the open-circuit voltage in the light, the open-circuit potential was first allowed to equilibrate in the dark (always to within 10 mV of 0 V). The light was then switched on and the sample was allowed to equilibrate in the light. The reported V_{oc} is the difference between the potential in the dark and the potential in the light. *J-V* data were then recorded in the light at a scan rate of 10 mV s^{-1}. The short-circuit photocurrent densities were recorded as the current density measured at a bias of 0 V vs the Nernstian potential of the cell. The electrode area used to calculate the current density was measured using a flatbed scanner. Averages shown are for six wire array samples and four control samples, with the indicated error equal to the standard error of the mean.

4.3.3 Single Wire Measurements

The as-grown wires were removed from the growth substrate by sonication in isopropanol, and were then spin-coated onto a degenerately doped (n-type) silicon wafer that was covered with 100 nm of Si_3N_4. The substrate was then coated with lift-off resist (LOR3A, Microchem), followed by photoresist (S1813, Microchem). The electrodes were aligned to the wire samples using a Suss MA-6 mask aligner. Following pattern development, the wire samples were etched for 20 s in buffered HF(aq) to remove the

native oxide, and 300 nm of Al, followed by 800 nm Ag, was then thermally evaporated onto the sample. The contacts were subsequently annealed at 250°C for 30 min in forming gas (90% N_2, 10% H_2). An example device is shown in the inset of Figure 4.3. Ohmic behavior was observed for the annealed Al contacts, and the resistivity was calculated based on the probe spacing and wire diameter (as determined by SEM). To determine the carrier type, the conductivity of the sample was measured at various back gate bias potentials between -60 V and 60 V. The samples were found to be n-type, based on the increase in conductivity with increasing gate bias.

4.4 Results and Discussion

Arrays of Si wires were grown using the vapor-liquid-solid (VLS) growth method, with Au as the VLS catalyst.[10-12] A 285 nm thick SiO_2 buffer layer was first thermally grown on the substrate, which was a degenerately doped n-type Si(111) wafer. Oxide deposition was followed by application of a resist layer. A pattern of holes in the resist and oxide was then formed using photolithography and subsequent etching through the oxide. The Au catalyst was then thermally evaporated onto the substrate, and excess Au removed during resist lift-off. VLS growth was then performed at 1050°C using $SiCl_4$ diluted in H_2, producing 10-30 μm long Si wires having the desired radii and pitch. Following growth, the remaining Au catalyst was removed from the wires.[13] As shown in Figure 4.1, the resulting Si wires were nearly completely oriented normal to the substrate and were highly regular, in both diameter and pitch, over a large (~2 mm^2) area.[11]

Although gold is a deep-level trap in silicon, the wires grown in this study are nevertheless expected to allow effective carrier collection. Because the solubility limit of

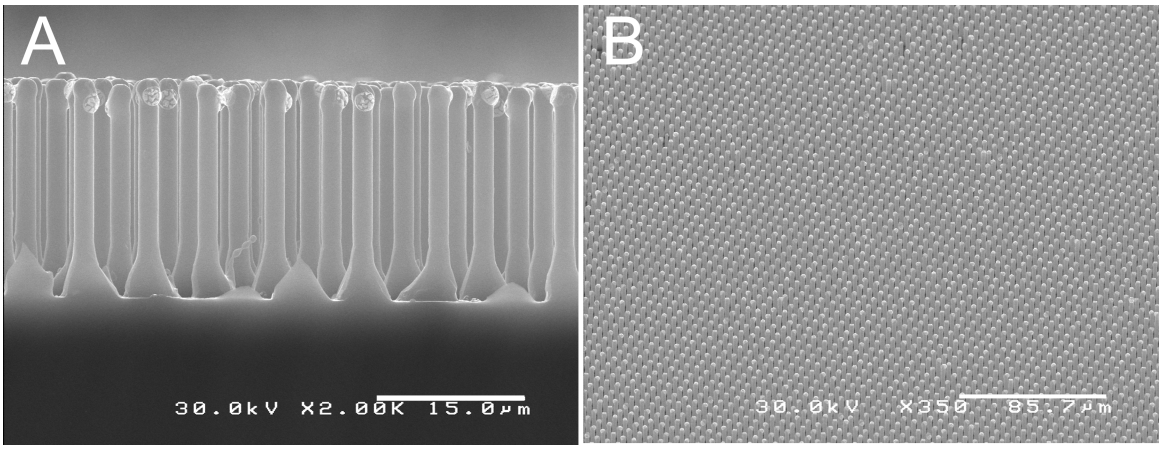

Figure 4.1. *Scanning electron microscopy images of silicon wire arrays. (A) Cross section. Scale bar, 15 µm. (B) 45° view. Scale bar, 85.7 µm.*

Au in Si at 1050°C is ~10^{16} cm^{-3}, the trap cross-section of Au is expected to produce carrier lifetimes of 2 ns.[1,14] This short lifetime would greatly restrict carrier collection in planar Si absorbers, but nevertheless is adequate to provide carrier collection for distances of at least 1 µm.[1] A theoretical treatment has shown that optimal efficiencies are expected when the wires have a diameter comparable to the minority-carrier diffusion length.[2] Smaller diameters produce increased surface area, and thus increase surface and junction recombination with little concomitant improvements in carrier collection. Hence, micron-diameter Si wires were grown and used in the array junction measurements.

Transmission electron microscopy (TEM) characterization of the wires indicated that they were single crystalline and grew in the <111> direction, as expected from the orientation of the substrate wafer (Figure 4.2).[11] Four-point probe measurements and field-effect measurements on individual nanowires indicated that the as-grown wires were n-type, with resistivities of 0.32 Ω-cm, corresponding to dopant densities of 2.5x10^{16} cm^{-3} (Figure 4.3).[15]

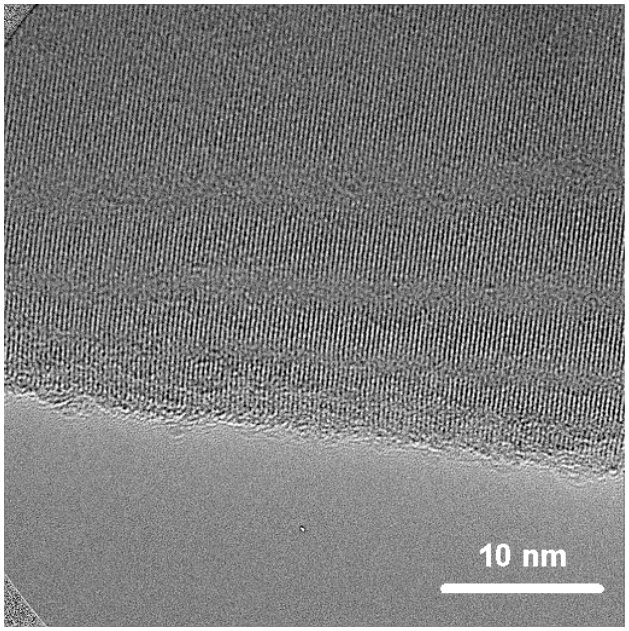

Figure 4.2. *TEM image of a Au-catalyzed, $SiCl_4$-grown, nanowire.[11] The scale bar is 10 nm. The vertical lines are lattice fringes; the horizontal bands are due to the curved surface of the wire causing interference fringes. No crystal defects were observed by TEM in the wires. A lattice spacing of 0.307 ± 0.004 nm is inferred from these images. This lattice spacing, combined with the fact that the wires grew as single crystals normal to a Si(111) wafer, is consistent with the growth being in the <111> direction (the Si (111) lattice parameter is ~0.314 nm).*

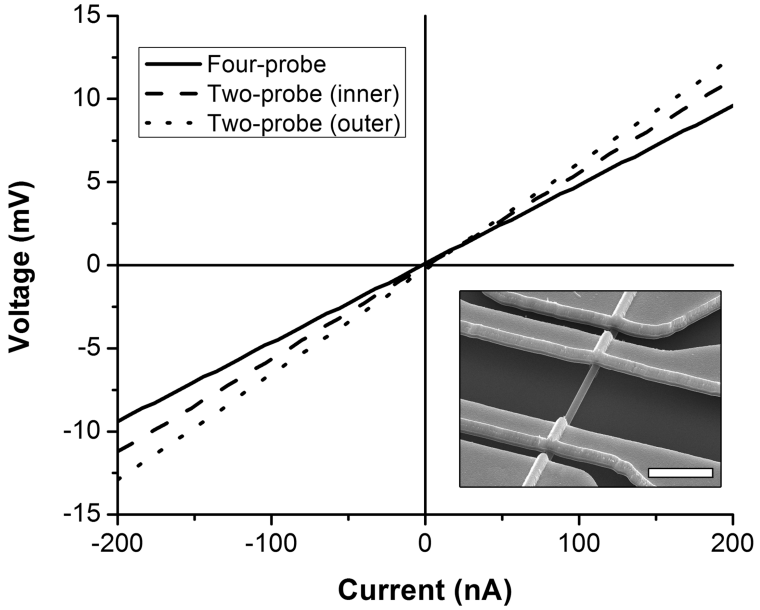

Figure 4.3. *Typical I-V measurement for an individually contacted wire using the four-point probe technique.[15] The wire resistance was 50 kΩ for this sample, corresponding to a doping level of 2.9×10^{16} cm^{-3}, assuming the same carrier mobility as in bulk Si. Inset: a SEM image of a four-point probe measurement device, viewed at 45°. The scale bar is 6 μm.*

The junction properties of such Si wire arrays were probed using a liquid electrolyte. The liquid electrolyte provided a convenient, conformal method of contacting the Si wires, and allowed measurements of the performance of the wires without requiring a diffused metallurgical junction to the Si wires in the array. In particular, the 1,1'-dimethylferrocene $(Me_2Fc)^{+/0}$ redox system in CH_3OH has been shown to yield excellent junctions with n-type Si, providing bulk diffusion-recombination limited photovoltages in excess of 670 mV under 100 mW cm^{-2} of AirMass (AM) 1.5 conditions.[16-20] Such junctions also form an in situ inversion layer in the n-Si, in essence forming an in-situ p^+ emitter layer, while also producing a highly passivated surface.[21] Hence these liquid junctions are well-suited as systems for providing initial probes of the solar device conversion properties of arrays of n-type Si wires. This expectation has been verified by measurements of photoelectrodes made from n-type macroporous Si, which have shown that high photovoltages can be obtained even with significant increases in surface area of the junction relative to the geometric projected area of the substrate, through use of the $Me_2Fc^{+/0}$-CH_3OH liquid contact.[22]

Table 4.1 summarizes the average values for the open-circuit voltage (V_{oc}) and short-circuit current density (J_{sc}) of the Si wire array photoelectrodes. To generate control samples, an oxidized substrate wafer was patterned with holes, but no catalyst

Table 4.1. *Photocurrent and photovoltage of wire array cells*

	V_{oc} (mV)	J_{sc} (mA/cm^2)
Wire Array	389 ± 18	1.43 ± 0.14
Control	232 ± 8	0.28 ± 0.01

was deposited into the openings, and wires were not grown on the samples. The V_{oc} in the wire array samples was relatively large (350-400 mV) given the high surface area per unit projected area. This value of V_{oc} reflects the relatively low surface recombination velocity of the Si/$Me_2Fc^{+/0}$-CH_3OH interface and good bulk properties of the Si wires, without which much lower V_{oc} values would be observed. The short-circuit photocurrent densities of the wire array samples were relatively low, 1-2 mA cm^{-2}. However, the wires were only 20 μm in length, so the expected J_{sc} of 43 mA cm^{-2} that could be attained for complete absorption and collection of all solar photons with energies above the 1.12 eV band gap of Si is reduced to 34 mA cm^{-2} for a 20 μm thickness of Si absorber.[1,2] In addition, the array of 2 μm diameter wires on a 7 μm pitch only fills 6.5% of the projected surface plane, thereby producing an expected maximum J_{sc} of 2.2 mA cm^{-2}, in agreement with the observed J_{sc}.

Representative current density vs voltage curves are shown in Figure 4.4. The fill factor was relatively low, and presumably reflects either a shunt or residual recombination at the junction that could potentially be reduced through improved surface passivation methods. The observed photoactivity was not dominated by the substrate, because the degenerately doped substrate produced only a low photovoltage and nearly no photocurrent. In addition, the wide bases of the wires suggest that relatively little, if any, direct contact was formed between any remaining oxide-free substrate and the liquid electrolyte. Thus, it is likely that all of the observed photocurrent and photovoltage are due to the wires rather than the substrate.

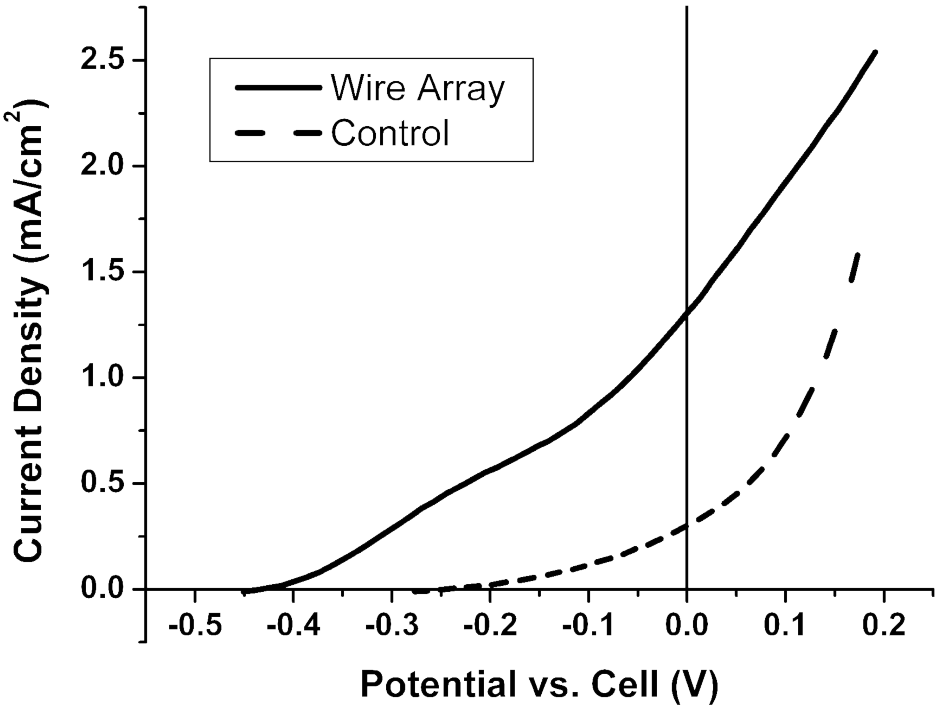

Figure 4.4. *Current density vs. voltage behavior for Si wire array (solid) and control samples (dashed). The electrode potential was measured vs. a Pt reference poised at the Nernstian potential of the 0.2 M Me_2Fc-0.5 mM Me_2Fc^+-1.0 M $LiClO_4$-CH_3OH cell.*

In summary, high fidelity, vertically aligned arrays of high aspect-ratio silicon wires have been fabricated over relatively large areas, and their energy conversion properties have been measured in a photoelectrochemical cell. Although the wires were grown with Au as the catalyst, the wire array samples showed significantly higher photocurrents and photovoltages than the control samples. Hence, as described herein, a nearly photoinactive substrate has been rendered photoactive by the scalable, relatively low cost, VLS growth of arrays of Si wires.

4.5 References

1. Sze, S. M. *Physics of Semiconductor Devices*; 2nd ed.; John Wiley & Sons: New York, 1981.
2. Kayes, B. M.; Atwater, H. A.; Lewis, N. S. *J. Appl. Phys.* **2005**, *97*, 114302.
3. Fan, H. J.; Fuhrmann, B.; Scholz, R.; Syrowatka, F.; Dadgar, A.; Krost, A.; Zacharias, M. *J. Cryst. Growth* **2006**, *287*, 34-38.
4. Lombardi, I.; Hochbaum, A. I.; Yang, P.; Carraro, C.; Maboudian, R. *Chem. Mat.* **2006**, *18*, 988-991.
5. Huang, Z. P.; Fang, H.; Zhu, J. *Adv. Mater.* **2007**, *19*, 744-+.
6. Peng, K. Q.; Xu, Y.; Wu, Y.; Yan, Y. J.; Lee, S. T.; Zhu, J. *Small* **2005**, *1*, 1062-1067.
7. Huynh, W. U.; Dittmer, J. J.; Alivisatos, A. P. *Science* **2002**, *295*, 2425-2427.
8. Lin, Y. T.; Zeng, T. W.; Lai, W. Z.; Chen, C. W.; Lin, Y. Y.; Chang, Y. S.; Su, W. F. *Nanotechnology (UK)* **2006**, *17*, 5781-5785.
9. Law, M.; Greene, L. E.; Johnson, J. C.; Saykally, R.; Yang, P. D. *Nat. Mater.* **2005**, *4*, 455-459.
10. Wagner, R. S.; Ellis, W. C. Transactions of the Metallurgical Society of Aime **1965**, 233, 1053-&.
11. Kayes, B. M.; Filler, M. A.; Putnam, M. C.; Kelzenberg, M. D.; Lewis, N. S.; Atwater, H. A. *Appl. Phys. Lett.* **2007**, *91*, 103110.
12. Westwater, J.; Gosain, D. P.; Usui, S. Jpn. J. Appl. Phys. Part 1 - Regul. Pap. Short Notes Rev. Pap. **1997**, 36, 6204-6209.
13. Woodruff, J. H.; Ratchford, J. B.; Goldthorpe, I. A.; McIntyre, P. C.; Chidsey, C. E. D. *Nano Lett.* **2007**, *7*, 1637-1642.
14. Struthers, J. D. *J. Appl. Phys.* **1956**, *27*, 1560-1560.
15. Kelzenberg, M. D.; Turner-Evans, D. B.; Kayes, B. M.; Filler, M. A.; Putnam, M. C.; Lewis, N. S.; Atwater, H. A. *Nano Lett.* **2008**, *8*, 710-714.
16. Gibbons, J. F.; Cogan, G. W.; Gronet, C. M.; Lewis, N. S. *Appl. Phys. Lett.* **1984**, *45*, 1095-1097.

17. Gronet, C. M.; Lewis, N. S.; Cogan, G. W.; Gibbons, J. F. *Proc. Natl. Acad. Sci.* **1983**, *80*, 1152-1156.

18. Rosenbluth, M. L.; Lewis, N. S. *J. Am. Chem. Soc.* **1986**, *108*, 4689-4695.

19. Rosenbluth, M. L.; Lewis, N. S. *J. Phys. Chem.* **1989**, *93*, 3735-3740.

20. Rosenbluth, M. L.; Lieber, C. M.; Lewis, N. S. *Appl. Phys. Lett.* **1984**, *45*, 423-425.

21. Gstrein, F.; Michalak, D. J.; Royea, W. J.; Lewis, N. S. *J. Phys. Chem. B* **2002**, *106*, 2950-2961.

22. Maiolo, J. R.; Atwater, H. A.; Lewis, N. S. *J. Phys. Chem. C* **2008**, *112*, 6194-6201.

Chapter 5

Improved Efficiency Silicon Wire Array Solar Cells

5.1 Abstract

In response to the work completed in Chapter 4, further studies of silicon wire arrays as photoelectrochemical solar cells were conducted. By using longer wires and optimizing the epoxy encapsulation, significantly improved short circuit current densities (J_{sc}) and fill factors were observed compared to previous results. Simultaneous with the improvement in J_{sc} and fill factor, a reduction in open circuit voltage (V_{oc}) was observed, but the overall energy conversion efficiency was still significantly improved over that observed in Chapter 4. Furthermore, verification that the photoactivity was due to the Si wires as opposed to the single-crystalline Si substrate was obtained by measuring the substrate after removal of the wires and by using scanning confocal microscopy to selectively excite the wires rather than the substrate. The observed energy conversion efficiencies can be significantly improved by correcting the raw data for both concentration overpotential losses and series resistance losses, and the validity of the concentration overpotential correction was verified by the use of a photoelectrochemical cell exhibiting significantly reduced concentration overpotentials. Finally etching of Si wires to remove the outer layers was preliminarily found to only decrease the observed efficiency, implying that further improvements in efficiency will require the use of different growth catalysts or improved methods for removing Au from the wires following growth.

5.2 Introduction

The results presented in Chapter 4 show that significant photovoltages are obtainable from silicon wire array samples produced by chemical vapor deposition (CVD) from Au catalyst particles.[1] However, in order to achieve significant energy conversion efficiencies, it will be necessary to demonstrate much higher currents and fill factors than those observed in the initial studies. For individual wires, simulations show that radial junction wires should be able to achieve nearly unity quantum efficiency across most of the Si absorption spectrum.[2] Thus the studies presented in this chapter have focused on measuring the *J-E* curves of wires that are significantly longer than those considered in Chapter 4, and on understanding the contributions of the substrate and the surface treatment of the wires on the observed values of V_{oc}, J_{sc}, fill factor, and efficiency.

5.2.1 CVD Grown Silicon Wires

Growth of silicon wire arrays by chemical vapor deposition (CVD) is a promising route to the inexpensive, scalable synthesis of structured silicon devices starting from widely available starting materials. CVD by the vapor-liquid-solid (VLS) method to grow Si wires was pioneered by Wagner and Ellis in the 1960s (Figure 5.1).[3] Since then, many studies have shown the controlled synthesis of silicon wires of many different sizes by using the CVD-VLS mechanism with Au catalyst particles.[4-15] In addition to CVD,

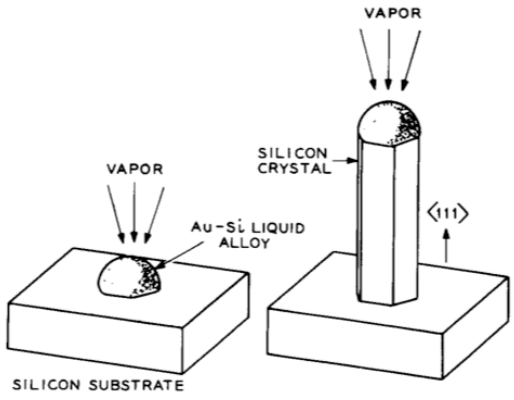

Figure 5.1. *Schematic of the VLS growth mechanism.[3] Si precursor in the gas phase impinges on the catalyst particle, where it is dissolved and then precipitated, growing the Si wire.*

wirelike structures have also been etched into the surface of single-crystalline silicon samples by chemical means,[16-20] but CVD growth does not necessarily consume an expensive single crystalline substrate wafer and is therefore preferable from a cost perspective.

Work in the Atwater and Lewis groups has demonstrated controlled growth of uniform arrays of Si wires starting from either Au or Cu catalyst particles with $SiCl_4$ as the feed gas.[21] Uniform arrays are obtained by patterning the catalyst particles inside an oxide mask to prevent pooling of the metal at the high growth temperatures.[21] In the interest of conserving the expensive substrate Si wafers used during growth, removal of the arrays after embedding in polymers (e.g., polydimethylsiloxane—PDMS) was demonstrated, as was reuse of the underlying substrate following wire removal.[22,23] In addition, single wires grown in this way have been characterized in both 2- and 4-probe geometries to determine their resistivity, and individual wires with axial contacts have been measured as microscale solar cells.[24]

Although other growth catalysts are possible, the wire arrays examined in this study were all catalyzed by Au particles. Au is expected to form a deep level trap in Si,[25] and its equilibrium concentration at the growth temperature is roughly 10^{16} cm^{-3}.[26-28] This expected concentration was confirmed by secondary ion mass spectrometry (SIMS) experiments which showed a concentration in the bulk of about 10^{16} cm^{-3}, but a concentration in the 100 nm closest to the surface of around 10^{17}-10^{18} cm^{-3}.[29] At this bulk Au concentration, for a midgap trap state in n-type Si, the expected minority carrier lifetime in the bulk is given by:[25]

$$\tau_p = \frac{1}{\sigma_p v_{th} N_T} \tag{5.1}$$

where τ_p is the minority carrier lifetime, σ_p is the trap capture cross section, v_{th} is the thermal velocity, and N_T is the concentration of traps. Using the geometric cross section of a Au atom (~10^{-15} cm^2) and the thermal velocity in Si (~10^7 cm s^{-1}) with a concentration of 10^{16} cm^{-3} yields a lifetime of about 10 ns. To convert this to a minority carrier diffusion length, we use the hole diffusion coefficient in Si (~10 cm^2 s^{-1}):[25]

$$L_p = \sqrt{D_p \tau} \tag{5.2}$$

This gives a value of around 3 μm for the minority carrier diffusion length. Using single wire devices, the diffusion length in VLS grown wires was measured by scanning photomicroscopy and found to be around 2-2.5 μm. Thus, the minority carrier diffusion length is expected to be larger than the radius of these wires, so that all photogenerated minority carriers are expected to be collected by the radial junction.[2]

Another important consideration for Au-catalyzed wires is the potential for Au to increase the resistivity of the wires. It was found that increasing the Au concentration significantly above the dopant concentration in n-type Si could lead to an increase in resistivity of many orders of magnitude.[26] In this case, 2- and 4-probe measurements showed the wires to have relatively low resistivity as grown (~0.05 Ω-cm) indicating that no such process is occurring.[24] However, the mechanism of n-type doping is unknown, and early studies of the resistivity of Au-catalyzed wires showed significant batch-to-batch variability in resistivity. Furthermore, the wires used in most of these studies were

grown with higher purity Au catalyst and were typically found to have lower conductivity than those reported in the literature (M. Kelzenberg, personal communication, 2008).

5.2.2 Photoelectrochemistry

As in the preceding chapters, photoelectrochemical characterization of the CVD-grown wire arrays was primarily accomplished using the 1,1'-dimethylferrocene$^{+/0}$/ methanol system ($Me_2Fc^{+/0}$/methanol). This system has been used with great success in the past for characterization of Si as the absorber for solar energy conversion and has been well studied.[30-37] Solar energy conversion efficiencies with single crystalline silicon were in the range of 10-14%,[38-40] and multicrystalline silicon efficiencies exceeded 7%.[41] The surface properties of Si samples immersed in this medium are also known to be favorable, with low SRV values and high barrier heights.[30,42,43] This system is therefore ideal for making high barrier height conformal junctions to the wires grown by the CVD method.

5.2.3 Wire Arrays for Solar Energy

Semiconductor wire arrays have been used in the literature for a number of solar energy conversion endeavors. In particular, there has been significant work on the use of metal oxide wires in a dye-sensitized solar cell (DSSC) configuration,[44-47] although a number of studies have also used metal oxide nanowires as charge collectors in hybrid organic/inorganic solar cells.[48-50] In addition, silicon wires have also been used to change the reflectivity properties of silicon solar cells, in a manner comparable to that discussed in Section 3.2 for porous Si.[51] In these efforts, the semiconductor is not typically acting as the primary absorber, but is only present as a charge collector or as an optical element.

In addition, photoelectrochemical studies similar to those described in this chapter have been carried out on arrays of Si nanowires produced from porous alumina templates, and a significant shift in cyclic voltammetric peaks was observed at these wire arrays, indicating a photovoltage of about 200 mV.[52] Furthermore, a recent study has also explored the use of Si wire arrays produced by etching in a photoelectrochemical cell,[53] and there have been several recent reports of solid state junctions with Si nanowire arrays produced both by CVD-VLS[54,55] and by chemical etching.[56] Thus, there is significant precedent for the use of wire arrays in solar energy conversion, but the challenge remains to show efficient energy conversion *J-E* curves from semiconductor wire arrays used as the absorbing material.

5.3 Experimental

5.3.1 Reagents

Methanol (BakerDry, Baker, Phillipsburg, NJ), 49% (27 M) HF(aq) (Transene, Danvers, MA), and buffered HF(aq) (Transene) were used without further purification. Water (18 MΩ cm resistivity) was obtained from a Barnstead Nanopure system. Lithium perchlorate, $LiClO_4$ (Sigma-Aldrich), was fused under vacuum and stored under an inert atmosphere until use. Dimethylferrocene (Me_2Fc, Sigma-Aldrich) was sublimed at ~45 ºC under vacuum and was stored under an inert atmosphere until use. Dimethylferrocenium tetrafluoroborate (Me_2FcBF_4) was synthesized from Me_2Fc by addition of excess HBF_4 (Alfa Aesar, Ward Hill, MA) in the presence of 0.5 equivalents of benzoquinone (Sigma-Aldrich). The reaction was conducted in an ice-water bath. The

resulting solid was dried under vacuum and stored in an inert atmosphere. Me_2Fc and Me_2FcBF_4 were stored in light-protected bottles.

Silicon (Czochralski, n-type, (100)-oriented, P-doped) for use as the planar electrode in studies employing high [Me_2Fc^+] was obtained from Wacker Siltronic (Munich, Germany, 4-8 Ω cm resistivity). These wafers were 500 ± 25 μm thick, polished on one side, and had measured resistivities between 5 and 7 Ω-cm.

5.3.2 Fabrication of Wire Array Samples and Controls

Degenerately doped N-type Si(111) wafers (0.004 Ω-cm) were thermally oxidized to produce a 285 nm oxide film. These wafers were then coated with S1813 photoresist (Microchem, Newton, MA), exposed to the pattern (square array of 3 μm holes, 7 μm center to center), and developed in MF319 (Microchem). The wafers were then etched for 4 min in buffered-HF improved (Transene), followed by thermal evaporation of 500 nm gold (99.9999%) and lift-off of the photoresist, to leave the catalyst islands separated by an oxide buffer. The samples were then brought into a tube furnace at 1050°C and annealed in H_2 for 20 min at a flow rate of 1000 sccm. The wires were subsequently grown in a mixture of H_2 (1000 sccm) and $SiCl_4$ (20 sccm) in order to produce wires of ~100 μm length (about 30 minutes).

5.3.3 Electrode Preparation and Treatment

Following growth, the wire array samples were etched for 10 s in buffered HF to remove the native oxide. The samples were then soaked for 45 min in TFA solution (Transene), which contains I^-/I_3^-, to etch away the gold particles. SEM images confirmed removal of the bulk of the Au catalyst particle (See Figure 5.3). The wire array samples were subsequently dipped in 1 M HCl(aq) and rinsed with H_2O. The samples were then

etched for 10 s in buffered HF to remove native oxide, rinsed with H_2O, and dried under a stream of N_2. Ga/In was immediately rubbed onto the back of the sample, and the samples were attached to a wire coil using silver paint. The samples were then sealed inside a glass tube, leaving 2-4 mm^2 of exposed front surface area, using Hysol 9460 epoxy (Loctite) to coat the front face and sealing the rest of the sample with Hysol 1C epoxy (Loctite). Hysol 9460 is used on the front face because it does not wick into the wire array to an appreciable extent.

For physical removal of wires from the substrate, the corner of a borosilicate glass slide was used to gently scrape the wires away from the surface, followed by a cotton swab soaked in methanol. Very little force was necessary to remove the wires, and the resulting surface typically regained a reflective sheen. For chemical wire etching, a 30% (w/w) solution of KOH in H_2O was used at room temperature with agitation or stirring. Following each etching step in KOH, the electrodes were rinsed with water/methanol/ acetone/methanol/water and etched again for 10 s in buffered HF to remove any oxide that formed during the etching procedure.

For scanning confocal microscopy studies, the Au catalyst was first removed from a large area wire array as described above. The array was then subsequently etched 10 s in buffered HF to remove the native oxide and affixed to a copper mount using Ga/In eutectic followed by silver paint. The cell for confocal microscopy experiments was then assembled under an inert atmosphere.

5.3.4 Photoelectrochemical Measurements

Under white light, the photoelectrochemical measurements were performed in a solution consisting of 200 mM of 1,1'-dimethylferrocene (Me_2Fc), 0.5 mM of Me_2FcBF_4, and 1 M of $LiClO_4$ in methanol. Methanol was clearly observed to wet the wire array surfaces during both processing and photoelectrochemical measurements. The working electrode was a wire array sample. The counter electrode was a Pt mesh, and the reference electrode was a Pt wire enclosed in a Luggin capillary that contained the same solution as the main cell. All cell components were assembled under an inert atmosphere and were sealed before being placed under positive pressure of Ar. During measurements, the cell was illuminated using a 300 W ELH-type projector bulb with a dichroic rear reflector.[57] The light intensity was calibrated using a Si photodiode to produce a photocurrent equivalent to that obtained under 100 mW cm^{-2} of AM 1.5 illumination at the working electrode surface. For Si photoelectrodes in this same cell configuration and electrolyte/redox system, this calibration method has been shown previously to produce short-circuit photocurrent densities that are very close to those obtained under the same intensity of actual sunlight.[39,40] The solution was stirred vigorously during measurement, and a stream of air was used to keep the cell temperature constant under illumination.

All current density-potential (*J-E*) measurements were recorded using a Solartron model 1287 potentiostat. In a typical experiment, the *J-E* behavior of the electrode was measured at 5 mV s^{-1} in the dark and then under 100 mW cm^{-2} of illumination. The open-circuit voltage, V_{oc}, was measured between each *J-E* measurement. The short-circuit

current density, J_{sc}, was calculated as the average current density for potentials within 10^{-4} V of 0 V versus the Nernstian potential of the cell. The values of V_{oc} and the presented *J-E* behavior are reported with respect to the Nernstian cell potential, which was measured with respect to the reference electrode for each working electrode. The Nernstian potential was typically 10-30 mV positive of the reference electrode potential, due to drift in the composition of the cell solution compared to the composition of the solution in the Luggin capillary. The point of maximum power was calculated as the average of 10 data points, after eliminating the 10 largest measured points (to remove any erroneous spikes). The efficiency and fill factor were calculated by conventional methods.

Photoelectrochemical experiments were also performed with an increased concentration of Me_2Fc^+ present. In this case, the solution consisted of 200 mM Me_2Fc, 50 mM Me_2FcBF_4, and 1 M $LiClO_4$ in methanol. All other procedures were identical to those described above except that monochromatic illumination was used due to the high absorption of Me_2Fc^+ in the visible. In this case, samples were illuminated with a diode laser emitting at 808 nm that had been passed through a diffuser to give uniform light intensity. The laser intensity was set for each measurement by matching the plateau current to the current measured for the same electrode under AM 1.5 in the cell having only 0.5 mM Me_2FcBF_4. In addition to the wire array samples tested, equivalent samples constructed from planar (100) Si samples were also tested with both small and large [Me_2Fc^+].

5.3.5 Correction for Series Resistance and Concentration Overpotential

Corrections for concentration overpotential and series resistance losses were performed according to equations (5.3) and (5.4):[58]

$$\eta_{conc} = \frac{k_B T}{nq}\left\{\ln\left(\frac{J_{l,a}}{-J_{l,c}}\right) - \ln\left(\frac{J_{l,a} - J}{J - J_{l,c}}\right)\right\} \tag{5.3}$$

$$E_{corr} = E_{meas} - iR_S - \eta_{conc} \tag{5.4}$$

where k_B is Boltzmann's constant, T is the absolute temperature, q is the charge on an electron, n is the number of electrons transferred in the redox process (n = 1 for $Me_2Fc^{+/0}$), $J_{l,c}$ and $J_{l,a}$ are the cathodic and anodic limiting current densities, respectively, and R_s is the series resistance. The limiting cathodic and anodic current densities were determined by use of a Pt foil working electrode in the same geometry as the Si working electrode, in contact with the same electrolyte solution, and in the same cell configuration. For experiments in solutions with small [Me_2Fc^+], $J_{l,c}$ and $J_{l,a}$ were found to be -0.1 mA cm^{-2} and 60 mA cm^{-2}, respectively. When large [Me_2Fc^+] was used, $J_{l,c}$ was found to increase to -9.7 mA cm^{-2}. The series resistance was calculated by using equation (5.3) to correct the *J-E* data obtained using the Pt electrode for concentration overpotential losses. The inverse of the slope of the linear portion of the resulting *J-E* data, around 0 V vs the cell potential, was then evaluated to produce a value for R_s. Although the series resistance varied from measurement to measurement, due primarily to small differences in the placement of the Luggin capillary, the value was typically in the range of 130-180 Ω. To minimize the possibility of overcorrection, a value of 100 Ω was chosen as the value of the series resistance used for the low [Me_2Fc^+] conditions.

This value should be an underestimate of the actual series resistance, particularly because the contact resistance and the series resistance of the silicon are not accounted for by the resistance data obtained using the platinum working electrode. Hence, the photoelectrode efficiencies calculated herein are conservative. For the cell with high [Me_2Fc^+], R_s was taken to be 150 Ω because an increased resistance was measured due to the difficulty of placing the Luggin capillary near the working electrode surface in the dark solution. Correction of the observed *J-E* behavior at the Si photoelectrodes for both series resistance and concentration overpotentials thus produced the values of E_{corr} reported herein for each measured potential, E_{meas}. When only one of the concentration overpotential or series resistance losses was corrected for, equation (5.4) was still used, but the appropriate term was dropped.

5.3.6 Diode Quality Factor Measurement

In order to measure the diode quality factor, electrodes were measured at a series of light intensities using the 808 nm diode laser in the cell with high [Me_2Fc^+]. At each light intensity the V_{oc} and the J_{sc} were measured using the Solartron 1287 potentiostat. The V_{oc} is expected to the have the general form:[59]

$$V_{oc} = \frac{AkT}{q} \ln\left(\frac{J_{ph}}{J_0}\right) = \frac{AkT}{q} \ln(J_{ph}) - \frac{AkT}{q} \ln(J_0) \tag{5.5}$$

where A is the diode quality factor, k is Boltzmann's constant, T is the temperature, q is the charge on an electron, J_{ph} is the photocurrent density, and J_0 is the dark saturation current density. Therefore, a plot of V_{oc} vs. J_{ph} should be linear with slope AkT/q, and the value of A can be readily extracted.

5.3.7 Scanning Confocal Microscopy Measurements

For scanning microscopy experiments, a silicon wire was affixed to a copper backing as described above. A flow cell was then assembled using an o-ring with three radial holes and a coverslip. Two of the radial holes allowed the cell to be filled through fluorocarbon turing with 50 mM Me_2Fc, 10 mM Me_2FcBF_4, and 1 M $LiClO_4$ in propylene carbonate under an inert atmosphere. The wire array electrode was connected to the virtual ground of a high-pass filtered transresistence preamplifier circuit. The counter electrode was connected to ground through a DC power supply. The preamplifier output was connected to a lock-in amplifier (Stanford Research), and the signal was measured from the lock-in amplifier output. The lock-in reference was provided by the optical chopper (Thorlabs) used to modulate the excitation beam. The sample was excited with a continuous wave 650 nm diode laser passed through the optical chopper operating at about 1 kHz and finally through a 20x long working distance microscope objective. The focused laser spot was then rastered across the sample and the photocurrent measured at each point as the output of the lock-in amplifier.

5.4 Results and Discussion

5.4.1 Wire Arrays

Vertically aligned arrays of high aspect ratio Si wires were produced by the CVD-VLS method using Au as the VLS catalyst.[21] In order to achieve good pattern fidelity, the substrate wafer is first patterned with an oxide buffer layer before Au deposition, which serves to prevent flow and pooling of the catalyst at the growth temperatures. Growth from wafers patterned in this way produces long, straight wires with the Au catalyst

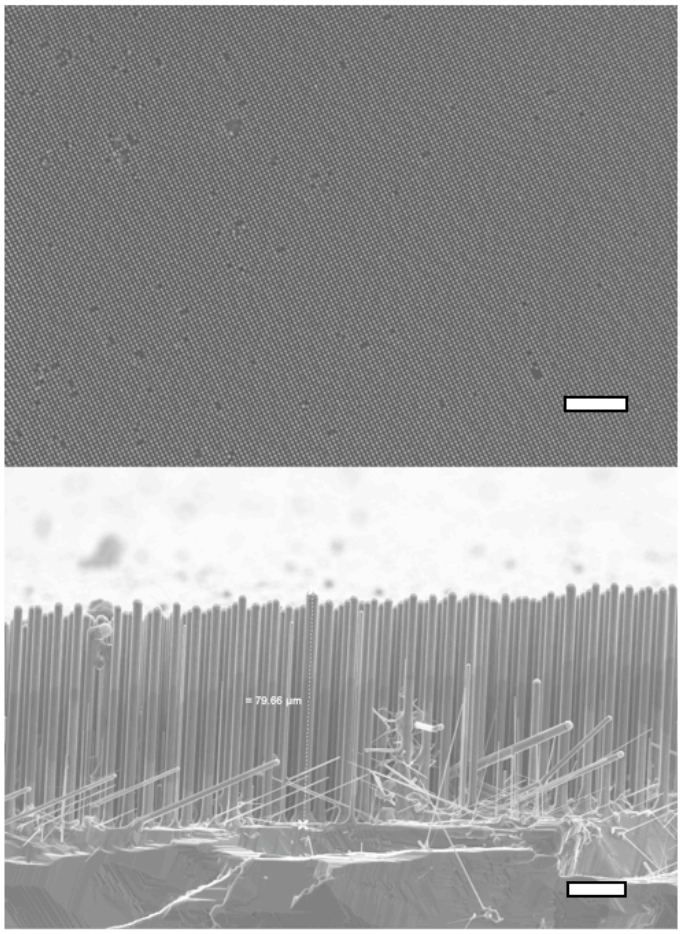

Figure 5.2. *Scanning electron micrographs of Si wire arrays. Top: Plan view showing the long range order in the arrays with some deletion defects. Scale bar, 100 µm. Bottom: Side view of the wires at the edge of the wafer. Some of the non-vertical wires are due to the growth at the sample edges. Scale bar, 20 µm.*

particle still clearly visible on the wire tip. The arrays shown in Figure 5.2 are representative of the samples used to obtain the photoelectrochemical results shown below. From the plan view of the wires, it is apparent that there are a significant number of deletion defects in the arrays, perhaps due to defects in the oxide or catalyst patterns resulting from the photolithography step. However, the cross-sectional image of the wires shows some nonvertical wire growth, and this may be another explanation for the observed defect density. It has been previously shown that wires produced under these conditions grow in the <111> direction,[21] and the angle between adjacent <111> vectors

is around 70º, which is approximately the angle observed between the vertically growing wires and those that grow at an angle. Thus, it is expected that the non-vertical wires are still growing in the <111> direction, but have developed a kink early in their growth.

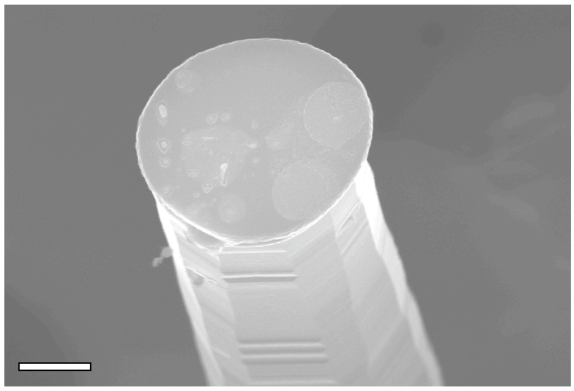

Figure 5.3. *Close up of the wire tip after removal of the catalyst particle. Note that the tip is flat and that the wire shows significant faceting. Scale bar 1 µm.*

The wires used in this study varied from ~80 to ~100 µm in length and typically had diameters of around 2-2.5 µm. This diameter is slightly smaller than the 3 µm diameter of the patterned catalyst particle, which is consistent with the significant taper typically observed at the very base of the wires. Following this initial taper, however, the wires grow with straight side walls, indicating that the catalyst particle does not shrink at a significant rate after growth initiation. Removal of the catalyst particle from the wires was accomplished using a proprietary etching solution containing I^-/I_3^-. Complete removal of the catalyst particles could be accomplished with this treatment, leaving a flat Si surface at the tips of the wires (Figure 5.3), although in some cases a thin, hollow shell of silicide was observed (not shown). The facets observed in Figure 5.3 are typically observed in the wires upon closer inspection, particularly following a short etch in KOH solution, which is an anisotropic etchant for Si.

5.4.2 Photoelectrochemical Performance

Photoelectrochemical measurements of wire array electrodes were carried out in a solution consisting of 1.0 M $LiClO_4$, 200 mM Me_2Fc, and ~0.5 mM Me_2FcBF_4 in methanol. This solution has been shown previously to give low surface recombination velocities and high open circuit potentials in contact with n-type Si.[30,42] Figure 5.4 shows representative *J-E* curves of wire array samples. Also shown in Figure 5.4 is the *J-E* characteristic of the substrate after the wires have been mechanically removed. We note that the J_{sc} is reduced by roughly one order of magnitude upon removal of the wires, indicating that the primary contribution to the photoactivity of the samples measured is due to the CVD-grown Si wires rather than the single crystalline Si substrate. This reduction in both photocurrent and photovoltage upon wire removal is consistently

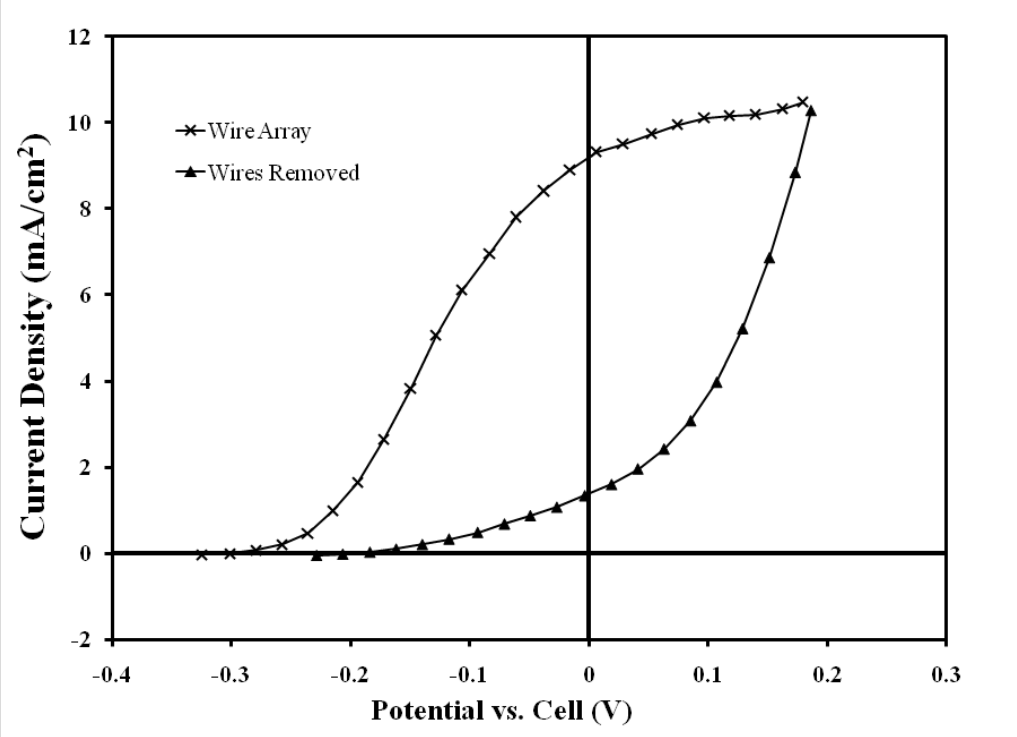

Figure 5.4. *Representative J-E curves for wire array electrodes and electrodes with the wires removed. The data is referenced to the Nernstian potential of the cell, and the scan rate was 5 mV/s.*

observed. This result is expected because the substrate wafer is heavily doped n^+-Si, which should therefore be nonphotoactive. Furthermore, the wire array growth is carried out in the presence of significant concentrations of Au, which has a relatively large diffusion coefficient at the growth temperatures employed (~10^{-6} cm^2 s^{-1} at 1050ºC).[27,28] Thus, we expect the contribution of the substrate to the observed photocurrent to be relatively minor and the remainder of this chapter will focus primarily on the behavior of the Si wires. For further evidence of the photoactivity of the wires over the substrate, see Section 5.4.5.

From the raw *J-E* curves, several features are immediately apparent. First, we note that the observed short circuit current density (~9 mA/cm^2) is significantly larger than the expected value based on the filling fraction of wires. Since the wires are patterned in a square array with 7 μm center-center distance and typically have diameters on the order of 2.5 μm, the filling fraction of Si in the wire layer is only about 10%. Given that the flux of incident energy in the AM 1.5 spectrum above the Si band gap gives rise to a maximum theoretical J_{sc} of ~43 mA/cm^2,[60] the 10% filling fraction of wires predicts a maximum observable J_{sc} of only 4.3 mA/cm^2. One possible explanation is that the lamp used is not exactly the same as AM 1.5, giving rise to artificially high photocurrents in Si. However, the results of Section 2.4.2 show that planar samples under the same illumination in the same cell show photocurrents of around 35 mA/cm^2, well less then the theoretical maximum.[61] Thus, the high J_{sc} implies significant light scattering within the wire array layer, leading to absorption of more light than just that incident directly on the tops of the wires. The optical absorption and scattering properties of the wire arrays have

been verified using arrays that have been embedded in polydimethylsiloxane (PDMS) and removed from the subsrate. Under these conditions, it was found that the wire array absorption was 2-3 times what would be expected from the simple filling fraction of the wires in the polymer (M. Kelzenberg, personal communication, 2008). Although the scattering in the Si wire/methanol system is expected to differ from that observed in the Si wire/PDMS system, the precedent for significant scattering based absorption of the wires, even at normal incidence, lends credence to the hypothesis that the observed values of J_{sc} are due primarily to the scattering of light.

In addition to the high currents observed from the raw data, the cathodic limiting current is also found to be very small (usually ~0.1 mA/cm^2). This is due to the much smaller concentration of Me_2FcBF_4 used in the cell as compared to the concentration of Me_2Fc. It is necessary to use only small amounts of Me_2Fc^+ when illuminating with white light because Me_2Fc^+ absorbs strongly in the visible, interfering with the penetration of light to the electrode surface. As discussed in Section 1.4.1, the small cathodic limiting current leads to a significant concentration overpotential loss, resulting in a significant reduction in fill factor. When the *J-E* curves are corrected for the concentration overpotential loss as described in the Section 5.3.5, the fill factor is noticeably improved (Figure 5.5). The anodic and cathodic limiting currents needed for the correction were obtained by measuring the *J-E* curve of a Pt electrode in the same cell and geometry as that used to measure the Si electrodes. The observed value of J_{sc} is also improved upon correction in these samples because the curves had not reached the plateau current before reaching short circuit due to the large potential shift from the

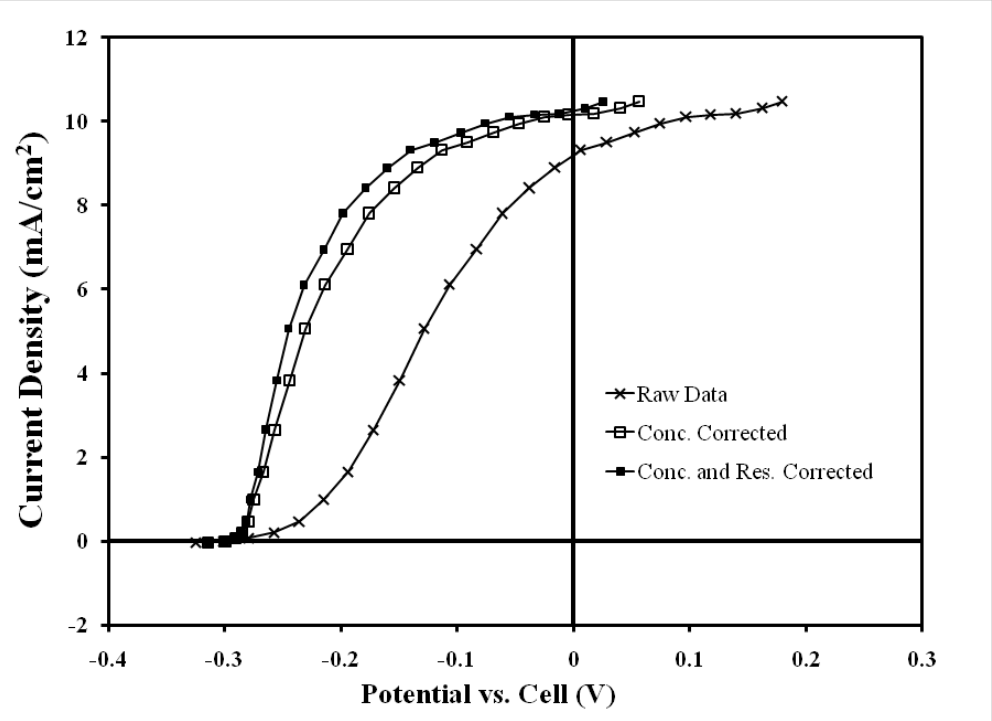

Figure 5.5. *Representative J-E curves for wire array electrodes after correction for concentration overpotential losses (Conc. Corrected) and both concentration overpotential and series resistance losses (Conc. and Res. Corrected).*

concentration overpotential loss. In addition to concentration overpotential loss, we also expect resistance losses due to the nonaqueous electrolyte. Even when using a Luggin capillary to reduce it, the solution series resistance is measured to be in excess of 100 Ω when using a Pt foil electrode in place of the Si working electrode. Further correction of the *J-E* curve for this series resistance leads to only a slight improvement in fill factor (Figure 5.5).

The observations made above by qualitatively examining representative *J-E* curves from wire array samples are supported quantitatively by the solar cell figures of merit observed for a set of wire array electrodes measured under the same conditions (Table 5.1). It is apparent from the change in fill factor that the contribution of the concentration overpotential loss is significantly larger than that of the solution series resistance loss.

Table 5.1. *Solar cell figures of merit for wire array electrodes grown from Au catalyst*

Data Correction[a]	J_{sc} (mA cm^{-2})[b]	V_{oc} (mV)[b]	Fill Factor (%)[b]	Efficiency (%)[b]
None	9.8 ± 0.4	262 ± 9	21 ± 1	0.55 ± 0.05
Conc. Only	11.7 ± 0.5	262 ± 9	44 ± 1	1.35 ± 0.08
Conc. and Res.	11.9 ± 0.5	262 ± 9	50 ± 2	1.56 ± 0.10

[a] Conc. Only indicates that only the concentration overpotential correction has been made, while Conc. and Res. indicate values extracted from J-E curves corrected for both concentration overpotential and series resistance.
[b] All values are the mean of eight independent samples, with the error given as the standard error of the mean.

Comparing these figures of merit with those found in Chapter 4,[1] we see that, while the J_{sc} has improved by nearly an order of magnitude, the V_{oc} has decreased by around 100 mV. The improvement in J_{sc} can be explained by several key changes from the samples examined in Chapter 4. First, it was stated in Chapter 4 that the wires were on the order of 20 μm in length, whereas the wires in this study are typically around 80-100 μm long. Furthermore, the epoxy used to encapsulate the samples examined in Chapter 4 was subsequently found to infiltrate the wire arrays to a significant extent, leaving only the tips of the wires exposed to solution. Since the wires generated are expected to have minority carrier diffusion lengths on the order of 2 μm,[24] leaving only the tips of the wires exposed will significantly reduce the collected current. Finally, the epoxy infiltrating the arrays in the samples from Chapter 4 was opaque, preventing the enhanced absorption due to scattering of light within the wire arrays. Thus, the wires in this study show much higher J_{sc} values because they are longer, have conformal contact along the full length of the wire, and have the possibility of enhanced absorption due to scattering.

We would also like to understand the observed V_{oc}, both in comparison with an ideal planar diode and in comparison to the results obtained in Chapter 4. In order to

understand the influence of geometrical affects on the observed V_{oc}, we can calculate the expected reduction in V_{oc} based on the increased surface area of the wires relative to a planar diode, given by (See Section 1.3.1):

$$V_{oc} = \frac{AkT}{q} \ln\left(\frac{I_{ph}}{\gamma I_0}\right) \tag{5.6}$$

From equation (5.6), it is apparent that the value of the diode quality factor, A, can be determined from the slope of a plot of V_{oc} vs. ln(I_{ph}). Performing this measurement gives an average value for the diode quality factor for the wire array samples examined here of ~1.6 (mean of 6 samples). We note that the observed diode quality factor for the wire arrays is significantly larger than 1, and that values of approximately 1.1 are obtained with photoactive planar samples under the same conditions. In all cases the plot of V_{oc} vs. ln(I_{ph}) was found to be linear with $R^2 > 0.999$. Thus, other recombination mechanisms besides bulk recombination ($A = 1$) are likely to be active in these devices, particularly depletion region recombination, which gives an expected diode quality factor of 2.[59] The simulations performed by Kayes et al. showed that depletion region recombination becomes quite important for devices with highly structured junctions,[2] so we expect to see significant contributions from depletion region recombination in these samples.

We calculate γ for equation (5.6) by assuming that all of the current collected is collected through the wire surface, not through the substrate (which is protected by a thick layer of oxide). In this case, we have:

$$\gamma = \frac{\text{wire surface area}}{\text{projected area}} \tag{5.7}$$

Therefore, we can easily calculate γ by taking the ratio of the wire surface area in one wire to the projected area of one unit cell. For 100 μm long wires with 2.5 μm diameter and 7 μm center-center distance in a square array, this gives $\gamma \approx 16$. Thus, we calculate a reduction in V_{oc} of only about 117 mV due to the increased junction area relative to a planar device. This value cannot account entirely for the poor V_{oc} measured for the wire arrays, and it suggests that the high concentration of Au in these wires is leading to a much reduced V_{oc} value due to recombination in the bulk and depletion regions in addition to the reduction from increasing γ.

Since the wires examined in Chapter 4 were also grown by Au-catalyzed CVD-VLS, we can compare the V_{oc} obtained in this study (262 mV) with the V_{oc} measured for those samples (389 mV).[1] As with the observed change in J_{sc}, geometrical concerns are again expected to play a significant role. For the shorter wires from Chapter 4, the decreased junction area relative to the projected area is expected to lead to an increased V_{oc} relative to the wire arrays examined here. Furthermore, we expect that carriers were collected primarily at the wire tips in the samples examined in Chapter 4 due to epoxy infiltration, thus further reducing the junction area and increasing the V_{oc} relative to the samples examined in this chapter. These effects combined lead to an increase in the effective surface area enhancement factor, γ, for the wires examined in this chapter relative to those studied in Chapter 4.

Assuming that the wires examined in Chapter 4 have a similar diode quality factor (~1.6), and taking into account the difference in photocurrents, it is possible to calculate the increase in γ that would be needed in order to account for the observed decrease in

V_{oc}. Based on this calculation, an increase in γ of more than a factor of 100 would been needed to fully explain the observed decrease in V_{oc}. Although γ is only ~16 for the long wires examined in this chapter, it is likely that the wires studied in Chapter 4 have an effective γ that is less than unity based on equation (5.7) because only a few microns of wire tip were exposed through the epoxy. Assuming 2 μm of wire were exposed in the samples from Chapter 4 gives a γ value of 0.42 for those wires, and thus a relative increase in γ by a factor of about 40 for the long wires considered here relative to the short, unintentionally encapsulated wires considered in Chapter 4. Although there is significant uncertainty in these calculations, they suggest that changes in γ due to geometrical changes cannot fully explain the observed decrease in V_{oc}. As another possible contributor to the change in V_{oc}, we expect to observe significant depletion region recombination in the long wires examined in this chapter, but much less in the wires examined in Chapter 4 since only the tips of the wires were exposed. This may lead to a smaller diode quality factor for the wires from Chapter 4, further enhancing the observed decrease in V_{oc}. Although a significant portion of the change in V_{oc} can be accounted for by geometrical effects, there may be significant differences in materials properties or doping levels giving rise to the observed difference in V_{oc}.

Finally, we note that the observed fill factor improves significantly upon correction for the concentration overpotential losses, leading to much improved efficiencies. These devices, although still not efficient enough for commercial use, are much more efficient than the devices studied in Chapter 4, largely due to the changes in geometry described above. Since the concentration overpotential has such a dramatic effect on the observed

fill factor and efficiency, further experiments were undertaken in order to verify that the fill factor and efficiency of the electrodes improve experimentally under relaxed concentration overpotential constraints.

5.4.3 Experimental Verification of *J-E* Curve Correction

In order to further probe the influence of the concentration overpotential loss, *J-E* curves were collected under conditions with an increased concentration of Me_2Fc^+ (50 mM instead of ~0.5 mM). Since the oxidized half of the redox couple absorbs strongly in the visible, it is necessary to use illumination of a wavelength where Me_2Fc^+ does not absorb strongly when using an appreciable concentration of Me_2Fc^+. Thus, for these experiments, the samples were illuminated with a diode laser emitting at around 808 nm. The laser intensity was set so that the plateau current under monochromatic illumination in high [Me_2Fc^+] was approximately equal to that observed under white light for the same electrode in the cell containing only ~0.5 mM Me_2Fc^+. Figure 5.6 shows representative *J-E* curves taken with high Me_2Fc^+ with various applied corrections for both planar (photoactive) and wire array samples. The photoactive planar samples have been included to demonstrate that the observed effect is not due to the wire array geometry. It is apparent from these plots that the corrections for both series resistance and concentration overpotential losses are much smaller under these conditions.

Representative *J-E* curves comparing small (~0.5 mM) and large (50 mM) [Me_2Fc^+] conditions for both planar and wire array samples are shown in Figure 5.7. For both planar and wire array samples, the improvement in the fill factor at the same J_{sc} and V_{oc} are clearly visible in the raw data. This is a direct manifestation of the concentration

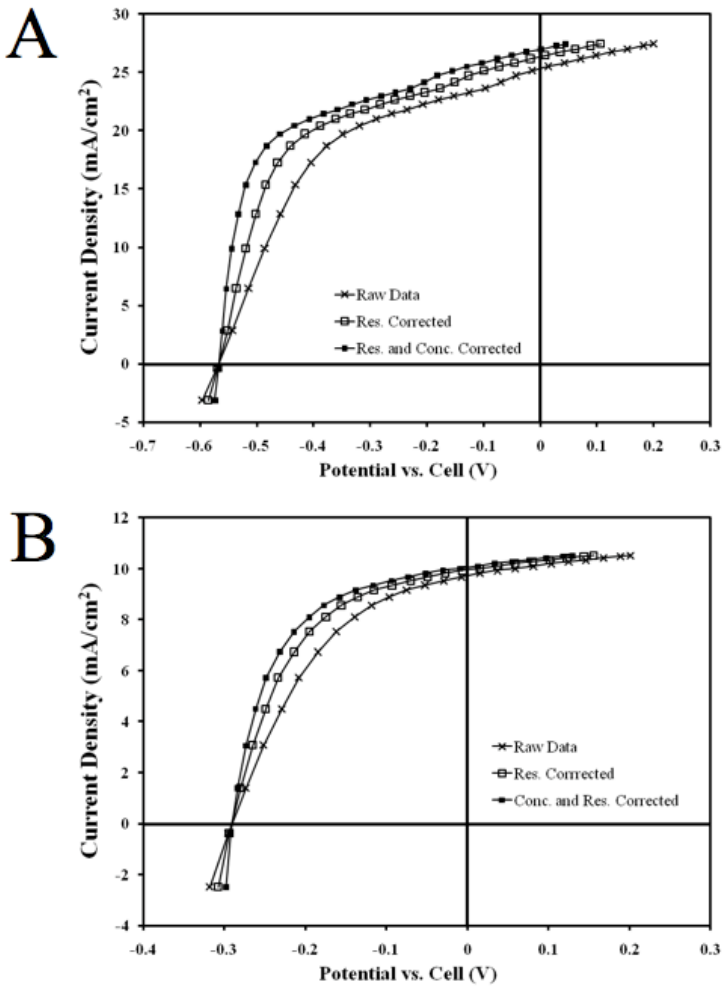

Figure 5.6. *Representative J-E curves collected with 200 mM Me_2Fc, 50 mM Me_2Fc^+, and 1.0 M $LiClO_4$ in methanol. Illumination was provided by an 808 nm diode laser with the intensity set to match the plateau current under AM 1.5 illumination. The scan rate was 5 mV/s. A) Planar, (100) sample corrected for resistance (Res.) or both resistance and concentration overpotential losses (Conc. and Res.). B) Wire array electrode.*

overpotential loss observed when the concentration of Me_2Fc^+ is much smaller. When monochromatic illumination was used in the cell with small [Me_2Fc^+], the *J-E* curves matched those obtained with white light when the laser intensity was adjusted to match the plateau currents (data not shown). Thus, the observed increase in fill factor is not due to the use of monochromatic illumination instead of white light and is a direct manifestation of the increased concentration of Me_2Fc^+.

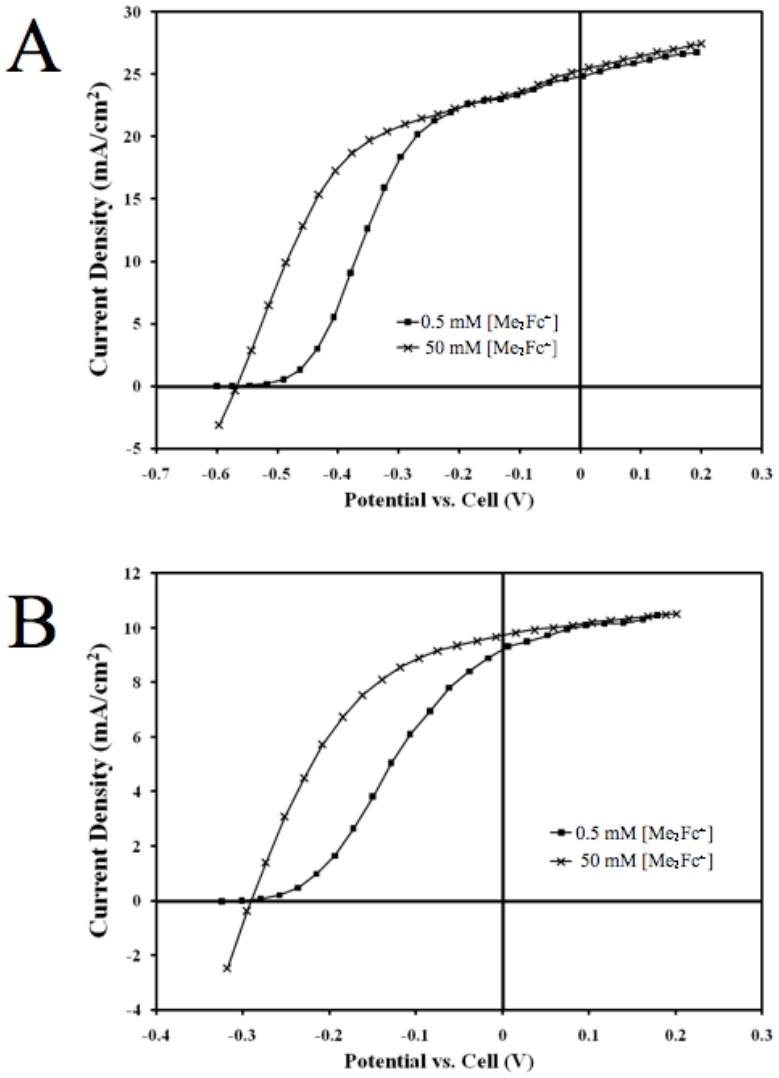

Figure 5.7. *Representative J-E curves comparing response in small [Me_2Fc+] and large [Me^2Fc+]. Samples were under AM 1.5 white light with small [Me_2Fc^+] or under 808 nm light with large [Me_2Fc^+], with the intensity set to match the plateau current at AM 1.5. A) Planar (100) Si sample. B) Wire array sample.*

Figure 5.8 (A and B) shows data collected with both small and large [Me_2Fc^+] when the concentration overpotential correction has been applied. The concentration overpotential corrected data from small [Me_2Fc^+] matches the raw data from large [Me_2Fc^+], as expected. However, even in the presence of 50 mM Me_2Fc^+, there is still a small but significant concentration overpotential loss. After making this correction to the 50 mM Me_2Fc^+ data, we see slightly better agreement between the two conditions for

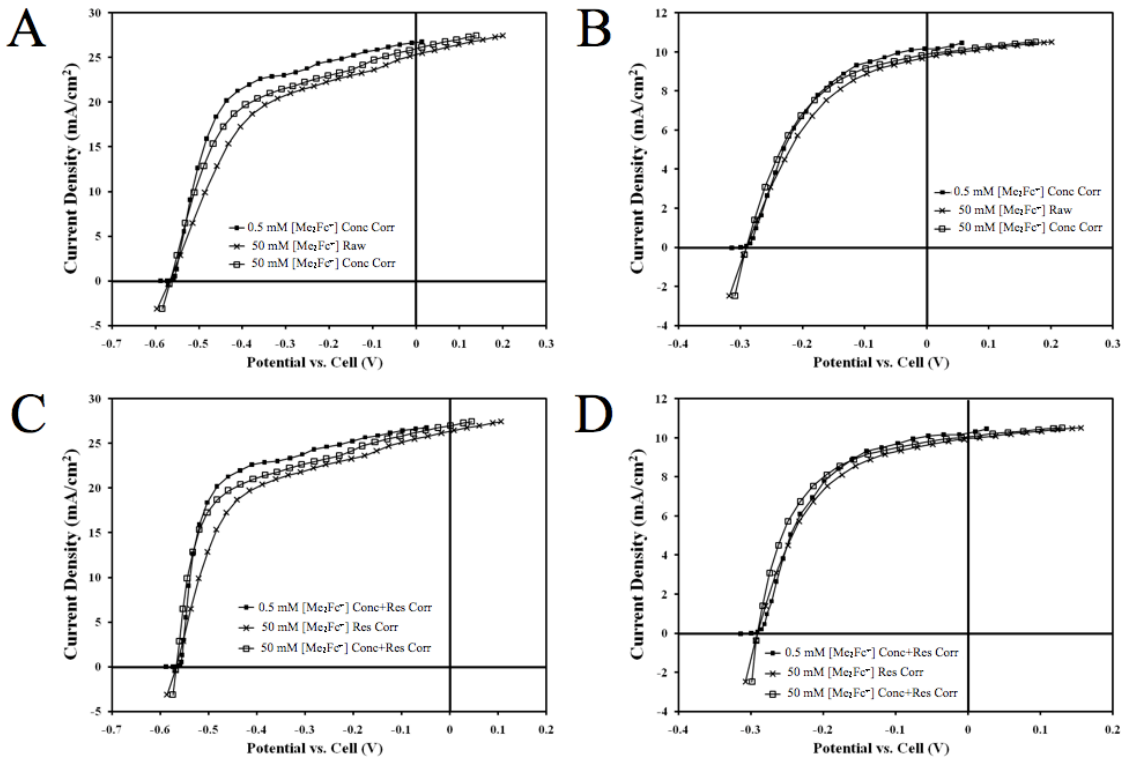

Figure 5.8. *Representative J-E curves with various corrections. As before, white light (AM 1.5) was used for 0.5 mM Me_2Fc^+, and 808 nm light was used for 50 mM Me_2Fc^+. A) Planar (100) samples, no resistance correction. B) Wire array samples, no resistance correction. C) Planar (100) samples, resistance corrected. D) Wire array samples, resistance corrected.*

both planar and wire array samples. This agreement is further evidence in support of the validity of the concentration overpotential correction.

The data shown in Figure 5.8 (C and D) have been corrected for series resistance losses. We also expect to observe agreement between *J-E* curves collected with large [Me_2Fc^+] that have been corrected for series resistance and *J-E* curves collected with small [Me_2Fc^+] that have been corrected for both concentration overpotential and series resistance losses. Figure 5.8 (C and D) supports this hypothesis, although a small correction for the remaining concentration overpotential loss with large [Me_2Fc^+] slightly improves the agreement in the planar case. Taken together, these data suggest that the

theoretically predicted correction for the concentration overpotential loss corresponds closely to the physical reality of the system.

The qualitative observations made above based on the representative *J-E* curves are corroborated by solar cell figures of merit obtained for a number of independent wire array electrodes (Table 5.2). As expected, the value of J_{sc} was approximately the same for all conditions and corrections with the exception of the raw data obtained with small [Me_2Fc^+]. In the latter case, many of the wire array samples had not reached the plateau current before short circuit due to large concentration overpotential losses. Neither the concentration overpotential correction nor the resistance loss correction affects the value of V_{oc}, so the only observed difference is between small [Me_2Fc^+] and large [Me_2Fc^+]. Although a slight drop in the average V_{oc} is observed upon changing to monochromatic illumination, this difference is not statistically significant. If there is a real difference in the V_{oc}, it could be due to the use of red light instead of white light, giving rise to more

Table 5.2. *Solar cell figures of merit for wire array samples measured with small and large [Me_2Fc^+]*

[Me_2Fc^+]	Data Correction[a]	J_{sc} (mA cm^{-2})[b]	V_{oc} (mV)[b]	Fill Factor (%)[b]
~0.5 mM	None	9.8 ± 0.6	254 ± 9	20 ± 1
~0.5 mM	Conc. Only	11.9 ± 0.6	254 ± 9	44 ± 2
~0.5 mM	Conc. and Res.	12.2 ± 0.7	254 ± 9	50 ± 2
50 mM	None	11.4 ± 0.7	249 ± 9	41 ± 1
50 mM	Res. Only	11.8 ± 0.8	249 ± 9	49 ± 1
50 mM	Conc. Only	11.7 ± 0.7	249 ± 9	46 ± 1
50 mM	Conc. and Res.	12.0 ± 0.8	249 ± 9	55 ± 1

[a] Samples have been corrected for concentration overpotential (Conc.) and solution series resistance (Res.) as indicated.
[b] Values reported are the mean of six independent electrodes and error values are the standard error of the mean.

uniform carrier generation in the wires and therefore more uniform flux across the junction (See Section 3.4.3), but the effect is very small in this case.

The most important parameter listed in Table 5.2 is the fill factor. We see that the fill factor is quite low for the raw data collected in small [Me_2Fc^+], but at least a factor of two higher for all the other entries in the table. In particular, we note that the fill factor for uncorrected data collected in large [Me_2Fc^+] is similar to the fill factor obtained when the data collected in small [Me_2Fc^+] is corrected only for concentration overpotential. As described above, correcting the data with large [Me_2Fc^+] for the remaining concentration overpotential loss under those conditions further improves the observed agreement with the concentration overpotential corrected small [Me_2Fc^+] data. Similarly, correcting the large [Me_2Fc^+] data for only series resistance losses gives a fill factor that is very similar to that obtained when the data collected with small [Me_2Fc^+] is corrected for both series resistance and concentration overpotential losses. Taken together, these data provide strong evidence that the concentration overpotential correction undertaken for small [Me_2Fc^+] is valid for this cell. Therefore, these experiments also validate the relatively high efficiencies obtained from the corrected data, implying that production of a cell that mitigates both concentration overpotential and series resistance losses would yield efficiencies on the order of 1.5% for these wire arrays.

5.4.4 Preliminary Wire Surface Removal Results

Impurity profiling experiments on wires grown by CVD-VLS from Au catalyst particles have shown that there is a Au rich layer near the surface of the wires.[29] As a result, etching of the wire surface using KOH was undertaken to explore the possibility of

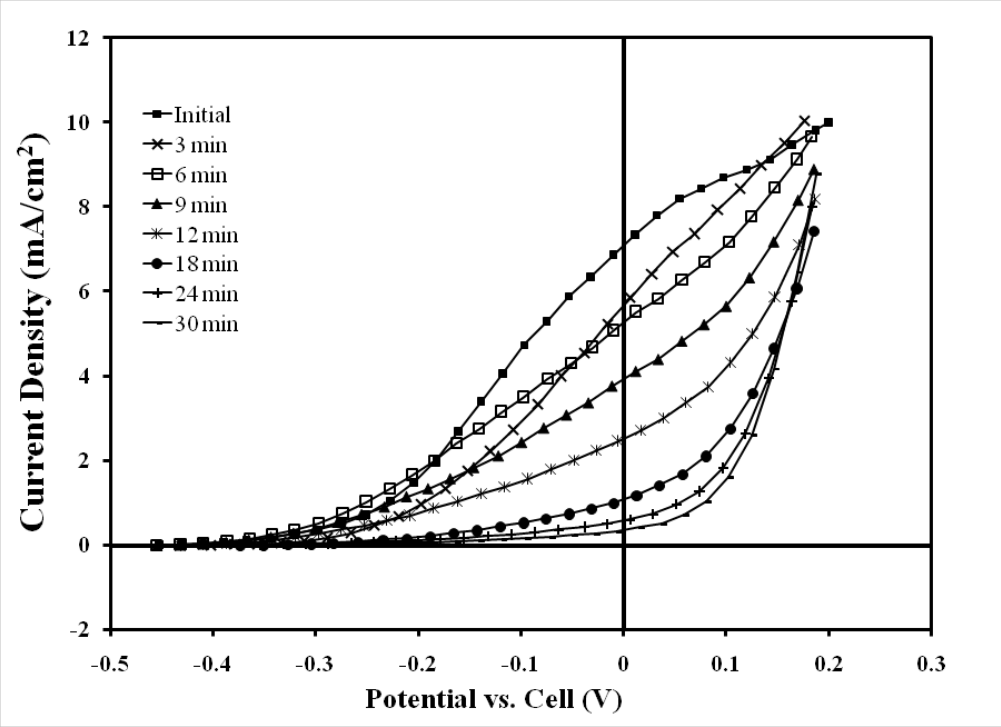

Figure 5.9. *J-E curves under AM 1.5 illumination in 200 mM Me_2Fc, 0.5 mM Me_2FcBF_4, and 1.0 M $LiClO_4$ in methanol. The scan rate was 5 mV/s. Etching was conducted in 30% KOH in water (w/w), and etch times are indicated in the legend.*

improving the wire performance by removing the near-surface Au rich layer. Figure 5.9 shows representative *J-E* curves for the etching of one wire array sample. Under the conditions used in this experiment, 3 min of etching in KOH should correspond to the removal of approximately 100 nm of Si from all exposed surfaces, or about a 200 nm reduction in diameter for each 3 minutes of etching.[62] It is apparent from Figure 5.9 that the primary effect of KOH etching is the reduction of J_{sc}. After etching for 30 min, it is expected that about 2 μm of wire diameter have been removed, corresponding to approximately the entire wire. Indeed, after 30 min of etching there is very little remaining photoresponse from the wire arrays. This observation further corroborates that the n^+-Si substrate is not photoactive following the growth procedure and that the *J-E* curves collected primarily reflect the photoactivity of the wires rather than the substrate.

The results shown in Figure 5.9 have been observed with other wire array samples as well, but these results are still preliminary due to complications arising from conformal deposition during the wire growth process. In some samples, conformally deposited Si (visible by SEM, data not shown) shows significant photoactivity even after all the wires have been removed. Thus, more detailed exploration of the influence of KOH etching on the photoelectrochemical properties of wire arrays will require samples known to have little or no conformally deposited Si at the base of the wires. Despite their preliminary nature, these results suggest that further improvements in the Si wire array performance at the same geometry will require changing to a different VLS catalyst that has a less deleterious effect on Si or devising an efficient gettering system to increase the purity of the wires produced.

5.4.5 Scanning Confocal Microscopy of Wire Arrays

It was shown above by both mechanical wire removal and chemical wire removal that that the n^+-Si substrate is not photoactive following wire growth. In order to provide more support for the dominance of the wires in the observed photoelectrochemical responses, scanning confocal microscopy experiments were undertaken to differentiate photoresponse from the wires and from the substrate. In brief, a long working distance confocal microscope objective was used to focus monochromatic light (650 nm) through a coverslip onto a liquid junction cell containing a wire array sample (Figure 5.10). In this case, the solvent used was propylene carbonate due to its lower vapor pressure, and a slightly higher concentration of Me_2FcBF_4 (10 mM) was used. A Pt wire was used as both the counter electrode and a pseudoreference. The focused laser spot was scanned

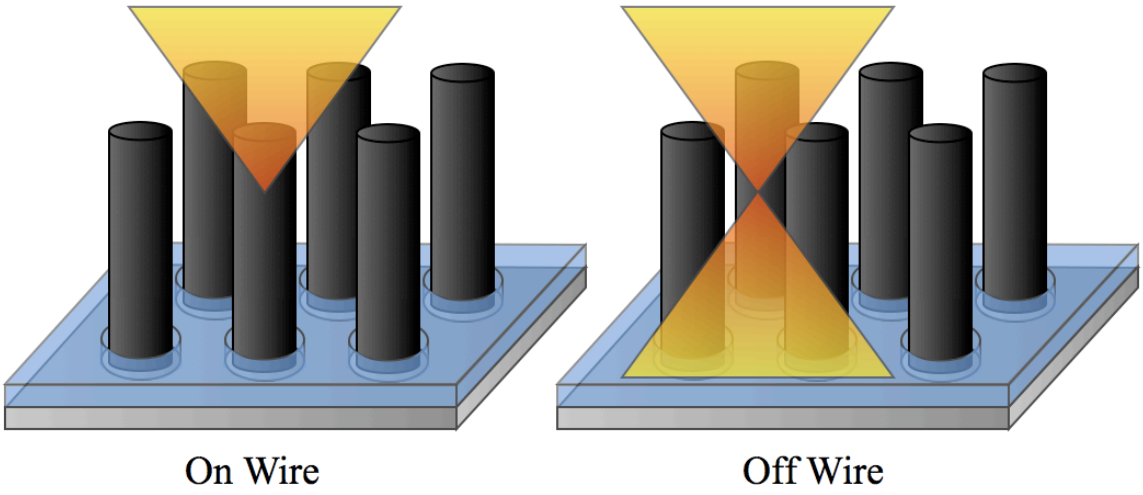

Figure 5.10. *Schematic of scanning confocal microscopy experiments. Si wires are shown growing vertically from the substrate through a thin oxide layer. When the focal point of the incident light is focused on a wire, most of the light should be absorbed by that wire. However, when the focal point is between wires, the defocused beam may intersect many neighboring wires, producing significant absorption.*

across the sample and the photocurrent was measured at each point with a chopper and a lock-in amplifier. In this way, an image can be constructed, with each pixel false colored to represent the measured photocurrent.

Figure 5.11 shows a false-color map of the photocurrent after scanning a wire array sample. The positions of the wires in the image are readily apparent as areas of increased photocurrent. Furthermore, the center-center distance between bright areas is commensurate with the value expected from the mask used, and the bright areas are arranged in a square array. Note, however that the wire diameter as measured by SEM is much smaller than that observed in the scanning microscopy experiments. As suggested by Figure 5.10, because of the tight focus of the laser spot from a confocal objective, it is likely that the beam broadens significantly both above and below the focal plane. Thus, even when the laser spot is not focused directly on a wire, there is expected to be significant absorption by nearby wires due to spreading of the beam. This also accounts

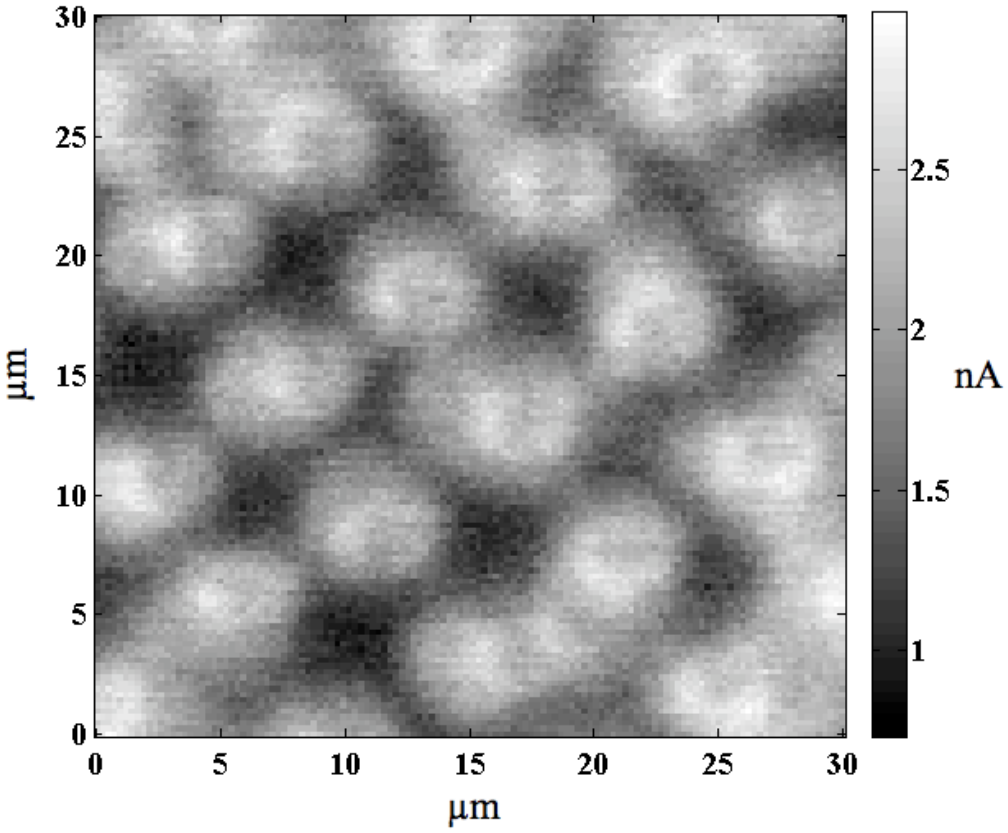

Figure 5.11. *False-color map of a wire array sample. The current scale is shown in nA, and the pixel positions have been scaled to match the approximate real distance traversed during the scan.*

for the significant photocurrent observed even in the darkest areas between rods (~0.75 nA). Thus, although the wires are clearly visible and more photoactive than the substrate, it is difficult to remove contributions from neighboring wires to see only the substrate. However, combined with measurements of the substrate following mechanical or chemical removal of wire arrays, these data strongly support that the observed photoelectrochemical properties described above are attributable to the CVD-grown Si wires rather than to the single crystalline substrate.

5.5 Conclusions

The Au-catalyzed, CVD-grown Si wire arrays examined in these studies show significantly improved efficiencies as compared with those presented in Chapter 4. In particular, the J_{sc} values were nearly an order of magnitude larger than those initially observed, and the fill factor values were improved as well. However, the observed V_{oc} was decreased relative to that observed in Chapter 4, possibly due to the same geometric factors that lead to an increased value of J_{sc}. However, there are likely to be other contributing factors to the lowered V_{oc}, such as changes in materials properties and doping levels. Despite decreases in V_{oc}, even the raw data collected in this study shows much improved efficiency as compared to the previously examined wire array samples. Correction of the raw data for concentration overpotential and solution series resistance losses further improves the fill factor, J_{sc}, and efficiency of these devices. In order to verify the validity of these corrections, extensive studies were performed using photoelectrochemical cells having an increased [Me_2Fc^+]. These studies showed that the concentration overpotential correction calculated from the measured limiting currents correctly accounts for the experimentally observed improvement when moving to a system that is not as limited by mass transport. Therefore, the reported efficiency of about 1.5% is expected to reflect the performance that these wire arrays would exhibit in a system in which both concentration overpotential and series resistance losses have been minimized (e.g., a thin layer cell). Attempts to improve the energy conversion efficiency of the wires by removing the outer, Au-rich layer have so far yielded only decreases in wire performance, indicating that further steps will need to be taken to replace Au as the

VLS catalyst or to remove it from the wires after growth. Finally, the negligible contribution of the n^+-Si substrate to the observed photoelectrochemical behavior has been demonstrated by removal of the wires both chemically and mechanically as well as by scanning confocal microscopy experiments.

5.6 References

1. Maiolo, J. R.; Kayes, B. M.; Filler, M. A.; Putnam, M. C.; Kelzenberg, M. D.; Atwater, H. A.; Lewis, N. S. *J. Am. Chem. Soc.* **2007**, *129*, 12346-12347.
2. Kayes, B. M.; Atwater, H. A.; Lewis, N. S. *J. Appl. Phys.* **2005**, *97*, 114302.
3. Wagner, R. S.; Ellis, W. C. *Transactions of the Metallurgical Society of Aime* **1965**, *233*, 1053-&.
4. Wu, Y.; Cui, Y.; Huynh, L.; Barrelet, C. J.; Bell, D. C.; Lieber, C. M. *Nano Lett.* **2004**, *4*, 433-436.
5. Cui, Y.; Lauhon, L. J.; Gudiksen, M. S.; Wang, J. F.; Lieber, C. M. *Appl. Phys. Lett.* **2001**, *78*, 2214-2216.
6. Lombardi, I.; Hochbaum, A. I.; Yang, P.; Carraro, C.; Maboudian, R. *Chem. Mat.* **2006**, *18*, 988-991.
7. Hochbaum, A. I.; Fan, R.; He, R. R.; Yang, P. D. *Nano Lett.* **2005**, *5*, 457-460.
8. Law, M.; Goldberger, J.; Yang, P. D. *Annual Review of Materials Research* **2004**, *34*, 83-122.
9. Wu, Y. Y.; Yang, P. D. *J. Am. Chem. Soc.* **2001**, *123*, 3165-3166.
10. Hannon, J. B.; Kodambaka, S.; Ross, F. M.; Tromp, R. M. *Nature* **2006**, *440*, 69-71.
11. Kodambaka, S.; Hannon, J. B.; Tromp, R. M.; Ross, F. M. *Nano Lett.* **2006**, *6*, 1292-1296.
12. Kodambaka, S.; Tersoff, J.; Reuter, M. C.; Ross, F. M. *Phys. Rev. Lett.* **2006**, *96*.
13. Lew, K. K.; Pan, L.; Bogart, T. E.; Dilts, S. M.; Dickey, E. C.; Redwing, J. M.; Wang, Y. F.; Cabassi, M.; Mayer, T. S.; Novak, S. W. *Appl. Phys. Lett.* **2004**, *85*, 3101-3103.
14. Lew, K. K.; Reuther, C.; Carim, A. H.; Redwing, J. M.; Martin, B. R. *J. Vac. Sci. Technol. B* **2002**, *20*, 389-392.
15. Wang, Y. F.; Lew, K. K.; Ho, T. T.; Pan, L.; Novak, S. W.; Dickey, E. C.; Redwing, J. M.; Mayer, T. S. *Nano Lett.* **2005**, *5*, 2139-2143.
16. Fang, H.; Wu, Y.; Zhao, J.; Zhu, J. *Nanotechnology (UK)* **2006**, 3768-3768.
17. Huang, Z. P.; Fang, H.; Zhu, J. *Adv. Mater.* **2007**, *19*, 744-+.

18. Peng, K. Q.; Wu, Y.; Fang, H.; Zhong, X. Y.; Xu, Y.; Zhu, J. *Angew. Chem.-Int. Edit.* **2005**, *44*, 2737-2742.

19. Z. Huang, H. F. *Adv. Mater.* **2007**, *19*, 744-748.

20. Gowrishankar, V.; Miller, N.; McGehee, M. D.; Misner, M. J.; Ryu, D. Y.; Russell, T. P.; Drockenmuller, E.; Hawker, C. J. *Thin Solid Films* **2006**, *513*, 289-294.

21. Kayes, B. M.; Filler, M. A.; Putnam, M. C.; Kelzenberg, M. D.; Lewis, N. S.; Atwater, H. A. *Appl. Phys. Lett.* **2007**, *91*, 103110.

22. Plass, K. E.; Filler, M. A.; Spurgeon, J. M.; Kayes, B. M.; Maldonado, S.; Brunschwig, B. S.; Atwater, H. A.; Lewis, N. S. *Adv. Mater.* **2009**, *21*, 325-328.

23. Spurgeon, J. M.; Plass, K. E.; Kayes, B. M.; Brunschwig, B. S.; Atwater, H. A.; Lewis, N. S. *Appl. Phys. Lett.* **2008**, *93*.

24. Kelzenberg, M. D.; Turner-Evans, D. B.; Kayes, B. M.; Filler, M. A.; Putnam, M. C.; Lewis, N. S.; Atwater, H. A. *Nano Lett.* **2008**, *8*, 710-714.

25. Sze, S. M. *Physics of Semiconductor Devices*; 2nd ed.; John Wiley & Sons: New York, 1981.

26. Bullis, W. M.; Strieter, F. J. *J. Appl. Phys.* **1968**, *39*, 314-&.

27. Struthers, J. D. *J. Appl. Phys.* **1956**, *27*, 1560-1560.

28. Wilcox, W. R.; Lachapelle, T. J. *J. Appl. Phys.* **1964**, *35*, 240-&.

29. Putnam, M. C.; Filler, M. A.; Kayes, B. M.; Kelzenberg, M. D.; Guan, Y. B.; Lewis, N. S.; Eiler, J. M.; Atwater, H. A. *Nano Lett.* **2008**, *8*, 3109-3113.

30. Lewis, N. S. *J. Electrochem. Soc.* **1984**, *131*, 2496-2503.

31. Rosenbluth, M. L.; Lewis, N. S. *J. Phys. Chem.* **1989**, *93*, 3735-3740.

32. Rosenbluth, M. L.; Lewis, N. S. *J. Am. Chem. Soc.* **1986**, *108*, 4689-4695.

33. Forbes, M. D. E.; Lewis, N. S. *J. Am. Chem. Soc.* **1990**, *112*, 3682-3683.

34. Kenyon, C. N.; Tan, M. X.; Kruger, O.; Lewis, N. S. *J. Phys. Chem. B* **1997**, *101*, 2850-2860.

35. Kruger, O.; Kenyon, C. N.; Tan, M. X.; Lewis, N. S. *J. Phys. Chem. B* **1997**, *101*, 2840-2849.

36. Tan, M. X.; Kenyon, C. N.; Kruger, O.; Lewis, N. S. *J. Phys. Chem. B* **1997**, *101*, 2830-2839.

37. Tan, M. X.; Kenyon, C. N.; Lewis, N. S. *J. Phys. Chem.* **1994**, *98*, 4959-4962.

38. Rosenbluth, M. L.; Lieber, C. M.; Lewis, N. S. *Appl. Phys. Lett.* **1984**, *45*, 423-425.

39. Gibbons, J. F.; Cogan, G. W.; Gronet, C. M.; Lewis, N. S. *Appl. Phys. Lett.* **1984**, *45*, 1095-1097.

40. Gronet, C. M.; Lewis, N. S.; Cogan, G. W.; Gibbons, J. F. *Proc. Natl. Acad. Sci.* **1983**, *80*, 1152-1156.

41. Cogan, G. W.; Gronet, C. M.; Gibbons, J. F.; Lewis, N. S. *Appl. Phys. Lett.* **1984**, *44*, 539-541.

42. Gstrein, F.; Michalak, D. J.; Royea, W. J.; Lewis, N. S. *J. Phys. Chem. B* **2002**, *106*, 2950-2961.

43. Groner, M. D.; Koval, C. A. *J. Electroanal. Chem.* **2001**, *498*, 201-208.

44. Beermann, N.; Vayssieres, L.; Lindquist, S. E.; Hagfeldt, A. *J. Electrochem. Soc.* **2000**, *147*, 2456-2461.

45. Baxter, J. B.; Aydil, E. S. *Appl. Phys. Lett.* **2005**, *86*.

46. Law, M.; Greene, L. E.; Johnson, J. C.; Saykally, R.; Yang, P. D. *Nat. Mater.* **2005**, *4*, 455-459.

47. Law, M.; Greene, L. E.; Radenovic, A.; Kuykendall, T.; Liphardt, J.; Yang, P. D. *J. Phys. Chem. B* **2006**, *110*, 22652-22663.

48. Gur, I.; Fromer, N. A.; Geier, M. L.; Alivisatos, A. P. *Science* **2005**, *310*, 462-465.

49. Takanezawa, K.; Hirota, K.; Wei, Q. S.; Tajima, K.; Hashimoto, K. *J. Phys. Chem. C* **2007**, *111*, 7218-7223.

50. Wei, Q. S.; Hirota, K.; Tajima, K.; Hashimoto, K. *Chem. Mat.* **2006**, *18*, 5080-5087.

51. Peng, K. Q.; Xu, Y.; Wu, Y.; Yan, Y. J.; Lee, S. T.; Zhu, J. *Small* **2005**, *1*, 1062-1067.

52. Goodey, A. P.; Eichfeld, S. M.; Lew, K. K.; Redwing, J. M.; Mallouk, T. E. *J. Am. Chem. Soc.* **2007**, *129*, 12344-+.

53. Dalchiele, E. A.; Martín, F.; Leinen, D.; Marotti, R. E.; Ramos-Barrado, J. R. *J. Electrochem. Soc.* **2009**, *156*, K77-K81.

54. Stelzner, T.; Pietsch, M.; Andra, G.; Falk, F.; Ose, E.; Christiansen, S. *Nanotechnology (UK)* **2008**, *19*.

55. Tsakalakos, L.; Balch, J.; Fronheiser, J.; Korevaar, B. A.; Sulima, O.; Rand, J. *Appl. Phys. Lett.* **2007**, *91*.

56. Garnett, E. C.; Yang, P. D. *J. Am. Chem. Soc.* **2008**, *130*, 9224-+.

57. Lewis, N. S.; Gronet, C. M. *Appl. Phys. Lett.* **1983**, *43*, 115-117.

58. Fajardo, A. M.; Lewis, N. S. *J. Phys. Chem. B* **1997**, *101*, 11136-11151.

59. Lewis, N. S.; Rosenbluth, M. L. In *Photocatalysis: Fundamentals and Applications*; Serpone, N., Pelizzetti, E., Eds.; Wiley Interscience: New York, 1989, p 45-121.

60. ASTM Standard G173, 2003e1, "Standard Tables for Reference Solar Spectral Irradiances: Direct Normal and Hemispherical on 37º Tilted Surface," ASTM International, West Conshohocken, PA, 2003, DOI: 10.1520/G0173-03E01.

61. Maiolo, J. R.; Atwater, H. A.; Lewis, N. S. *J. Phys. Chem. C* **2008**, *112*, 6194-6201.

62. Lehmann, V. *Electrochemistry of Silicon: Instrumentation, Science, Materials and Applications*; Wiley-VCH, 2002.

Appendix

MatStat Potentiostat Control Software Manual and Maintenance Guide

A.1 Preamble

This appendix describes the installation, usage, and internal workings of the MatStat potentiostat control software written in Matlab. The software is designed to control analog Princeton Applied Research (PAR) potentiostats using National Instruments (NI) data acquisition cards, although it could be expanded to work with any analog potentiostat and any data acquisition cards that can communicate with Matlab's data acquisition package. MatStat enables both analog and digital waveforms as well as high precision and high rate data acquisition on both current and voltage channels. MatStat is currently capable of making measurements in both potential control and current control modes, as well as open circuit voltage measurements, although the specific use is obviously coupled with the analog potentiostat being used. Furthermore, because the source code for the software is available and extensible, new modules and waveforms can be readily added. The maintenance section describes in some detail the inner workings of the software and should enable future users to both correct any remaining bugs and expand the capabilities of the software. Not only does MatStat enable the acquisition of high quality electrochemical data, it is also significantly more flexible than most of the currently available electrochemical instrumentation software.

A.2 Installation Instructions

A.2.1 Software Modes

Interpreted mode. Software is run from the Matlab command line. For the Caltech Matlab license, this requires network access, which may not always be possible for instruments on carts. MatStat typically runs a bit faster in interpreted mode, and errors or bugs are much easier to diagnose because the error message is printed to the Matlab command window.

Compiled mode. Software is run from the compiled binary, without starting it from the Matlab command line. The main benefit of this mode is that it can be used when Matlab cannot be started (e.g., when there is no network access) and even when there is not a complete installation of Matlab on the computer. However, it tends to run somewhat more slowly than interpreted mode. For the purposes of installation, setting up the software to run in compiled mode on a machine with Matlab will be referred to as *Full Compiled Mode*, and setting up the software on a machine without Matlab will be referred to as *Standalone Compiled Mode*.

A.2.2 System Requirements

A.2.2.1 General Requirements

- Analog potentiostat. MatStat has been tested with only Princeton Applied Research (PAR) analog potentiostats, but should in theory be compatible with any analog potentiostat having an external input and current and voltage monitor outputs.

- Data Acquisition (DAQ) Card. MatStat currently requires a National Instruments (NI) DAQ card, although it could be expanded to support other cards. In particular, the software has been configured and tested with NI PCI-6221 DAQ cards, which have a particular maximum data acquisition rate. This rate is currently hard-coded into the software, so the use of a different model card may require modification of the software for best performance.
- Window XP, SP3. MatStat has been exclusively tested with Windows XP. It may function on other Windows platforms, but no promise of compatibility with other versions of Windows is made.
- Microsoft Office Excel 2007. For saving directly to Excel format, Excel 2007 is recommended. MatStat has been tested extensively with Excel 2007, but may also work with Excel 2003. No promise of compatibility with later versions is made.

A.2.2.2 Stand Alone Compiled Mode

- Matlab Compiler Runtime (MCR), version 7.10
- Microsoft Visual C++ Redistribution (included in MCR)
- MatStat compiled module
- MatStat source code

A.2.2.3 Full Compiled Mode

- Full Matlab Installation, version R2009a
- MatStat compiled module
- MatStat source code

A.2.2.4 Interpreted Mode

- Full Matlab Installation, version 2009a
- MatStat source code

A.2.3 Software Installation

Before undertaking any of these installations, be sure that the NI DAQ card is properly installed on the system. Follow the manufacturer's instructions for this step.

A.2.3.1 Stand Alone Compiled Mode

- Extract the archive *compiled.zip* to anywhere convenient and download the Matlab Compiler Runtime, *MCRInstaller.exe*.
- Double click *MCRIntsaller.exe* to begin installation of the Matlab Compiler Runtime. Follow the instructions, accepting any defaults. The installer should automatically install VCREDIST_X86 if necessary. If prompted about installing the .NET framework, you can ignore the warning. The .NET framework is not needed for MatStat.
- After MCR installation, the following directory should contain the MATLAB runtime:

  C:\Program Files\MATLAB\MATLAB Compiler Runtime\v710

  Change into this directory and create a new folder named *work*. This is the folder from which MatStat expects to operate.
- Copy the following files and folders into *work* from the extracted *compiled.zip* directory:

  - MatStat.m

- MatStat.exe
- MatStat1.ico
- folder: MatStat

- Change into the *MatStat* directory and create a copy of the configuration file that is appropriate for the potentiostat configuration being used (for example, *config_PAR_173_175.mat*). Change the name of this copy to *config.mat.* NOTE: Windows XP does not show file extensions by default. If the file shows up as *config_PAR_173_175*, then the file extension is hidden, and the name should only be changed to *config*.
- To create a shortcut on the Desktop with a MatStat icon, right click on the desktop and select New➔Shortcut. Next, click "Browse..." and navigate to:

  C:\Program Files\MATLAB\MATLAB Compiler Runtime\v710\work

  Select *MatStat.exe*. Finish the wizard and the shortcut will be present on the desktop. To change the icon on the shortcut, right click on it and select Properties. On the "Shortcut" tab, click on "Change Icon..." and ignore the warning that MatStat.exe does not contain any icons. Select "Browse..." and navigate again to:

  C:\Program Files\MATLAB\MATLAB Compiler Runtime\v710\work

  Select *MatStat1.ico*, and click "OK." Click "Apply" and close the MatStat Properties window.
- MatStat can now be started by double clicking on either the shortcut or MatStat.exe.

A.2.3.2 Full Compiled Mode

- Extract the archive *compiled.zip* to anywhere convenient.
- Make sure that the *work* directory exists, or create it if it does not:

  C:\Program Files\MATLAB\R2009a\work

- Copy the following files and folders into the *work* directory:
  - MatStat.m
  - MatStat.exe
  - MatStat1.ico
  - folder: MatStat
- Change into the *MatStat* directory and create a copy of the configuration file that is appropriate for the potentiostat configuration being used (for example, *config_PAR_173_175.mat*). Change the name of this copy to *config.mat*. NOTE: Windows XP does not show file extensions by default. If the file shows up as *config_PAR_173_175*, then the file extension is hidden, and the name should only be changed to *config*.
- To create a shortcut on the Desktop with a MatStat icon, right click on the desktop and select New➔Shortcut. Next, click "Browse..." and navigate to:

  C:\Program Files\MATLAB\R2009a\work

  Select *MatStat.exe*. Finish the wizard and the shortcut will be present on the desktop. To change the icon on the shortcut, right click on it and select Properties. On the "Shortcut" tab, click on "Change Icon..." and ignore the warning that MatStat.exe does not contain any icons. Select "Browse..." and

navigate again to:

C:\Program Files\MATLAB\R2009a\work

Select *MatStat1.ico*, and click "OK." Click "Apply" and close the MatStat Properties window.

- MatStat can now be started by double clicking on either the shortcut or MatStat.exe.

A.2.3.3 Interpreted Mode

- Make sure that Matlab 2009a is installed on the system.
- Make sure that the *work* directory exists, or create it if it does not:

  C:\Program Files\MATLAB\R2009a\work
- Download the latest source code of MatStat and copy the following files and folders into the *work* directory:
  - MatStat.m
  - folder: MatStat
- Change into the *MatStat* directory and create a copy of the configuration file that is appropriate for the potentiostat configuration being used (for example, *config_PAR_173_175.mat*). Change the name of this copy to *config.mat*. NOTE: Windows XP does not show file extensions by default. If the file shows up as *config_PAR_173_175*, then the file extension is hidden, and the name should only be changed to *config*.
- Start Matlab

- Choose File➔Set Path from the pull-down menu. Check that the following folders are at the top of the list:

  C:\Program Files\MATLAB\R2009a\work\MatStat

  C:\Program Files\MATLAB\R2009a\work

  If they are not at the top of the list, move them up so that they are. If they are not present on the list, choose "Add Folder..." and navigate to the appropriate folders, adding each of the two shown above. Finally, chose "Save" and close the Set Path dialog box.
- Now MatStat can be started from the command line by typing "MatStat" and pressing enter.

A.2.4 Potentiostat Setup

In the following section, the correct BNC cable connections for each supported potentiostat configuration will be described. In all cases, the NI PCI-6221 DAQ is connected to an NI BNC-2110 connector breakout block. Connections designated as AO or AI refer to the corresponding analog output or analog input on the BNC breakout block. Furthermore, all of the analog inputs should be set to floating source, not grounded source.

A.2.4.1 PAR 173 Potentiostat

- AI 0 ➔ PAR 173 Electrometer Monitor
- AI 1 ➔ PAR 179 I Out or PAR 176 Output (depending on configuration)
- AO 0 ➔ PAR 173 Ext. Sig. Inputs (right input)

A.2.4.2 PAR 173 Potentiostat with PAR 175 Programmer

- AI 0 ➔ PAR 173 Electrometer Monitor
- AI 1 ➔ PAR 179 I Out or PAR 176 Output (depending on configuration)
- AO 0 ➔ PAR 173 Ext. Sig. Inputs (right input)
- AO 1 ➔ **BOTH** PAR 175 Frame Reset and PAR 175 Ext. Trig. In. (These should be shorted together at the PAR 175 to enable this connection.)
- PAR 175 Signal Output ➔ PAR 173 Ext. Sig. Inputs (left input)

A.2.4.3 PAR 362 Potentiostat

- AI 0 ➔ PAR 362 Potential Monitor (need a BNC to banana plug converter, make sure that the ground plug goes into the black terminal)
- AI 1 ➔ PAR 362 Current Monitor (need a BNC to banana plug converter, make sure that the ground plug goes into the black terminal)
- AO 0 ➔ PAR 362 Ext. In

A.3 Using MatStat

A.3.1 Starting MatStat

For either Stand Alone Compiled or Full Compiled Mode, locate either MatStat.exe or a shortcut to MatStat.exe and double click on it. For Interpreted Mode, start Matlab, type "MatStat" at the command prompt (omit the quotes), and press enter.

A.3.2 Setup Environment

A.3.2.1 Overview

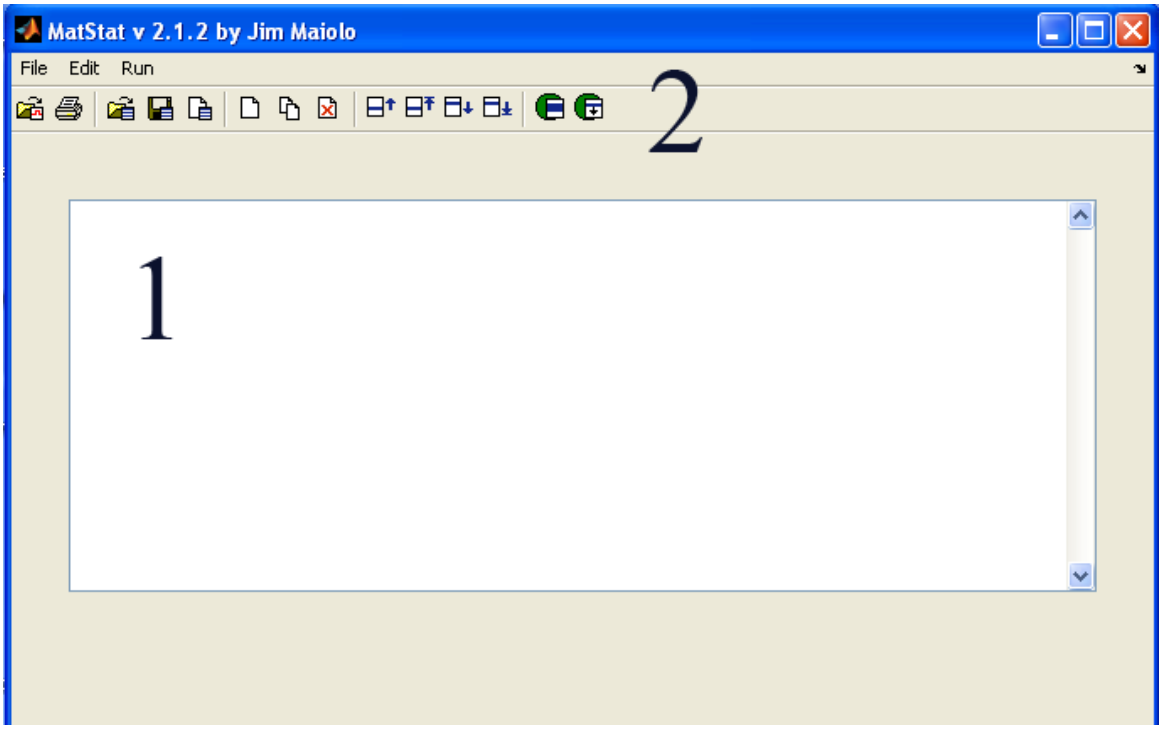

1. Experiment List. Holds a list of all the programmed experiments along with pertinent data about each.
2. Toolbar and Drop-down Menu. Define the possible operations in the Setup Environment.

A.3.2.2 Toolbar Buttons

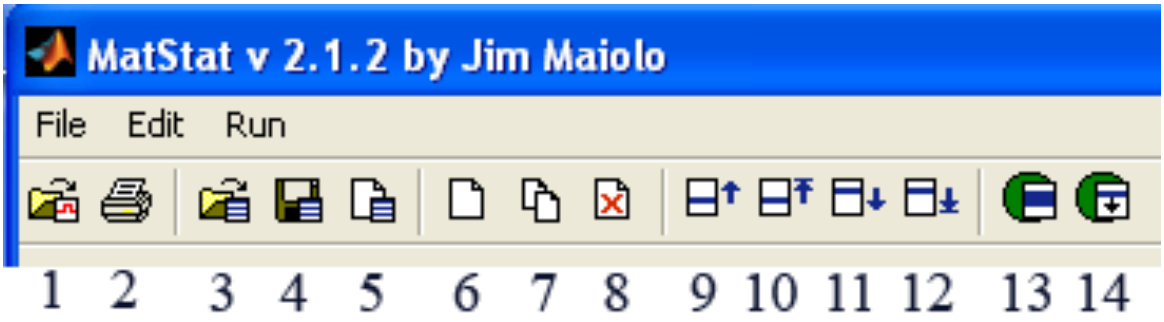

1. Open Graph. Opens a previously saved MatStat file, loading the relevant experimental parameters, and switches to the Run Environment.
2. Print - Prints the visible screen.
3. Open Setup. Opens a previously saved MatStat setup with all experiments.
4. Save Setup. Save this setup.
5. New Setup. Clear all the current experiments (you will be prompted to save).
6. New Experiment. Insert a new experiment below the one(s) currently selected.
7. Copy Experiment. Duplicates the currently selected experiment(s).
8. Delete Experiment. Deletes all of the currently selected experiments.
9. Move Up. Moves the selected experiment(s) up one in the order.
10. Move to Top. Moves the selected experiments(s) to the top of the list.
11. Move Down. Moves the selected experiment(s) down one in the order.
12. Move to Bottom. Moves the selected experiments(s) to the bottom of the list.
13. Run Selected. Runs all selected experiments in order.
14. Run From Selected to End. Runs all experiments starting from the first selected one to the end of the list.

A.3.2.3 Drop-down Menu Contents

- File
  - New Setup. Clear all the current experiments (you will be prompted to save).
  - Open Setup. Opens a previously saved MatStat setup with all experiments.
  - Save Setup. Save this setup under the current file (you will be prompted for a filename if this setup has not been saved before).
  - Save Setup As... Opens a dialog box to choose a save location and filename.
  - Open Graph. Opens a previously saved MatStat file, loading the relevant experimental parameters, and switches to the Run Environment.
  - Print. Prints the visible screen.
  - Quit. Exit MatStat.
- Edit
  - New Experiment. Insert a new experiment below the one(s) currently selected.
  - Duplicate Experiments. Duplicates the currently selected experiment(s).
  - Delete Experiments. Deletes all of the currently selected experiments.
  - Select All. Selects all experiments in the list.
  - Move Up. Moves the selected experiment(s) up one in the order.
  - Move to Top. Moves the selected experiments(s) to the top of the list.
  - Move Down. Moves the selected experiment(s) down one in the order.

  - Move to Bottom. Moves the selected experiments(s) to the bottom of the list.

- Run
  - Run Selected. Runs all selected experiments in order.
  - Run From Selected to End. Runs all experiments starting from the first selected one to the end of the list.

A.3.2.4 Shortcut Keys

- Ctrl+A. Select All
- Ctrl+B. Move to Bottom
- Ctrl+D. Move Down
- Ctrl+E. New Experiment
- Ctrl+F. Run From Selected to End
- Ctrl+G. Open Graph
- Ctrl+K. Duplicate Experiments
- Ctrl+N. New Setup
- Ctrl+O. Open Setup
- Ctrl+P. Print Screen
- Ctrl+Q. Quit
- Ctrl+R. Run Selected
- Ctrl+S. Save Setup
- Ctrl+T. Move to Top
- Ctrl+U. Move Up

- Ctrl+W. Delete Experiments

A.3.2.5 The Experiment List

When populated with experiments, the experiment list should look something like the image below. When using the experiment list, double clicking on a given experiment will pull up the parameters window and allow the experiment to be modified. Furthermore, pressing delete will remove any selected experiments from the list.

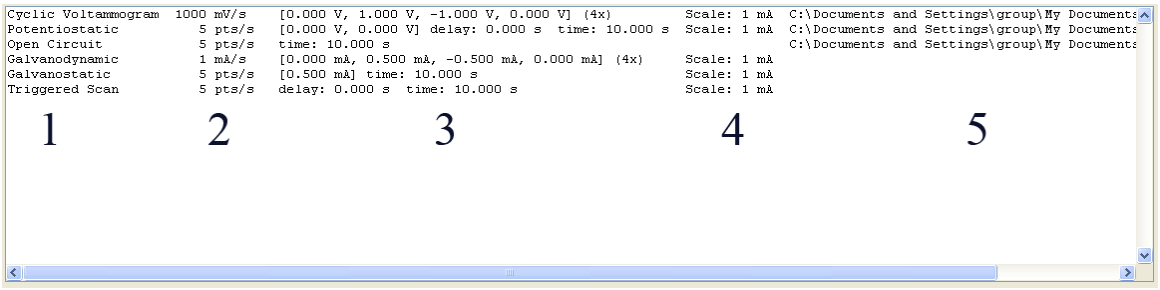

1. Experiment type
2. Scan rate for sweep experiments or data collection rate for other.
3. Experiment-type specific details
4. Current scale (where applicable)
5. Save file path and name (if any)

A.3.2.6 Adding a New Experiment

After choosing to insert a new experiment in any of the ways described above, the user will first be presented with a window for choosing which type of experiment to insert. Note that the contents of this window will depend on the particular analog instruments being used (e.g., the PAR 362 cannot perform triggered experiments). For this reason, it is extremely important that the configuration file match the instruments being used (See Section A.2.3).

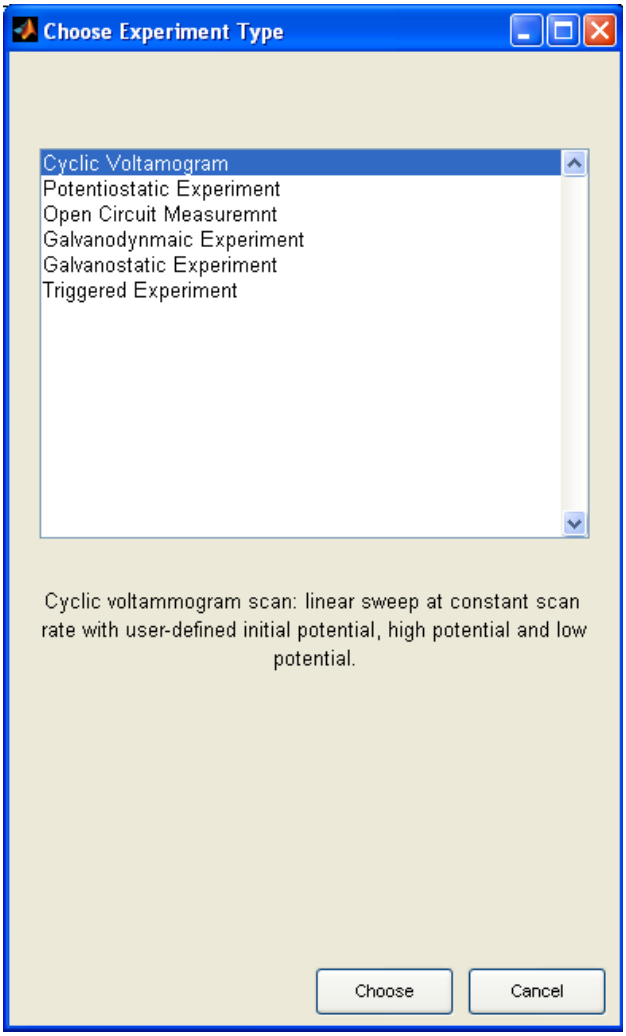

For each experiment, a short description is given. After selecting "Choose," the user will be directed to the configuration window specific to that experiment. See Section A.3.3 for details specific to configuring each type of experiment as well as information on configuring the potentiostats to correctly run each type of experiment.

A.3.2.7 Initiating a Run

Once the experiments have been configured, they can be run by either selecting all of the desired experiments and selecting Run Selected, or by selecting an experiment and choosing Run From Selected to End. When running multiple experiments, it is desirable

to select a save file for each one before running. However, if some experiments in the sequence do not have specified save files, MatStat will pause after each experiment with no specified save file and wait for user input. A warning is issued before the run begins in this case.

NOTE: Use extreme caution when setting up a list of multiple experiments to run in sequence. Since the instruments being used are analog in nature, all of the experiments must have compatible settings on the potentiostat's physical controls. This means, for example, that current controlled experiments cannot be mixed with voltage controlled experiments, and that the current scale must be identical for all of the experiments conducted.

A.3.3 Experiment Types

It should be noted here that one of the strengths of MatStat is its expandability, so it is hoped that more experiments will become available as people use the software and discover new functionality that would be beneficial. In that case, supplemental documentation for the new experiments should be provided. Before presenting specific details about each type of experiment, some general information about MatStat and the experimental parameters will be presented. Also, the names of the fields in the various parameter windows will be given in *italics* throughout this section.

A.3.3.1 Data Collection and Averaging

Because the DAQ card can collect data at an extremely high rate, it is always configured to collect data near its maximal rate. Since the user-requested data rate is usually significantly smaller than this rate, MatStat performs software averaging to

produce the desired number of data points. For example, if the DAQ card can collect data at 100,000 points per second and only 10 points per second are requested, then 10,000 points from the DAQ will be averaged for every point recorded for the user. In each of the configuration windows, the number of points being averaged is always shown, but is set indirectly by the user-entered parameters and is not directly accessible from the user interface. It should be noted that most commercial digitization software does largely the same kind of averaging before reporting data to the user because DAQ cards are capable of such high rates of data acquisition. In the event that a user attempts to enter configuration parameters that would necessitate the DAQ to collect data faster than its maximum rate, the number of points averaged will read as "0-1" indicating that the DAQ cannot keep up with the requested rate. When trying to run an experiment configured in this way, an error will be reported and the user will not be allowed to continue with the experiment until the error is corrected.

A.3.3.2 The Current Scale Setting

For all experiment types except the open circuit voltage measurement, current data will be collected. It is very important in this case to set the current scale of the potentiostat at a value such that the current will not exceed the set limit during the measurement. Furthermore, it is critical that the *Current Scale* setting in the experiment description match the setting on the potentiostat. This setting is used to convert the signal from the potentiostat to a real current, so the reported current values will be off by orders of magnitude if the software current scale is not set to agree with the potentiostat current scale.

A.3.3.3 The Save File Setting

When setting up an experiment, a save file can be specified. The data will be automatically saved to this file when the experiment is completed, overwriting any files with the same path and filename. When using this setting, be sure to change the filename when running multiple experiments from the same configuration.

A.3.3.4 A Note About Final Potentials

Since this is an analog instrument, it cannot be set to return to open circuit following a measurement. Therefore, in each experiment type below, the potential that the DAQ returns to is listed in the description. To return to open circuit, it is necessary to throw the switch on the potentiostat manually.

A.3.3.5 Cyclic Voltammogram

For this experiment, the waveform is generated in the software and sent to the potentiostat through the DAQ card. Therefore, the potentiostat should be in Control E mode and the external input from the DAQ card should be enabled. The scan will begin at *Initial Potential (V)* and proceed in the direction indicated by *Initial Scan Direction*. Upon reaching either the *Upper Scan Limit (V)* or the *Lower Scan Limit (V)*, the scan will reverse directions and proceed to the other scan limit. From that limit it will reverse directions once more and proceed back to the initial potential. Note that scans can also be set up in which the initial potential is equal to one of the limiting potentials. In this case the scan will proceed from the initial potential to the limiting potential and back to the initial potential. Note that the initial sweep direction must be set appropriately when the initial potential is equal to one of the scan endpoints. The programmed scan will be

repeated a number of times equal to *Number of Scans*. The *Scan Rate (mV/s)* sets the sweep speed of the waveform. The *Precision (V/point)* indicates the frequency with which to collect data along the potential axis. When the experiment is finished, the potential will remain at the initial potential.

A.3.3.6 Potentiostatic Experiment

As with the cyclic voltammogram, the potential is set from the DAQ card so the potentiostat should be in Control E mode and the external input from the DAQ card should be enabled. The experiment will hold at *Initial Potential (V)* for a time equal to *Initial Delay (s)*, and will subsequently step to *Run Potential (V)*, holding at that potential for a time equal to *Run Time (s)*. When this time has expired, the potential will return to the initial potential. The rate of data acquisition is set by *Rate (points/s)*.

A.3.3.7 Open Circuit Measurement

In this case, only measurement is performed. When using a PAR 173, the operating mode should be set to Direct Meas. Only and the potential will only be measured. For the PAR 362, which does not have this mode, the potentiostat should be set to Control I and the DAQ card will cause a current of 0 A to be applied, resulting in a simulated open circuit condition. Voltage data only will be collected for a time equal to *Run Time (s)* and data will be collected at a rate of *Rate (points/s)*. The applied potential will remain at zero from the DAQ card no matter what potentiostat is used.

A.3.3.8 Galvanodynamic Experiment

This experiment is a controlled current sweep experiment, very similar to the cyclic voltammogram. The external input from the DAQ card should be enabled, and the

potentiostat should be set to Control I mode. The scan will begin by stepping immediately to *Initial Current (mA)* and proceed in the direction indicated by *Initial Scan Direction*. Upon reaching either the *Upper Scan Limit (mA)* or the *Lower Scan Limit (mA)*, the scan will reverse directions and proceed to the other scan limit. From that limit it will reverse directions once more and proceed back to the initial current. Note that scans can also be set up in which the initial current is equal to one of the limiting currents. In this case the scan will proceed from the initial current to the limiting current and back to the initial current. Note that the initial sweep direction must be set appropriately when the initial current is equal to one of the scan endpoints. The programmed scan will be repeated a number of times equal to *Number of Scans*. The *Scan Rate (mA/s)* sets the sweep speed of the waveform. The *Precision (mA/point)* indicates the frequency with which to collect data along the current axis. Note that it is extremely important with this technique that the current scale in the software match the scale on the potentiostat as the current applied by the potentiostat depends on the current scale setting. Also note that galvanodynamic experiments always return the applied current to zero after the scan, independent of the initial current. This is for safety.

A.3.3.9 Galvanostatic Experiment

This experiment applies a constant current to the cell, so the external input from the DAQ card should be enabled, and the potentiostat should be set to Control I mode. Unlike the potentiostatic experiment, there is no initial delay period enabled for galvanostatic experiments. The scan will immediately jump to *Applied Current (mA)* and hold at that current for a time equal to *Run Time (s)*. The data will be collected at a rate

of *Rate (points/s)*. Note that it is extremely important with this technique that the current scale in the software match the scale on the potentiostat as the current applied by the potentiostat depends on the current scale setting. Also note that galvanostatic experiments always return the applied current to zero after the scan. This is for safety.

A.3.3.10 Triggered Experiment

Triggered experiments are only available with a combination PAR 173 potentiostat and PAR 175 programmer. This allows the user to program the waveform on the programmer, but then the programmer is activated by MatStat and the data is collected by MatStat. For this method, the external input on the PAR 173 coming from the PAR 175 should be enabled. The potentiostat can then be operated in either Control E or Control I mode, depending on the intentions of the user. Any desired waveform can be set on the programmer, and the programmer should then be set to Initial, with the Ext. Trig. button depressed. When running the triggered experiment, the program will wait for *Initial Delay (s)*, collecting data at whatever initial potential the programmer is set to apply. The software will subsequently trigger the programmer and allow it to run for *Run Time (s)*. When the time has elapsed, MatStat will trigger the programmer to return to its initial potential. During the scan, data is collected at of *Rate (points/s)*.

A.3.4 Run Environment

A.3.4.1 Overview

After the user chooses to start an experiment, MatStat will switch to the Run Environment. The experiment will immediately be started, and the data will be shown in in the graph window. When the experiment is finished, it will be saved if a save file was

specified previously. Otherwise, the user will be prompted for a save file. The user may choose to cancel saving at this point. Once the experiment has been completed, the behavior will depend on how the experiment was started. If there are more experiments in the series to be conducted automatically, then they will be started immediately. If the experiment is the last in the series, or if only one experiment was started, then the Run Environment will remain active, and the user can continue to interact with it. This behavior is particularly important if the user has not specified a save file in advance or cancels saving up on completion of the experiment. If there are more experiments in the series to be run, then the data will be lost if not saved.

See the figure on the next page for the parts of the Run Environment.

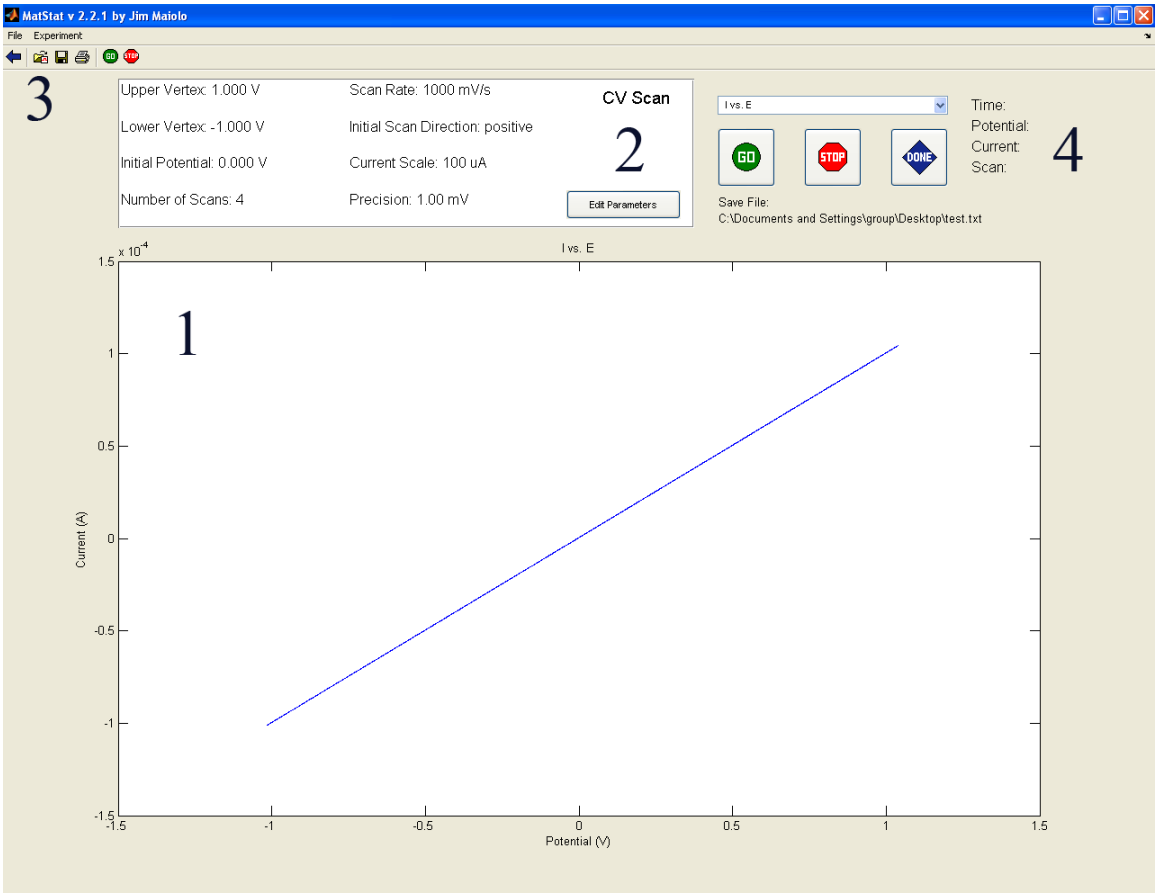

1. Graph area, showing data collected. Zooming is enabled on the plot after data collection has finished by dragging. Right click and select "Reset to Original View" to zoom all the way out. Zooming from the Experiment➔Zoom... menu is always available.
2. Parameter display area and button to edit parameters. The type of experiment is always shown here.
3. Toolbar.
4. Interaction and scan information area.

A.3.4.2 Toolbar Buttons

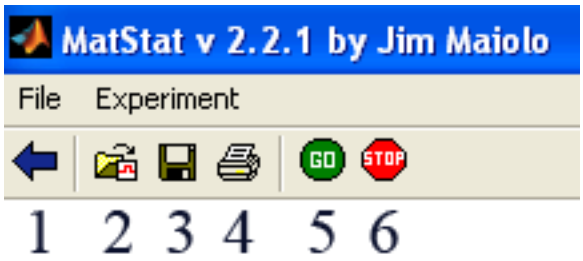

1. Back button. Return to the manager.
2. Open graph. Opens another data set.
3. Save. Saves the currently active data set.
4. Print. Print the current screen.
5. Go. Start running the experiment.
6. Stop. Stop running the current experiment.

A.3.4.3 Interaction and Scan Information Area

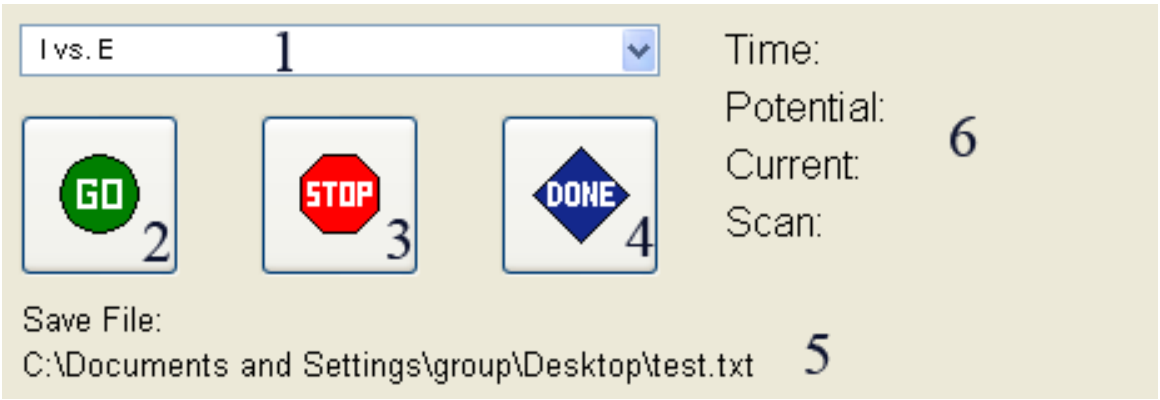

1. Plot type chooser. Display the same data in different ways.
2. Go button. Starts the experiment.
3. Stop button. Stops the experiment.
4. Done button. Return to the setup environment.
5. Save file. Experiments conducted will be saved to this file.

6. Information. Numbers will appear here when an experiment is in progress. Not all experiments will have the same set of information in this area.

A.3.4.4 Drop-down Menu Contents

- File
  - Open Graph. Opens another data set.
  - Save Data. Saves the currently active data set.
  - Print Screen. Print the current screen.
  - Close. Return to the setup environment.
  - Quit. Leave MatStat entirely.
- Experiment
  - Zoom... Opens the zoom window.
  - Start Measurement. Begin running experiment.
  - Stop Measurement. Stop running experiment.
  - Edit Parameters. Change experiment parameters.

A.3.4.5 Shortcut Keys

- Ctrl+E. Edit Parameters
- Ctrl+G. Start Measurement
- Ctrl+H. Stop Measurement
- Ctrl+K. Return to Setup Environment
- Ctrl+O. Open Graph
- Ctrl+P. Print Screen
- Ctrl+Q. Quit MatStat

- Ctrl+S. Save Data
- Ctrl+Z. Zoom...

A.3.4.6 Zoom Window

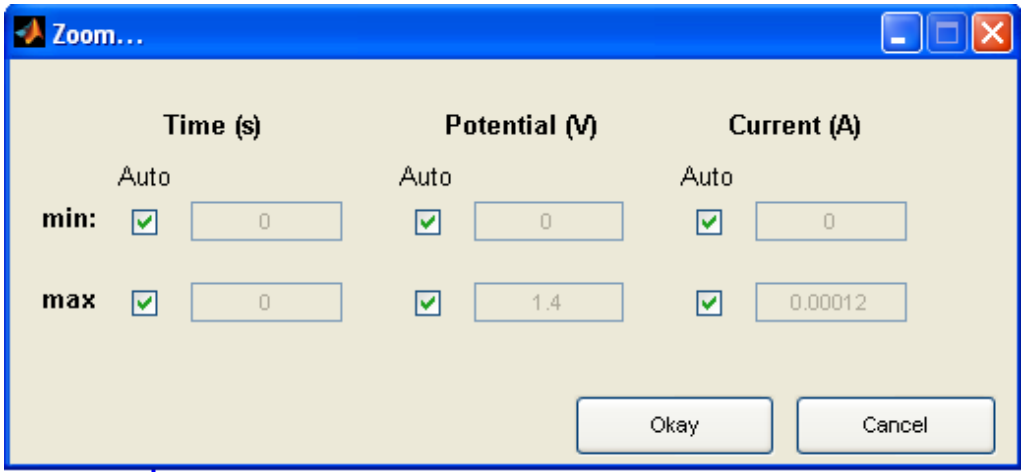

The zoom window allows zooming on all three variables available in the data. In order to set the zoom manually, the *Auto* box must be unchecked for the corresponding value. When zoom parameters have been manually set, they will persist if the plot type is changed. However, if the plot is zoomed using the mouse, the manually set parameters will be overwritten.

A.3.4.7 Run Environment Interaction

While there is an experiment actively running, the interaction options are somewhat limited. The user can specify manual zoom parameters with the zoom window, but cannot zoom using the mouse. The plot type can be changed (e.g., I vs. E or E vs. T), but the data cannot be saved. Choosing Stop will stop the experiment from running. If the user chooses to close the Run Environment or to quit MatStat, a prompt is displayed confirming that the experiment should be stopped in order to close or quit. Similarly,

upon attempting to open a different data set, the user will be asked if they wish to terminate the current run.

When no experiment is currently running (as when the Run Environment is reached by loading another data set or after an experiment has been completed), there are several options available to the user. The user can examine the data by changing the plot type and by changing the zoom either using the mouse or through the zoom window. The user can also edit the experimental parameters. If the Run Environment was initiated from an experiment in the Setup Environment, then any changes made to the experimental parameters in the Run Environment will be reflected in the experiment in the Setup environment. When there is not experiment running, the user can also start a new experiment at any time, either with the original parameters or after modifying the parameters. The user can also choose to save the current data set at any time when there is no experiment running, or as many times as desired, although no modification of the data is possible from within MatStat. Finally, the user can choose to open a previously collected MatStat data set.

A.4 Maintenance and Development Guide

This section describes the inner workings of MatStat and gives some general tips for debugging and further development. In all cases, when making a new change to the software, a new version number should be selected and the files from the previous version preserved so that the changes can be rolled back in the event of unexpected consequences. As of the writing of this manual, the latest version is 2.2.1. Any significant changes after this version should be accompanied by documentation where possible.

A.4.1 Overview

MatStat was designed to be as modular as possible so that new types of experiments could be easily plugged into the existing framework. In an object-oriented language, this could be easily accomplished using inheritance. However, the initial version of Matlab used to develop MatStat did not support inheritance or object-oriented programming (although more recent versions now do). The result, unfortunately, has been significant repetition of code, which is somewhat problematic from a maintenance point of view. Specifically, each type of experiment needs three files: **__GuiSetup**, **__Params**, and **__Open**, where __ should be filled in with an abbreviation for the experiment type. In these files, many of the inner functions are expected to have some differences, but they are largely similar. The end result is that changes to the operation of the program typically need to be propagated through all six of the currently available experiment types. I have usually found it beneficial to fully develop the behavior in one module before translating to the correct behavior for other modules.

In addition to the three files need for each module, I have also maintained generic modules to be used as templates for developing new types of experiments. These are **XXGuiSetup**, **XXParams**, and **XXOpen**, and they should also be updated whenever a change is made so that new experiments can always be added easily. For each experiment, the **__GuiSetup** module is the main workhorse. This module loads all of the graphical user interface (GUI) elements for the Run Environment and controls the acquisition, saving, and plotting of data. All of the main user interactions with the Run Environment are encapsulated in these files as callback functions. The **__Params** file manages the GUI for changing parameter values, while the **__Open** file contains the logic necessary to load data of the specified type. It is necessary to have these functions in a separate file (unlike the save function, which is included in **__GuiSetup** as an inner function) because they must be available to functions outside of the **__GuiSetup** file.

In addition to the three main files for each experiment, there are a number of other modules needed. The most significant is the **MainGuiSetup** file which includes all of the code for the GUI and behavior of the Setup Environment. I will typically refer to this entity as the manager in this document as well as in the program comments. Apart from this file, there is the main **MatStat** file which serves only to set up the figure window and call the manager. There are also a number of smaller modules that will be discussed below.

Matlab functions are typically found in their own file with the same name. I will give the names of these functions in bold, e.g., **MatStat** or **newExp**. In addition, Matlab supports inner functions defined within the body of other functions. I will give the names

of these functions in italics, e.g., *openFile* or *hScanButtonCallback*. Variables will typically be underlined as in Config.

Matlab does not support explicit typing, so I have typically included some type information in my variable names, particularly in variables that are part of structures. Variables with a leading "h" are typically handles to either functions or GUI elements (or regular functions whose handles will be passed as callback functions). Variables with a leading "i" are integers, those with a leading "d" are doubles, and those with a leading "s" are strings. Typically arrays and structures have no leading character indicating type. I will also refer repeatedly to "global variables," by which I mean variables defined at the top level in a main function as opposed to variables defined in an inner function.

A.4.2 Typical Execution Path

I always find that the first step toward understanding a program is to see its typical execution path. I will try to give a brief description of the execution of MatStat in this section. When it is started, **MatStat** first creates a new figure with a toolbar and maximizes it (using the third party function **maximize**). It subsequently attempts to load a configuration file, which currently only contains information about which potentiostat setup is being used. See Section A.4.5 for more information on how to create a valid configuration file. **MatStat** then passes a handle to the figure, a handle to the toolbar, and and a string indicating the potentiostat type to **MainGuiSetup**. The manager, after setting itself up, will then return two handles: one to its main panel so that **MatStat** can make it visible, and one to its kill function so that **MatStat** can ask it to quit when a user tries to close the figure. When making any changes to the way that MatStat quits, errors

may cause the program never to exit. In this case, uncomment the first line in **MatStat**:*hCloseRequestCallback* and the program can exit.

Once **MainGuiSetup** has completed its setup process and **MatStat** has registered the required handles, control of the program has been successfully passed of to **MainGuiSetup**. With control of the execution, **MainGuiSetup** allows users to add, change, and delete experiments as well as to save and load experimental setups. These functions will be described in more detail in Section A.4.4.1. The next major change in execution occurs when an experiment is run. At this point, the manager needs to hand off control to one of the **__GuiSetup** modules. In order to do this, it passes pertinent data to **runDispatch** which then calls the correct **__GuiSetup** module. That module then performs its various setup operations and passes back a handle to its main display panel as well as handles to its kill and run functions. With these handles, the manager can make the Run Environment visible and actually start the run automatically. When the user has finished with the Run Environment, the **__GuiSetup** will signal **MainGuiSetup**, which will then invoke the kill function handle to regain control.

Finally, MatStat can be closed under a variety of circumstances. When the user clicks the close button on the figure (the "X" in the corner), **MatStat** receives the signal and uses its handle to the **MainGuiSetup**:*hKill* function. In **MainGuiSetup**:*hKill*, the manager can check to see if the run window is currently active, and if so it can use the handle it received to **__GuiSetup**:*hKillThis* during setup of the Run Environment to tell the Run environment to close itself. Once the Run Environment has been closed, or if *hKill* is invoked when **MainGuiSetup** has control, the function will simply clean up and

can then exit by deleting the main figure (the handle of which was passed in from **MatStat** during the setup process).

Control can also be passed from **MainGuiSetup** to one of the **__GuiSetup** modules by opening previously saved data. In this case, the same procedure as above is invoked, but the experiment is not caused to run once it has been opened. Furthermore, it is possible to open data from the Run Environment. In this case, **__GuiSetup** uses the handle it received during setup to **MainGuiSetup**:*openFile*, allowing it to destroy itself if another file has been successfully opened. **MainGuiSetup** can then make the new data visible and thus remain in proper communication with the Run Environment at all times.

A.4.3 Important Communication Structures

Descriptions of the most important data structures used for communication among the various modules follow.

A.4.3.1 Config

The Config structure is used to pass both configurational information and key function handles to the **__GuiSetup** modules during setup. The following fields are present:

- hMainFigure. A handle to the main figure. Used to set the parent of the panel created in the Run Environment.
- hToolbar. A handle to the toolbar. Used to add Run Environment toolbar buttons.
- hSwitchBack. A handle to **MainGuiSetup**:*switchBack*.
- hFileOpen. A handle to **MainGuiSetup**:*openFile*.

- sPstat. The potentiostat configuration string.
- hParamUpdate. A handle to **MainGuiSetup**:*updateExp*.
- paramPos. An integer specifying the position of the current experiment in the list from **MainGuiSetup**. A value of -1 is used to indicate an experiment not on the list (i.e., one that was opened from a previous data set).
- hSetSaveDir. A handle to **MainGuiSetup**:*setSaveDir*.
- hGetSaveDir. A handle to **MainGuiSetup**:*getSaveDir*.
- hSetSaveType. A handle to **MainGuiSetup**:*setSaveType*.
- hGetSaveType. A handle to **MainGuiSetup**:*getSaveType*.

A.4.3.2 saveInfo

This structure just contains the information needed to keep track of the last save path and type. This is passed to smaller modules such as the **__Params** modules that need to save and load files, but not run experiments. The fields are:

- hSetSaveDir. A handle to **MainGuiSetup**:*setSaveDir*.
- hGetSaveDir. A handle to **MainGuiSetup**:*getSaveDir*.
- hSetSaveType. A handle to **MainGuiSetup**:*setSaveType*.
- hGetSaveType. A handle to **MainGuiSetup**:*getSaveType*.

A.4.3.3 Scan (or params)

The fields in this structure vary by the type of experiment being used. The fields for each experiment type are given in the file structs.txt in the MatStat source folder. I will only show the fields from the structure used with **IVGuiSetup** here, but the fields tend to be similar with the other experiment types. (However, it should be noted that, for

the Constant I experiments, the parameters are actually stored internally as the potentials that will need to be applied from the DAQ card, not as the currents specified by the user.)

- Type - a string that should be 'IV Scan' for this structure. In general, the strings for the currently available set of experiments are:
  - IV Scan. Cyclic Voltammogram.
  - Pot Scan. Potentiostatic Scan.
  - Trig Scan. Triggered Scan.
  - Voc Scan. Open Circuit Measurement.
  - GalDyn Scan. Galvanodynamic Experiment.
  - GalStat Scan. Galvanostatic Experiment.
- dUpperLimit. The upper scan limit in V.
- dLowerLimit. The lower scan limit in V.
- dInitial. The initial potential in V.
- iScans. The number of scans.
- ScanRate. The scan rate in mV/s.
- Step. The precision of the scan in V/point.
- sDirection. A direction string that should be either "+" or "-."
- dCurrentScale. The current scale setting stored as an integer. To accomplish this, the scale is stored as (1 A)/scale. Thus, at a current scale of 1 A, dCurrentScale = 1, and at a current scale of 1 μA, dCurrentScale = 10^6.
- SaveFile. The full path to use when saving this experiment automatically. The empty string is used when no value has been selected.

- SaveType - The extension of the file type to use (.txt, .mat, or .xls) when saving the experiment automatically. The empty string is used when no value has been selected.

A.4.4 Major Module Descriptions

A.4.4.1 MainGuiSetup

The setup process of **MainGuiSetup** starts with the definition of a number of useful global variables, as well as two structures that are used to communicate with other modules: Config and saveInfo. All of the GUI components that reside directly in the main panel are defined at the top level since they can be made invisible with the main panel when switching to the Run Environment. All of the toolbar and menu items of the manager are declared but not defined at the top level so that they can be readily removed and reinstated as the program switches between the Setup Environment and the Run Environment. The function *menuSetup* is then responsible for configuring the menus and the toolbars. Finally, **MainGuiSetup** attempts to open the default set of parameters, which simply stores the last used set of parameters so that the program does not start empty.

In addition to the communication structures described above, there are several important global variables in **MainGuiSetup**. The handle hKillOther stores the kill function for the currently active Run Environment. The experiments and last_saved variables are both horizontal cell arrays, with each cell consisting of a Scan structure. This is how the currently configured experiments are stored, with experiments being the current list and last_saved being the most recently saved list, which is used to determine

whether the list needs to be saved. In addition saveDir and saveType hold the most recently used directory for saving or opening as well as the last file type so that these can be used when saving or loading new files.

Once the setup process is complete, **MainGuiSetup** is in interactive mode. The process of switching between **MainGuiSetup** and the various **__GuiSetup** modules is described in Section A.4.2. There is a significant amount of additional communication between these modules, however. In particular, the following functions are passed as handles to all of the **__GuiSetup** modules: *switchBack*, *openFile*, *updateExp*, *setSaveDir*, *getSaveDir*, *setSaveType*, and *getSaveType*. The function *switchBack* allows the Run Environment to signal that it has finished. In **MainGuiSetup** this function first tells the Run Environement to quit, checking for success by the return value, and then it makes itself visible again. The function *openFile* allows either **MainGuiSetup** or one of the **__GuiSetup** functions to open another data file, with the **__GuiSetup** closing itself upon successfully opening another data set. The function *updateExp* allows the Run Environment to communicate changes to experiments that were initiated in the Setup Environment, so that the changes are registered there as well. Finally, the function *setSaveDir*, *getSaveDir*, *setSaveType*, and *getSaveType* are present so that every module that calls up a browse window to save or load can both check the last path and file type used (in order to open the browse window in a similar state to the last time it was closed) and report back the new path and file type chosen.

Most of the other behavior of **MainGuiSetup** is fairly straightforward. In particular, the offer to save the setup is always made whenever the program will be closed

or the current setup will be wiped. Whether or not to offer saving is determined by comparing the current setup with the last saved setup. As with the other modules that will be described, memory management of global variables and GUI elements is accomplished by clearing those variables during the process of exiting the **MainGuiSetup** module.

A.4.4.2 The __GuiSetup Family of Modules

These modules actually run all the experiments. Unfortunately, they share a significant amount of code between them, but they have small differences to account for the different experiments being performed. After being called from **MainGuiSetup**, **__GuiSetup** first initializes several global variables and then configures most of the GUI elements. The parameter display is created by the function *updateDisplay* so that it can be remade when the parameters are changed. Next, **__GuiSetup** calls *aoSetup* which attempts to configure the analog output. If it fails due to incorrect parameters, **__GuiSetup** will set all of its return values to -1 to flag that an error has occurred and **MainGuiSetup** will behave accordingly. Note that *aoSetup* is called every time the parameters are changed so that the software is always using the most up-to-date information when initiating a scan. Finally, **__GuiSetup** attempts to load any data that was passed in (if it was called to open previous data). A value of 0 for outData indicates that no data was given (since otherwise outData should be an array, not a scalar).

Descriptions of the global variables are provided in the code comments, so I will only describe a few here. Of particular importance are DAQdata, data, and Time. The data variable holds column data for the voltage and current at each point (two columns,

except for **VocGuiSetup** which only measures potential and therefore has data of only one column), while Time holds column data for the time at each point. Both of these variables are preallocated for the entire length of the run to avoid memory errors in the middle of a run. The values for both of these variables are determined by averaging the data pulled directly from the DAQ card, which is temporarily stored in DAQdata. In addition, the variable Running is used as a flag that a scan is running and certain user interface features should be disabled.

Most of the remaining behavior of **__GuiSetup** is self-explanatory apart from initiating, running, and stopping a scan. When the go button is pushed, any old data is first cleared from the analog output, and then the analog input and output devices are loaded and started. The function *hScanButtonCallback* then enters into its main loop, which gets new data from the DAQ card, averages it, then adds it to the current data set and replots the data. This loop has a built in 0.25 s pause in order to keep from overtaxing the system with updates. The data averaging is accomplished in the following way. During *aoSetup* the total number of points for the entire run is calculated and stored in TotalPoints, and the total time for the run is calculated and stored in InputTime. From this data, the time end points for each interval can be calculated and they are stored in the global variable tEndPoints. During averaging, data from DAQdata, which includes time information, is averaged according to these precalculated time intervals and stored in data.

A scan can be terminated either by user action or by reaching the end of the desired run. In order to obtain the same behavior in both cases, the function *hStopAiPushed* is

registered as the stop function on the analog input variable, and is therefore called when analog input has ceased either by user action or by reaching the end of the run. The function *hStopAiPushed* clears out the DAQ and averages the rest of the data before plotting the final data and calling the *mySave* function. The Running variable is not reset until all of these things have been accomplished so that a new scan cannot be initiated. Finally, the analog input is cleared by calling *reset_ai* to remove any remaining data and free up memory.

A.4.4.3 The __Params Family of Modules

This family of functions acts as the GUI for changing parameter values. They take as arguments a previous set of parameters (to populate the window with), a saveInfo structure for changing the global save and load behavior, and information about how to return the new parameters. This information is given as pos,which specifies the position in the experiment list (or -1 for an experiment not from a list), and returnParams, which is a function handle to send back the changed parameters. It is necessary to return the parameters in this way because the actual **__Params** function returns immediately after configuring the GUI, and the changed parameters need to be returned later, when the user is finished with the dialog box. Apart from this behavior, the workings of the **__Params** family of functions is fairly straightforward.

A.4.4.4 The __Open Family of Modules

This family of functions performs the correct procedures for opening data from a given experiment type. The **__Open** functions take in all the parameters necessary to call **__GuiSetup**, and they return all the parameters required by **MainGuiSetup** when

loading the Run Environment, as well as a parameter opened which is true if the file was read successfully.

A.4.4.5 IVCurve

This function generates the waveform for an IV curve given the pertinent input values. This is used by both **IVGuiSetup** and **GalDynGuiSetup** when configuring their analog output. The data is generated for a given step size that is tied directly to the analog output rate from the caller.

A.4.4.6 myDataPlot

This is the function used to do all of the data plotting. Its complexity has been increased dramatically by the necessity of dealing with five different types of plots as well as numerous possible autoscaling configurations. The function needs the data to plot as well as a handle to the axes to plot it on and the current setting of the window variable. In addition, it needs to know what type of plot is requested and also whether the experiment is running. This is important because mouse zooming is disabled for running experiments due to the constantly changing nature of the data. There is also a hack built into **myDataPlot** to account for the strange zooming behavior of Matlab.

A.4.4.7 updateParams

This function is used to dispatch a parameter update request to the appropriate **__Params** function. It also contains all of the default values used to initially populate the parameter setting dialog boxes for a new experiment. The arguments passed to this function are the same as those passed to the **__Params** functions since it must call those functions.

A.4.4.8 setWindow

This function provides a GUI for setting the window variable. The window variable consists of two rows of data. In the first row are the current values for min time and max time (both in s), min potential and max potential (both in V), and min current and max current (both in A). In the second row are booleans corresponding to whether each corresponding value is currently set to manual scaling or not (i.e., true for manual, false for auto). Thus, when the checkbox is checked on the GUI, the corresponding value is false in the window variable. As with other GUI functions **setWindow** also takes a function handle that allows it to return the updated window variable to the caller since **setWindow** returns immediately after setting up the GUI.

A.4.4.9 newExp

This function is an intermediary GUI that allows the user to choose the type of new experiment. It takes as parameters all of the values that are needed by **__Params** and therefore **updateParams**, since it must call **updateParams** after a selection has been made.

A.4.4.10 exp2str

This function takes the experiments cell array from **MainGuiSetup** and produces a correctly formatted string. It needs the entire array because it changes the spacing so that the columns line up for all of the experiments to be displayed. It is called every time there is a change to the experiment list in **MainGuiSetup**.

A.4.4.11 runDispatch

This is a simple function that starts the correct **__GuiSetup** based on the type of the Scan structure passed in.

A.4.4.12 typeToOpen

This is a simple function to translate between a given type string and an integer for the saving a loading of text files. This is necessary because for some reason Matlab will not allow text to be read from text files, only numbers. Thus, a number is written to the file indicating what type of file it is, so that when the file is opened later, the number can be read and translated back to a type.

A.4.4.13 putFileString

This function takes the last used file type and generates the list of choices for saving so that the last used file type is always the first choice.

A.4.5 Regenerating Configuration Files and Potentiostat Support

The current configuration file only contains a single field that specifies the type of potentiostat setup being used. If desired, future development could significantly expand the information in this file, perhaps to include information about the type of DAQ card being used and even local user preferences. Use the following sequence of commands at the Matlab command prompt to generate a configuration file containing the string PAR173/175 named config_PAR_173_175.mat.

```
>> config.sPstat = 'PAR173/175'
>> save('config_PAR_173_175','config')
```

At the time of this writing, the recognized potentiostat strings are PAR173, PAR173/175, and PAR362, with obvious meanings. When trying to support a new type of potentiostat, it is important to be aware of the following places in the code that make use of the potentiostat configuration. The **newExp** module requires knowledge of the potentiostat configuration so that triggered experiments can be made available only when a programmer is present. In **MainGuiSetup**, knowledge of the potentiostat configuration is required when loading a set of experiments in order to make sure that no unsupported experiments are in the list. Furthermore, in **GalStatGuiSetup** and **GalDynGuiSetup**, the potentiostat type is important because the potential polarity must be inverted on the PAR 173, but not on the PAR 362. Finally, in **TrigGuiSetup**, the configuration is checked on initiating a scan to make sure that the system can support it. When adding a new type of potentiostat, these are good starting points to make sure that MatStat behaves properly with the new hardware. There may be other issues, particularly polarity issues, however, that will need to be addressed as well.

A.4.6 Adding New Modules

When adding new modules to MatStat, the first step should be to modify the generic XX files: **XXGuiSetup**, **XXParams**, and **XXOpen** to suit the specific desired behavior. when making the changes to these functions, it is probably best to consult some of the similar modules to see how things are done in other, working, experiments. In addition to making these modified files, small modifications will be necessary to nearly all of the other small functions, most of which have some form of switch statement on the type of experiment being performed. Although these processes may be somewhat tedious, it is

expected that adding a completely new module should not take more than a few hours for someone who is already somewhat familiar with the inner workings of MatStat. This is one of the key advantages of the software—that it can be readily expanded to suit changing needs and imaginative ideas.

A.5 Final Notes

MatStat is certainly not the most elegant piece of software ever written, but it does work, and it does provide high quality data. More likely than not, with the object-oriented features of Matlab R2008a (most of the original development was done on R2007a), I could significantly improve the structure of the program, but that kind of sweeping overhaul would likely introduce more problems than it would fix. In all likelihood, few changes will be made to the software after I stop maintaining it, and so I hope that the current version is robust and stable enough to provide many years of happy data collection for many researchers. Enjoy!